ABSTRACT

Title of Dissertation:	HIGH TEMPERATURE PROCESSED NANOSTRUCTURES FOR EMERGING ELECTROCHEMICAL DEVICES
	Hua Xie, Doctor of Philosophy, 2019
Dissertation directed by:	Professor Liangbing Hu, Department of Materials Science and Engineering

The future of electric vehicles, consumer electronics, and grid-scale renewable energy storage will place challenging demands on the performance requirements of portable energy conversion and storage devices. The tremendous demand for energy has stimulated intensive research on highly efficient and environmentally benign alternatives to conventional fossil fuels, including fuel cells and lithium metal batteries. In this dissertation, high temperature processing approaches are employed to tune the composition and microstructures of promising material candidates for energy conversion and storage applications.

In the first part of the work, a thermal shock approach is employed to synthesize carbon-based composite materials and platinum-group metal (PGM)-free electrocatalysts for oxygen reduction reactions in fuel cells. Specifically, this work has focused on the nanostructure design of graphene/metal nanoparticles to enhance their chemical stability and electrochemical durability during reactions. In addition to the

systematic characterization, detailed electrochemical performance evaluations were carried out to get a further understanding of the mechanism, which allows for better materials nanoengineering and amelioration in the resulting devices.

The second primary research topic in this dissertation focuses on the high temperature synthesis and post-treatment of high performance Garnet-type solid state electrolytes, which are a promising candidate to replace conventional flammable liquid electrolytes for lithium ion batteries. A melted lithium-alloying approach is applied to improve the interfacial wettability and stability between the lithium metal anode and Garnet solid-state electrolyte. Thermal shock post-treatment on the Garnet electrolyte is demonstrated to significantly eliminate the impurities and improve the electrochemical properties, such as ionic conductivity. Sol-gel and template methods are carried out to demonstrate a fast synthesis approach to achieve hybrid Garnet electrolytes with excellent flexibility and good performance. Additional investigation includes analysis of the theoretical fracture mechanics of electrolyte as determined by dimensionality. A mechanics-guided strategy is employed to design a composite solid-state electrolyte with superb flexibility.

HIGH TEMPERATURE PROCESSED NANOSTRUCTURES FOR EMERGING ELECTROCHEMICAL DEVICES

by

Hua Xie

Dissertation submitted to the Faculty of the Graduate School of the
University of Maryland, College Park, in partial fulfillment
of the requirements for the degree of
Doctor of Philosophy
2019

Advisory Committee:
Professor Liangbing Hu, *Chair/Advisor*
Professor John Cumings
Professor Lourdes Salamanca-Riba
Professor Yifei Mo
Professor Dongxia Liu, *Dean's Representative*

Dedication

To my daughter Lingyun and her “first author” Longnyu.

.

Acknowledgements

I would like to thank my advisor Dr. Liangbing Hu. Your passion for research, scientific insight and ideas are indispensable for me throughout my whole graduate session. I sincerely thank you for the constant support and guidance. I appreciative the precious time you spent guiding, reviewing, and critiquing my work.

Great thanks to my dissertation committee: Prof. John Cumings, Prof. Lourdes Salamanca-Riba, Prof. Yifei Mo and Prof. Dongxia Liu for the support and guidance when I was confronted with confusions and difficulties in the research process and for the suggestions about my dissertation.

I would also like to thank my workmates and collaborators in the range of projects on which we have worked. To Dr. Yifan Liu and Prof. Chao Wang from Johns Hopkins University, thank you for the great suggestions about the electrochemical performance of nanomaterials. To Dr. Boyang Li and Prof. Guofeng Wang from University of Pittsburgh, thanks a lot for the contribution of density functional theory analysis. To Dr. Yinhua Bao, Dr. Jian Cheng and Prof. Teng Li, thank you for the help in finite element analysis. I would like to thank everybody in Hu's group for the assistance of experiment, especially Dr. Chengwei Wang and Dr. Chunpeng Yang for their support in lithium ion batteries. Frankly speaking, without the assistance, the projects in this dissertation could not be accomplished.

To those who have tutored, taught, and supported me in learning the experimental techniques of this work, thank you.

Finally, to my family, especially my wife, I am grateful for the giving-up of decent job in Shanghai and accompanying me all along.

Table of Contents

List of Figures

Chapter 1: Introduction

The ancients exploited fire to keep warm, but temperature embodies more than just warm and cold. Researchers employ high temperatures as a useful tool to develop novel materials. Many reactions require high energy input at the very beginning or during the whole synthesis process. High temperature synthesis is an effective approach to synthesize new materials or to achieve designed phase structures[1,2]. This approach can be operated under air, a reducing atmosphere, or high vacuum, which are suitable for various applications and are widely used in chemical decomposition and compounding, powder sintering and densifying, as well as nanocrystal growth. In this work, high temperature techniques are applied to two distinct emerging energy-related electrochemical systems, improving the key component material properties for advanced applications.

In the first part of the work, a thermal shock approach is employed to synthesize carbon-based composite materials and platinum-group metal (PGM)-free electrocatalysts for oxygen reduction reactions in fuel cells. Specifically, this work has focused on the nanostructure design of graphene/metal nanoparticles to enhance their chemical stability and electrochemical durability during reactions. In addition to the systematic characterization, detailed electrochemical performance evaluations were carried out to get a further understanding of the mechanism, which allows for better materials nanoengineering and amelioration in the resulting devices.

The second primary research topic in this dissertation focuses on the high temperature synthesis and post-treatment of high performance Garnet-type solid state

electrolytes, which are a promising candidate to replace conventional flammable liquid electrolytes for lithium ion batteries. A melted lithium-alloying approach is applied to improve the interfacial wettability and stability between the lithium metal anode and Garnet solid-state electrolyte. Thermal shock post-treatment on the Garnet electrolyte is demonstrated to significantly eliminate the impurities and improve the electrochemical properties, such as ionic conductivity. Sol-gel and template methods are carried out to demonstrate a fast synthesis approach to achieve hybrid Garnet electrolytes with excellent flexibility and good performance. Additional investigation includes analysis of the theoretical fracture mechanics of electrolyte as determined by dimensionality. The strain energy stored in a deformed body scales with the volume, while the surface energy scales with the surface area. As the dimension of the body diminishes, strain energy rapidly scales down and falls below the surface energy. A mechanics-guided strategy is employed to design a composite solid-state electrolyte with superb flexibility.

1.1 Energy Materials

The development of modern society has ballooned the consumption of energy during past decades. It is estimated that, by the year 2050, 130,000 TWh or the equivalent of 10^{10} tons of oils will be required every year, which is a huge number compared with the current energy production rate[3]. This huge gap between supply and demand is exerting heavy pressure on finite fossil-fuel resources, especially under the condition that great effects are taken to curb the increasing CO_2 emission. The ever-growing demand for energy and depleting fossil-fuel resources have stimulated

intensive research on highly efficient and environmentally benign alternatives to current energy storage and conversion systems[4]. Among many candidates, fuel cells and lithium metal batteries are very promising owing to their greener properties during operation and high compatibility with existing facilities[3,5,6]. However, there are still fundamental and technological obstacles needed to overcome, which limit their wide applications to substitute conventional devices.

These issues are expected to be addressed by tuning the materials in nanoscale. Global sustainability gives strong impetus towards the innovation of materials and their synthesis methodologies. Especially the developments in nanotechnology have burgeoned to meet the demanding technological requirements over the past decades. Materials with nanostructures possess attractive properties such as remarkably high chemical activities and enhanced electron-transfer capabilities, which are promising for energy storage as well as electrocatalysis. Thus, the effective combination of material design and nanoscale architecting can address issues that hinder the implementation of emerging electrochemical systems.

1.2 Fuel cell energy-transfer systems

Fuel cells are electrochemical devices that combines hydrogen or methanol fuel with oxygen to generate electricity[5]. Fuel cells are very similar to batteries, exploiting two electrodes separated by an electrolyte, but require the continuous supply of fuel for the constant output of electricity. Catalysts exist on both side of electrodes, which help separate hydrogen into protons and electrons in anode and ionize oxygen in the cathode to combine with protons to form the product water. The anode catalytic reaction is

called fuel oxidation reaction (FOR) and the cathode promote the oxygen reduction reaction (ORR). FOR and ORR electrocatalysts are the critical components for the high performance of fuel cells. Compared to the conventional internal combustion engine, fuel cells do not generate harmful emissions as the only product is water. A single fuel cell generally functions at a working potential around 0.6 to 0.8 V and fuel cells in series can offer high voltage values. As a highly efficient energy conversion technique, fuel cells represent a promising pathway towards a carbon-free conversion cycle without greenhouse gases.

Anode electrode reaction: $H_2 \rightarrow 2H^+ + 2e^-$

Cathode electrode reaction: $O_2 + 4H^+ + 4e^- \rightarrow 2H_2O$

Fuel cells can be classified into several categories according to the nature of electrolyte used in the cell. (a) alkaline fuel cells (AFC) with the alkaline solution electrolyte (aqueous solution of potassium hydroxide soaked in a matrix), (b) phosphoric acid fuel cells (PAFC) with acidic solution electrolyte (phosphoric acid soaked in a matrix), (c) polymer electrolyte membrane fuel cells (PEMFC) with electrolyte consist of the proton exchange membrane, (d) molten carbonate fuel cells (MCFC) with molten carbonate salt electrolyte (solution of Li, Na, and/or K carbonates, soaked in a matrix), (e) solid oxide fuel cells (SOFC) with ceramic ion conducting electrolyte in solid oxide form (such as yttria-stabilized zirconia). Among all of the existing fuel cells, PEM fuel cells are considered as the most promising candidate, which can be widely used for applications such as large power grids, electric vehicles, as well as potable electronics. Despite the promising future associated with this

technique, fuel cells encounter several challenges for their wide applications, such as insufficient durability and high catalyst cost.

1.2.1 Substrate materials for oxygen reduction

To well disperse the catalysts needed for fuel cell reactions, support materials are required to improve the efficiency of catalysts in exposing to reactants/ radicals and transferring electrons. The ideal support materials for fuel cell electrocatalysts typically possess the following advantages: (1) high surface areas and facile dispersing capabilities to disperse and accommodate catalysts (2) excellent electronic conductivity to decrease the overall catalytic barriers (3) high stability and electrochemical corrosion resistance to increase the durability of electrocatalysts.

The state-of-the-art support materials are generally carbon-based nanomaterials including carbon black, carbon nanotubes, graphene, carbon nanofibers, carbon-silicon carbide composite materials, as well as their nitrogen-doped variants. These carbon-based nanomaterials can significantly elevate the electrocatalytic performances. For instance, considering the availability and cost, carbon black materials are one of the most popular electrocatalytic supports with relative high conductivity. However, their instability can induce the electrochemical oxidation during fuel cell operation conditions. Thus, novel nanomaterials with high durability and high conductivity are under extensive research interest for scientists to ameliorate the fuel cell systems.

1.2.2 Oxygen reduction reactions

At the anode part of PEMFC, the reaction rate of FOR (hydrogen) is extremely fast so that the catalyst (Pt) loading can be reduced to less than 0.05 mg/cm^2. However, the sluggish oxygen reduction reaction (ORR) rate in the cathode part places a huge challenge for the wide application of fuel cell technologies[7,8]. To decrease the energy barrier and improve the reaction kinetics, metal electrocatalysts present pivotal roles in the electron transfer process for related reactions. Commercial electrocatalysts for ORR are composed of platinum nanoparticles deposited on carbon substrates, which are effective to decrease the overpotential and increase the current density[9]. The Pt loading is increased to a much higher level around 0.4mg/cm^2. Scientists are also working on the development of alternatives composed of more economically-viable transition metals[1011]. However, these electrocatalysts are burdened with issues such as material degradation, which is so severe that it limits the long-time performance of the catalysts.

To evaluate the performance of synthesized ORR catalysts, a full cell environment should be guaranteed to give the comparation of state-of -the-art Pt/C commercial catalysts, but membrane electrode assembly (MEA) test requires large quantity, which make it impossible to carry out every test. Generally, rotating disk electrode (RDE) is employed to characterize the electrochemical performance of new synthesized catalysts. Water and isopropyl alcohol are used to mix with the catalyst and the mixture is ultra-sonicated to form a uniform ink. Nafion solution is added into the ink to bind the catalysts. Calculated amount of ink is drop on the glass carbon to form a catalyst layer, act as the working electrode.

To characterize the electrochemical behavior of catalysts, electron transfer process is the core session that we focus on. To compensate the influence of mass transfer process during the ORR performance test, RDE is exploited to rotate the catalyst working electrode to increase the mass transfer rate of O_2 at the electrode surface. The electron transfer number during ORR can be calculated based on the Koutecky-Levich equation:

$$\frac{1}{J} = \frac{1}{J_L} + \frac{1}{J_K} = \frac{1}{B\omega^{1/2}} + \frac{1}{J_K} \qquad (1.1)$$

where J, J_L, J_K are nominal, diffusion limiting and kinetic current density, respectively. The reverse of the K-L plot slope, B, is:

$$B = 0.2nF\nu^{-1/6}C_0D_0^{2/3} \qquad (1.2)$$

where n is the electron transfer number, F is the Faraday constant (96485 C/mol), ν is the kinetic viscosity (0.01cm^2/s), C_0 is the concentration of oxygen within the electrolyte (1.2 mmol/L), and D_0 is the diffusion coefficient of oxygen within the electrolyte ($1.9 \times 10^{-5} cm^2/s$).

1.2.3 Issues in existing materials for oxygen reduction in fuel cells

Noble elements are preferred for many specific reactions because of their excellent catalytic performance, however, their high prices have forced researchers to develop and explore alternatives composed of more economically-viable platinum-group metal (PGM)-free transition metals[12–17]. Despite the promise of transition metal nanomaterials, several drawbacks have impeded their long-term utilization toward technological applications. One of the most challenging problems is stability, in which degradation in the form of agglomeration, morphological transformations, and

detachment from the substrate, can lead to degraded properties and even deactivation. Contamination is another important issue that occurs especially when the active sites, such as specific lattice planes, are exposed to toxic environments. To address these issues, various approaches have been undertaken to bolster the chemical stability and electrocatalytic durability. A typical approach is to form a protective shell of organic molecules or carbon[18,19]. However, many of these structures involve complicated operations, or the protective coatings are undesirably thick, hindering the effective reaction pathway, which severely impairs the performance of the nanomaterials.

1.3 Lithium ion battery systems

Lithium ion batteries have been continuously developed during the past decades, and they are successfully employed for applications in electric vehicles, consumer electronics, as well as large-scale energy storage grids. Their advantages such as high energy density, high power density and low self-discharge effects, strengthen their high competitiveness for increasing demand in energy compared with other types of batteries. Generally, lithium ion batteries are composed of two different electrodes with distinct electrochemical potentials, and an electrolyte layer in between the electrodes, which are ionic conductive but electronic insulative to allow lithium ions to travel between electrodes. During the working process (charging), lithium ions travels through the electrolyte while electrons travel through the external circuit from positive electrode to negative electrode, generating electric power for load devices. During the charging process, lithium ions travels back in the opposite direction to storage the energy.

The increasing energy demand has placed a high requirement for lithium ion batteries with high energy density, which can be potentially resolved by selecting electrode materials with higher charge capacity or higher voltage. Energy density describes the total achievable energy stored in a unit mass or volume (Wh/kg or Wh/L). Energy density is equal to the product of electrode specific capacity and voltage. The capacity is consistent with the exploitable lithium ion quantity that can be transferred from the electrodes. The voltage is generally determined by the electrochemical potential difference of the two electrodes. Besides the high energy density requirements, high cycle durability and safety are also determining the future development of lithium ion batteries.

1.3.1 Lithium ion battery materials

Cathode materials Cathode materials for lithium ion batteries can be divided into various types according to their specific reaction types. Intercalation cathode materials are solid host networks, which lithium ions can be inserted into and be removed from the host network during discharging and charging process. The host network compounds can be divided into several crystal structures, such as layered ($LiMO_2$), spinel ($LiMn_2O_4$) as well as olivine ($LiFePO_4$). $LiMO_2$ (M= Co, Ni, Mn or others) layered structure cathode materials are the most commercialized materials till now. LiCoO2 present a theoretical specific capacity of 274 mAh/g with the high discharge voltage around 3.7 V.

Anode materials Anode materials are essential in lithium ion batteries. Commonly used anode materials include graphite, lithium titanium oxide ($Li_4Ti_5O_{12}$), as well

alloying type materials (Si Sn). The anode materials also cat as host structure to store and release lithium ions during charging and discharging process.

Electrolyte materials The electrolyte is an inert part of a lithium ion battery, which determines the rate capability, durability, and safety of a battery, due to its contact and interaction with both positive and negative electrodes. An ideal electrolyte must meet the following requirements: (1). High Li+ ion conductivity (> 10^{-3} S/cm) and low electronic conductivity; (2). Wide electrochemical window, and electrochemically stability with other battery components in the battery operating voltage range; (3). Thermally stability, without flaming or evaporating concerns in the required temperature window.

1.3.2 Solid-state electrolyte for lithium metal energy-storage systems

The future of electric vehicles, consumer electronics, and grid-scale renewable energy storage will place challenging demands on the performance requirements of portable energy storage devices[20–26]. While the lithium-ion (Li-ion) battery dominates the current energy storage market, improvements to these batteries in terms of the energy density, cycle life, and safety will be crucial to meet growing demand.

Lithium (Li) metal has attracted a lot of interest to develop high energy density energy storage devices because it boasts the lowest reduction potential (-3.05 V) and a high theoretical specific capacity (3860 mAh/g). However, the widely known issues, dendritic Li growth along with the flammability of liquid organic electrolytes, can cause serious safety problems and therefore inhibit Li metal batteries for practical applications. Also, traditional commercial electrolytes dissolved in organic solvents have the potential hazard of leakage and are extremely flammable, which can easily

result in fire or explosion, causing more concerns about the safety issues of lithium metal batteries[21]. One of the most attractive and effective strategies to develop practical Li metal batteries is to use solid state electrolytes (SSEs) because of their non-flammability and mechanical strength to block dendritic Li growth. Among the many SSEs studied, the cubic garnet phase SSEs are more attractive because of their excellent chemical stability, high ionic conductivities, and wide electrochemical potential window.

1.3.3 Issues in existing materials for Li-metal batteries

Despite the promising potential of Li metal anodes, dendritic Li growth along with the flammability of liquid organic electrolytes, can cause serious safety problems and therefore inhibit Li metal batteries for practical applications[21]. To address the safety issues and increase the durability, many strategies such as gel polymer electrolytes and all-solid-state electrolytes have been considered. Gel polymer electrolytes, which possess properties of both solid and liquid electrolytes, have been systematically scrutinized[27–30]. But their relatively poor mechanical strength and high cost have limited further wide application. To address the safety issues and increase the durability, two sorts of solid-state electrolytes are extensively studied: solid polymer electrolyte and inorganic solid electrolyte[31–39]. Polymer electrolytes, such as poly(ethylene oxide) (PEO) or polyacrylonitrile (PAN) based matrices exhibit several advantages, including high flexibility and easy fabrication, using commonly available Li salts such as bis(trifluoromethane)sulfonimide lithium salt (LiTFSI) or $LiClO_4$ to impart sufficient ionic conductivity to the system[40]. However, solid polymer electrolytes usually present a relatively lower ionic conductivity compared to liquid

electrolytes[41]. Although adding inorganic ceramic particles as fillers can increase their ionic conductivity, they still fall behind the requirements for commercial application[42–44]. Compared with solid polymer electrolytes, inorganic solid electrolytes possess high ionic conductivity and have a high shear modulus to suppress the growth and penetration of Li dendrites. $Li_7La_3Zr_2O_{12}$, garnet-type Li solid-state electrolyte, has attracted much attention since it was first reported in 2007[45–48]. Despite its attractive ionic conductivity and excellent chemical and electrochemical stability, the brittleness and mass density of the ceramic ion conductor are too high to allow broad application of inorganic electrolytes.

Another challenge for the application of the garnet based solid-state Li metal batteries is the poor interfacial contact between garnet SSEs and electrode materials. Direct contact between Li metal foil and garnet pellets normally results in poor contact and large interfacial resistance. By adding a polymer interface or applying pressure, the Li and garnet interface can be improved marginally, but still has high resistance. The poor wettability of molten Li against garnet substrates also makes it unfeasible to directly coat Li metal on garnet SSEs.

Chapter 2: High Temperature Approaches

High temperature synthesis is an effective approach or an important part of processes to synthesize novel materials or to achieve expected phase structures. The high temperature approach can be operated under reducing atmosphere or high vacuum, which are suitable for various synthesis applications and are widely used in decomposing and compounding, sintering and densifying ceramic powders, and nanocrystal formation.

2.1 Thermal shock

Thermal shock approach (Figure 2-1) demonstrates superior capability for synthesizing ultra-small size high entropy alloy (HEA) nanoparticles. Owing to the extremely short heating duration, thermal shock method ensures (1) ultra-fine particle size by limiting particle nucleation and growth, (2) unique alloy structure by preventing phase separation within nanoparticles, and (3) high-level retention of volatile elements, in our case N-doping/bonding. Although thermal shock is a rapid kinetic process, the synthesized particles is still stable as many other nanoparticles (also not the most thermodynamically favorable). Specially, the size distribution of thermal shock synthesized nanoparticles is stabilized by the strong metal-substrate interaction (and the thin carbon shell), which ensures stability of these nanoparticles as a durable catalyst.

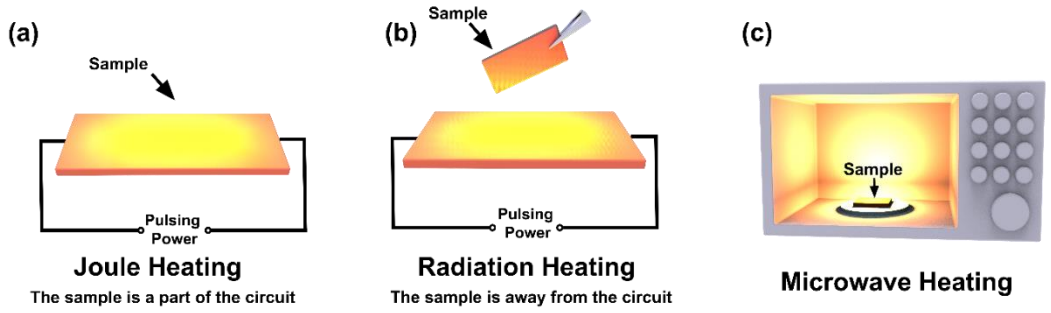

Figure 2-1. Different types of thermal shock approach.

Type of thermal shock	Joule Heating	Radiation Heating	Microwave heating
Heat duration	>= 5 ms	>= 5 ms	Generally optimized at 500 ms (effective duration)
Temperature profile	Square wave shape		
Batch size	~ several mg or more (depend on the material property)	~ several tens mg or more	~several hundred mg or more
Specific requirement	Sample need to be conductive and continuous	No specific requirement	function groups needed to be ignited

Table 2-1. comparison of different types of thermal shock approach.

Temperature measurement

The thermal shock process was analyzed and confirmed by study the temperature change during the process. The thermal shock process was captured using a high speed camera, while the pixels of each frame of the video were analyzed via a self-made program to capture the color of each pixel and study the light emission. The intensity of light emission is then collected, and the intensity vs. time curve shows the change of light emission during the synthesis.

To illustrate the capturing technique, an example is presented in Figure 2.1. to show the whole heating process of thermal shock. At the beginning of the synthesis

(t=0 ms), with no irradiation, there is no light emission. After ~100 ms of irradiation, the lighting happens, and the intensity increases with irradiation. At ~250 ms the light emission is the brightest, after which the light becomes dimmer and eventually dies out after ~600 ms of heating. The total effective heating time is ~600 ms, which is orders of magnitude shorter compared with previous report, making it a unique thermal shock process. Additionally, by fitting the light emission to Planck's law for gray-body radiation, the temperature profile can be achieved. Unlike the intensity of the light emission, the temperature is almost constant during the whole heating process, maintaining a high temperature of ~1600 K. The inconsistency between the intensity of light emission and the temperature stems from the method of capturing the temperature profile, which can be elaborated by observing the photos during the synthesis process. At the beginning of the synthesis, there is no light emitted from the sample. After ~100 ms, several bright spots appear on the sample. Although these bright sparks are scattered on the surface, and consequently the total intensity of the light emission is low, the temperature of these sparks is remarkably high. Therefore, on the temperature profile the temperature at ~100 ms is as high as 2000 K. As the heating progresses, the initial locally generated heat is spread to the whole sample, leading to the rapid increase in light intensity, making the sample completely visible without any ambient light. Although the light emission becomes stronger, since the heat is spread from few hot spots to the entire sample, the temperature of the sample slightly drops, stabilizing at 1600K. After ~250 ms of heating, the light reaches peak brightness. Almost blinding light is emitted from the sample. Afterwards, the light intensity starts dropping and the sample becomes visibly dimmer and dimmer, which eventually dies

off after 600 ms. Although the temperature still remains high, the temperature also becomes less and less stable with the intensity of total light emissions getting lower and lower. When the light dies off, the temperature is no longer measurable.

In summary, during irradiation process the temperature increases to >1600 K in ~100 ms. The high temperature is maintained for ~500 ms, which is followed by rapid cooling to room temperature. The whole synthesis process lasts less than 600 ms, making it an ultrafast thermal shock synthesis method.

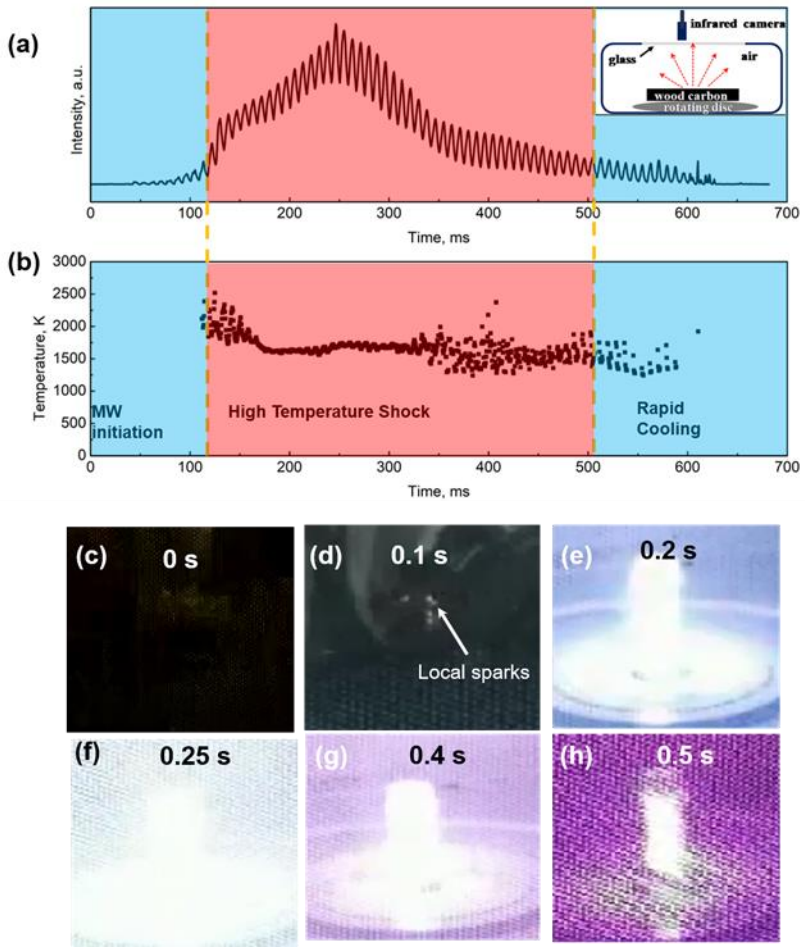

Figure 2-2. The analysis of thermal shock process. (a) The intensity of light emission during the thermal shock. Inset shows the schematics of the measurement setup. (b) Profile of medium temperature captured during the thermal shock by fitting the gray

body theory. (c-h) of sample during the thermal shock process: (c) before thermal shock, (d) 0.1 s, (e) 0.2 s, (f) 0.25 s, (g) 0.4 s (h) 0.5 s after the irradiation, respectively.

Fabrication process of supported core-shell nanoparticles:

Cobalt (II) chloride ($CoCl_2 \cdot 6H_2O$) salt was dissolved in ethanol to form a 0.05 mmol/mL solution. The precursor solution was dropped onto the CNF or carbonized wood substrate in a controlled manner. The as-prepared film was then connected to copper electrodes and silver paste was employed to glue the carbon substrate to the electrodes. A high temperature pulse was applied to the substrate in an argon-filled glovebox using an external Keithley 2425 Source Meter. The emitted light from the substrate was collected by a high-speed spectrometer camera and fitted using the blackbody radiation equation.

2.1 Solid state reaction synthesis process

The most common approach for the synthesis and sintering of inorganic multicomponent materials (ceramic) are the solid-state reactions at high temperature. At lower temperature, solid precursors are not able to overcome the high energy barriers among different solid components. Thus, high temperature is a prerequisite to offer an energy input to help reactants increase their diffusion capabilities to achieve aggregable reaction rate.

Many bulk ceramic functional materials are synthesized through this approach with high temperature range from 1000 to 1500 ℃. These materials involve reactions that thermodynamically achievable, but kinetically difficult to proceed at low

temperature at low temperature. For example, during the fabrication of LLZO electrolyte, many factors influence the reaction rate. (1) the surface and contacting areas of the reactants; (2) the nucleation rate of the LLZO phase; (3) the ionic diffusion rate at the boundaries of the reactants and in the products Thus, high temperature solid state synthesis is closely connected to the thermodynamic behavior and kinetics at high temperature.

Synthesis of Garnet Electrolyte:

The $Li_{6.75}La_3Zr_{1.75}Ta_{0.25}O_{12}$ garnet-type SSE was synthesized via a conventional solid-state reaction method. Stoichiometric amounts of LiOH·H2O (99.9%, Sigma Aldrich), La_2O_3 (≥99.9%, Sigma Aldrich), ZrO_2 (99.9%, Sigma Aldrich), and Ta_2O_5 (99.9%, Sigma Aldrich) were adequately mixed in isopropyl alcohol (IPA) for 12 h. An additional 12 wt% excess $LiOH·H_2O$ was added to compensate for the loss of lithium volatilization during the subsequent high-temperature treatment, in which the mixed materials were dried and calcined at 920 °C for 12 h. The resulting powder was mixed with IPA and ball-milled for 9 h. After drying at room temperature, the powders were pressed into pellets with a diameter of 10 mm using a pressure of 300 MPa and then sintered at 1150 °C for 9 h. After the sintering process, the surfaces of the pellets were polished in a glove box in Ar atmosphere.

2.3 Sol-gel synthesis process

The sol-gel synthesis is a relative new approach for preparing ceramics and many other materials as an effective alternative to high-temperature solid synthesis.

This technique possesses the following advantages compared with traditional high temperature powder synthesis. (1) As the precursor salts are dissolved in the solutions, it would be more facile to achieve the components with high homogeneous states. (2) Compared to the conventional solid-state reactions, sol-gel approaches are more feasible for synthesis at low temperature, which facilitates the sintering process of ceramic powders, such as LLZO Garnet electrolytes. (3) The high viscosity of the sols and gels pave the way for synthesizing complicated structures, such as ultrathin film, nanofibers, as well as porous nano-frameworks.

Synthesis of Garnet nanostructures through sol-gel approach:

$LiNO_3$, $La(NO_3)_3{\cdot}6H_2O$, $ZrO(NO_3)_2{\cdot}6H_2O$ (from Alfa Aesar) were weighed stoichiometrically and dissolved in the 15% acetic acid solution. A stoichiometric amount of $Al(NO_3)_3{\cdot}9H_2O$ is also dissolved in the solution, as Al atoms act as the dopants in the LLZO to increase the concentration of Li vacancies and stabilize the cubic phase at room temperature. A BC nanofiber was cut in the dimension of 10 mm × 5 mm and placed in the freeze dehydration machine for 48 h to dry completely. The freeze-dried BC aerogel was soaked in the LLZO precursor solution for 2 h and then compressed to squeeze out the excess solution. The membrane template was then transferred to a constant temperature oven in vacuum for 24 h to volatilize the solvent and keep the membrane from encountering moisture. The membrane was calcined to 850 ℃ for 1h at a ramp rate 7 ℃/min. After calcination in a muffle furnace at 850 ℃ in the air, BC fibers were completely removed and the c-LLZO membrane was fabricated. Then the calcined membranes were carefully transferred to the glovebox

within Ar gas environment to protect the garnet structure by inhibiting the formation of Li_2CO_3.

Chapter 3: Necklace-like Silicon Carbide and Carbon Nanocomposites Formed by Steady Joule Heating*

3.1 Abstract

Silicon carbide (SiC)/carbon nanocomposites exhibit outstanding physical properties as well as chemical stability and could be utilized in many potential applications. To make SiC/C nanocomposites requires high specific surface area, moderate agglomeration, and good interfacial interaction with the substrate. However, the synthesis of these desired carbon/SiC nanocomposites requires amelioration in two critical aspects – improving the bond strength between C and Si and dispersing SiC homogenously to avoid agglomeration. In our work, a Joule heating method is used to synthesize the SiC/C necklace-like nanocomposite fibers from electrospun C/Si nanofibers. A controlled current was induced to heat the C/Si nanofibers to approximately 2000 K, promoting the in-situ reaction between Si nanoparticles and carbon fibers to create SiC nanoparticles. SiC nanoparticles are uniformly formed in the composites with high specific surface area and strong bonding with the carbon nanofibers. The synthesis of SiC demonstrates a feasibility towards in-situ fabrication of un-agglomerated carbide nanoparticles on the carbon-based nanofiber with desirable interconnection bond strength.

* The results in this chapter have been published: Xie, H.; Fu, K.; Yang, C.; Yao, Y.; Rao, J.; Zhou, Y.; Liu, B.; Kirsch, D.; Hu, L. Necklace-Like Silicon Carbide and Carbon Nanocomposites Formed by Steady Joule Heating. *Small Methods* **2018**, 1700371.

3.2 Introduction

Carbon-based porous nanocomposites with a large specific surface area and interconnected microstructures are the key components for materials with potential application in energy storage (fuel cell and lithium-ion battery), gas storage and catalyst supports[49–53]. The synthesis of these nanocomposites, which is currently the subject of intense research both in academia and industry, has introduced new materials to achieve more complex nanostructures[54–58]. Silicon carbide (SiC), the only chemical compound of C and Si, has been synthesized through many approaches, including the magnesiothermic reaction of carbon/SiO_2 paper[59] and self-propagating high-temperature synthesis[60,61]. SiC exhibits outstanding physical and chemical properties, such as high strength at low density, high thermal conductivity, low thermal expansion, and characteristics of semiconductors with a wide bandgap[62–66]. Because of these remarkable properties, nanocomposites utilizing nanostructured SiC particles embedded in a carbon matrix could be applied in many fields with high promise[67–73].

However, synthesizing stable C/SiC nanocomposites involves solving two critical challenges: (1) the connection between carbon and SiC and (2) their homogenous distribution without agglomeration. In this nanocomposite, the carbon film acts as the substrate to support the SiC nanoparticles, but the weak interactions between the SiC and the carbon could result in the detachment of the SiC nanoparticles from the substrate. Strong interfacial bonding strength between the SiC particles and the substrate is essential for various applications, otherwise the weak bonding could give rise to the release of the SiC particles from the substrate[74]. Maintaining a homogenous distribution of the SiC nanoparticles on the carbon substrate is another

challenge that must be overcome to realize this composite as viable for application. Due to the high specific surface energy, SiC nanoparticles tend to agglomerate to decrease the net Gibbs free energy, which heavily impairs the uniform distribution of the nanoparticles on the substrate. Attempting to bond the SiC particles to carbon-based substrates while also maintaining their nanoscale properties is a great challenge, with the main hurdles being the high specific surface area and homogenous distribution on the substrate without agglomeration. One effective strategy to address these issues is to do in-situ synthesis of the SiC particles directly on the carbon substrates, thus forming strong covalent bonds between the two that will hinder the detachment and agglomeration of nanoparticles.

Herein, we designed an effective strategy to achieve in-situ synthesis of homogeneously dispersed SiC nanoparticles anchored on a carbon substrate via a Joule heating method[75–77]. A C-Si nanofiber (CSNF) framework was employed as the precursor for the in-situ synthesis of the SiC nanoparticles in an inert gas atmosphere through the Joule heating method. The elevated temperature generated by Joule heating boosts the in-situ formation of the SiC nuclei on the local surfaces of the nanofibers, promoting the continuous growth of the SiC nanoparticles. The as-synthesized SiC nanoparticles are strongly bonded on the carbon nanofiber substrate, forming a necklace-like structure. One the other hand, the carbon framework maintains its interconnected structure, which favors high conductivity. The Joule heating method effectively yields SiC nanoparticles with dimensions ranging from tens to several hundreds of nanometers, all of which exhibit strong covalent bonding with the carbon nanofiber substrates. This Joule heating strategy can even generate higher temperature

environments, which could be extended for the facile in-situ synthesis of other carbide nanoparticles with excellent bonding and homogeneous distribution.

3.3 Results and discussion

Figure 3-1 shows the schematic of the strategy employed herein. Si nanospheres with dimensions of approximately 100 nm are evenly distributed in the carbon nanofibers. A controlled current was applied to the CSNF to form a steady, local, high-temperature environment around the nanocomposite fibers. Due to the induced high-temperature, the Si nanoparticles melt and new SiC nuclei can be formed by a reaction on the surface of nanofibers.

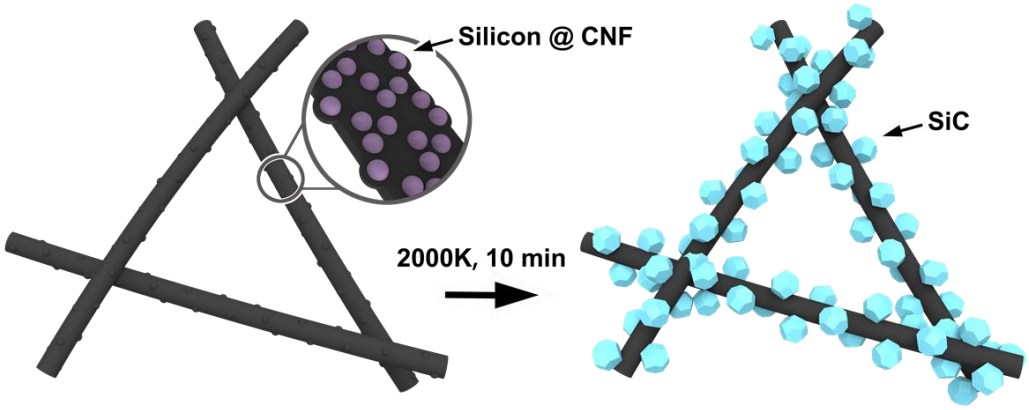

Figure 3-1. Schematic for the in-situ formation of the SiC/carbon necklace-like nanocomposite by Joule heating method: a controlled current was induced to ramp the C/Si nanofibers to about 2000 K, promoting the reaction between the Si nanoparticles and carbon fibers to form the SiC nanoparticles.

Figure 3-2a and b show TEM images for the morphology of a pristine CSNF fiber before Joule heating treatment and the β-SiC/carbon nanocomposite after Joule

heating, respectively. On the surface of the fibers, the crystallized SiC particles form a necklace-like structure; these small clusters are directly connected to the graphitized fibers, with dimensions that range from tens of nanometers to several hundred nanometers. Owing to the continuous high-temperature annealing process, the pristine amorphous carbon demonstrates a trend of graphitization with the resistance drastically decreased.

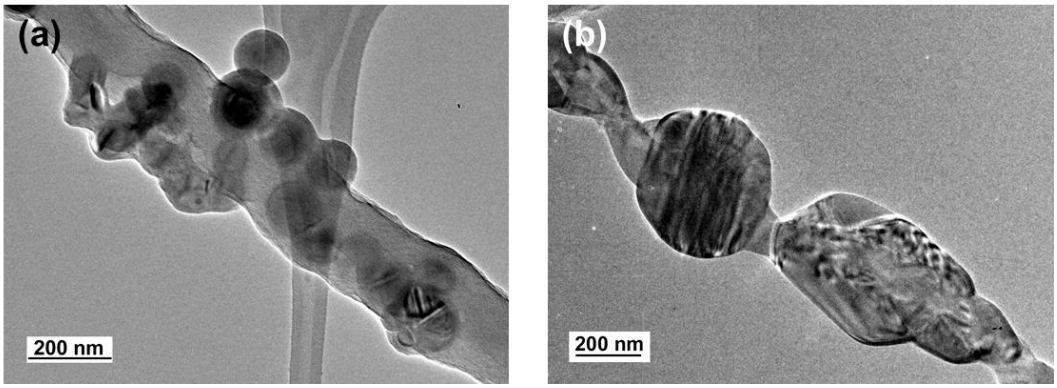

Figure 3-2. (a) TEM image of the pristine electrospun C/Si composite nanofibers. (b) TEM image of the necklace-like SiC/carbon nanocomposite.

To fabricate the pristine CSNF, polyacrylonitrile (PAN) and Si nanospheres are mixed in dimethylformamide (DMF) by ultra-sonication. The resulting solution shows that the Si nanospheres present a well-dispersed distribution in the PAN solution (Figure 3-3a). The Si@PAN nanofibers were prepared via electrospinning. After stabilization in air at 280 ℃, the Si@PAN composite film was carbonized in an argon atmosphere to form the C/Si nanofibers (Figure 3-3b). To obtain SiC on the carbon nanofibers, a CSNF film with a uniform thickness (Figure 3-3c) was fixed on a glass stage with copper tape extending out to the current controller for performing Joule

heating. A controlled current was applied through the CSNF film to realize a local high-temperature environment. Figure 3-3d shows a typical image for the Joule heating process, in which the temperature of the sample was instantly elevated, and the color of the sample shifts from dark red to bright yellow due to gray-body radiation during this brief period.

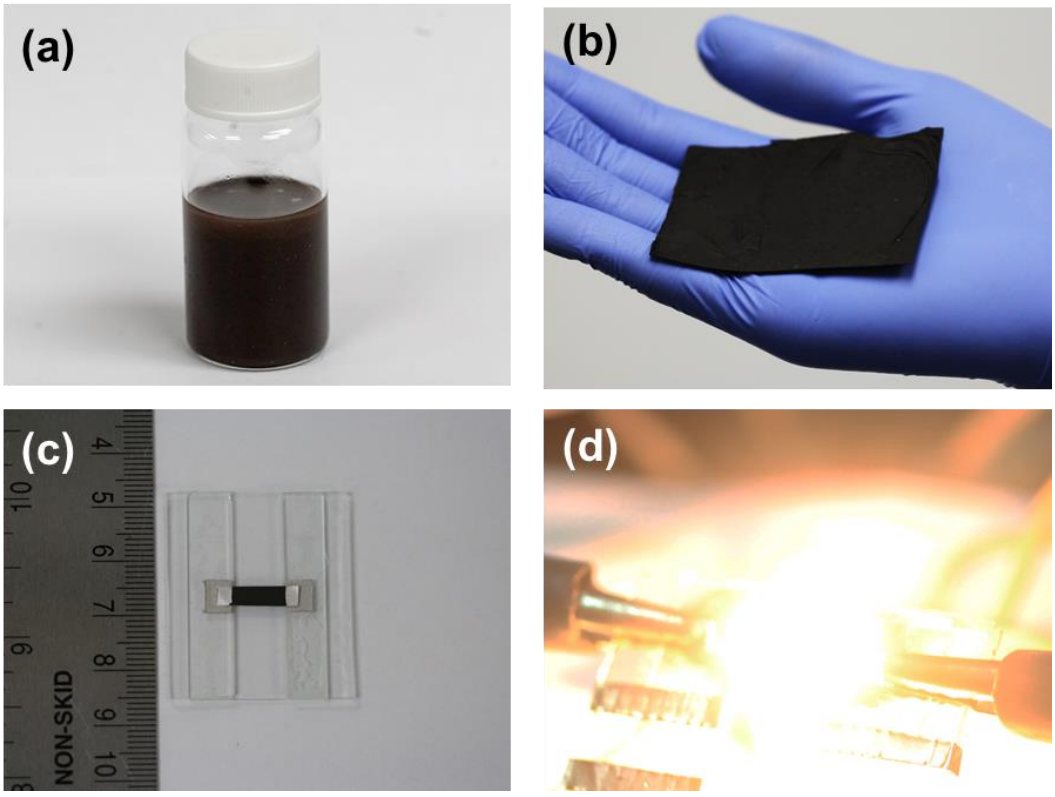

Figure 3-3. (a) Dispersed Si nanospheres in the 8wt% PAN-DMF solution. (b) Image of the CSNF nanocomposite film samples. (c) A typical setup for Joule heating with CSNF nanocomposite film (d) Digital image illustrating the emission of light from the CSNF film during the Joule heating process.

A homemade Labview program was used to control and monitor the current and power value that applied through the CSNF film (Figure 3-4). For the initial process, a small current (about several mA) was applied to the sample, which is

accompanied with the continuous resistance drop for the CSNF film owing to the annealing effects. Once the resistance of the sample drops to an appropriate and relative stable value, the current could be further increased to generate much Joule heat to realize the reaction between Si nanoparticles and carbon nanofibers. The current for the CSNF film is increased at a rate of 10mA/s, and when the highest current value was obtained it was continuously maintained for 10 minutes to promote the growth of the SiC crystallites.

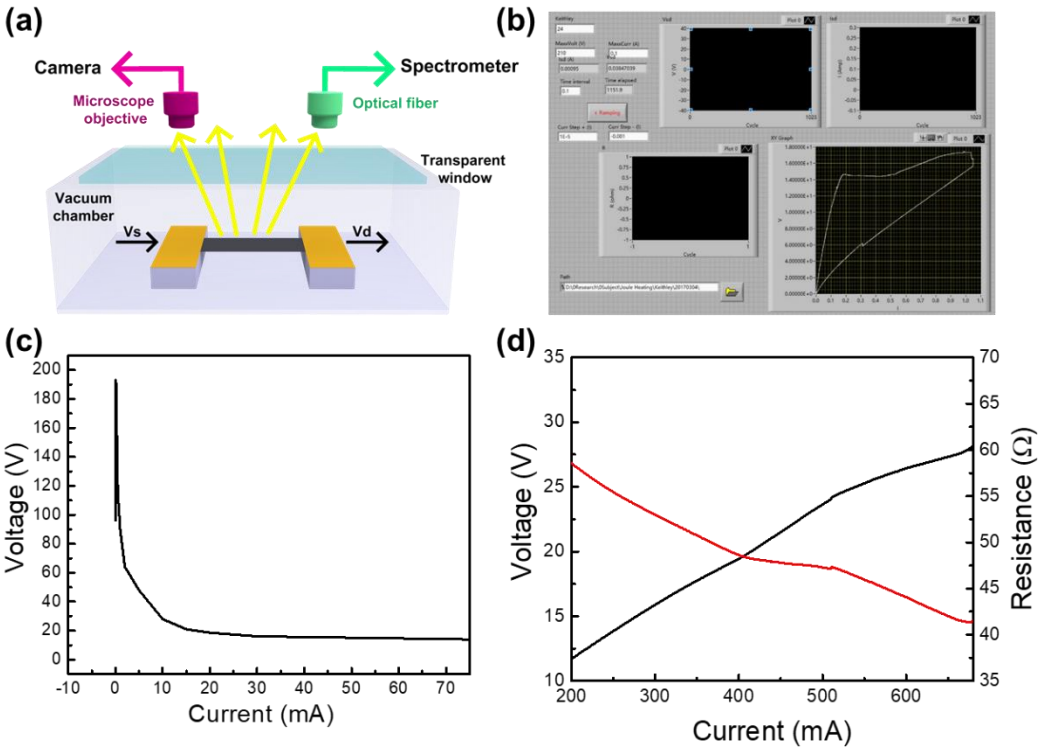

Figure 3-4. (a) Schematic of the method for Joule heat control and temperature acquirement. (b) Program interface to control the current applied on the sample. (c) the voltage-current curve for initial process when the sample is highly resistive: a small current is applied on the sample to decrease the resistivity of the sample. (d) the voltage-

current curve after a huge decrease in resistance. The black curve is the voltage, and the red curve is the resistance change during the increase of current.

The resulting thermal radiation information was directly collected and monitored by a spectrometer. The emission spectra of the CSNF films during the Joule heating process were captured and are shown in Figure 3-5a. Gray body radiation theory was exploited to fit the spectra to acquire the temperature of the composite film at different periods during heating. With the increase in current, the spectral radiation continued to increase until the maximum was reached at a value of 950 mA. The current-control program was appropriately interfered and adjusted to manipulate the temperature for steady Joule heating to guarantee the SiC formation reaction. To determine the influence of power in the Joule heating process, a relation between Joule power and temperature is acquired. Through controlling the current applied on the film, a precise temperature value could be acquired and maintained (Figure 3-5b). This relation between temperature and increasing power shows a linear relation which reached a max value of 2000K at a power of 23.5 W. The sample after steady Joule heating process present a huge resistance drop (red curve, measures twice from 0.00 V to 0.01 V) compared with the original film. Following the Joule heating process, the conductivity of the CSNF is significantly increased from 10^{-5} S/cm to about 10 S/cm, owing to the graphitization of carbon fibers (Figure 3-5c).

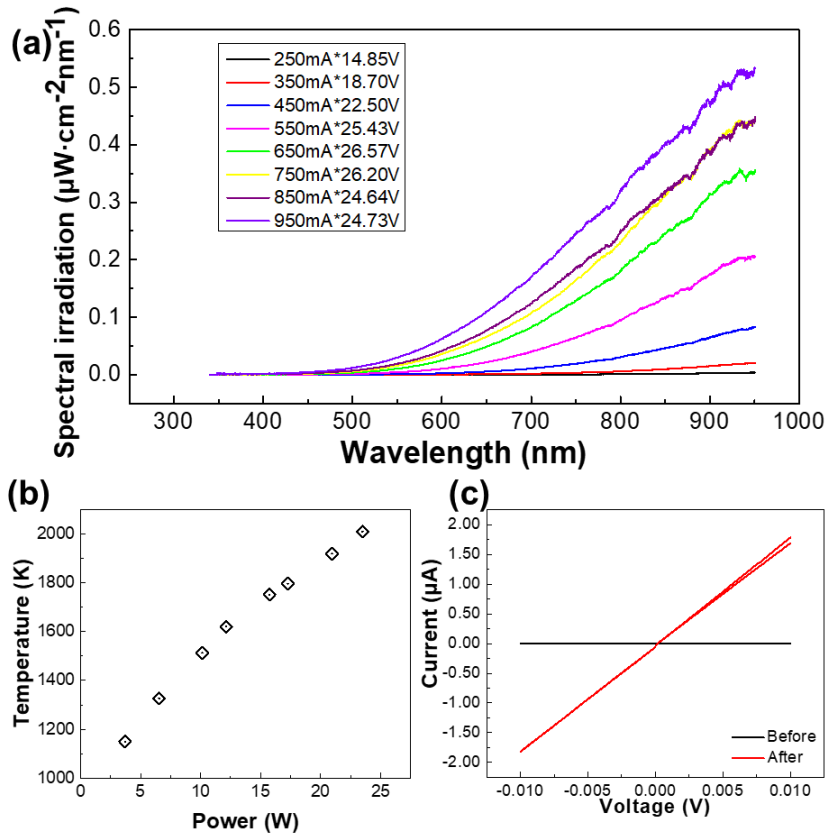

Figure 3-5. (a) Light emission spectra of the CSNF film at different current densities, with large currents indicating a high-temperature environment. (b) Resulting temperature of the CSNF film at different incident powers. (c) The variation of resistance before and after the Joule heating treatment.

Scanning electron microscopy (SEM) was utilized to characterize the morphology and structure of the CSNF film before and after the Joule heating treatment. The fibers of the pristine CSNF film present a smooth surface with lots of "nods", present relatively low electrical conductivity (Figure 3-6a and b). The low conductivity is owing to the unique microstructures of the CSNF fibers. (1) TEM image (Figure 3-2) proves that the fibers possesses an amorphous carbon state, the electric

conductivity of which is much lower than the crystalline graphite or nanotubes. (2) Unlike conventional carbon nanofibers (Figure 3-7) which present a long-range smooth fiber surface, the CSNF presents a “twig” structure with “nods”. These nods which could be considered as defects of the fibers, strongly increase the resistivity of the whole sample. The Si nanospheres are evenly embedded in the nanofibers with a 10-nm amorphous carbon coating layer.

The wrinkles that are present on the fibers are owing to the loss of functional groups in the PAN fibers during the stabilization and carbonization processes. Figure 3-6c depicts the diameter distribution of the pristine fibers, which follow a general Gaussian distribution with an average diameter of 267nm, with several fibers larger than 500nm observed.

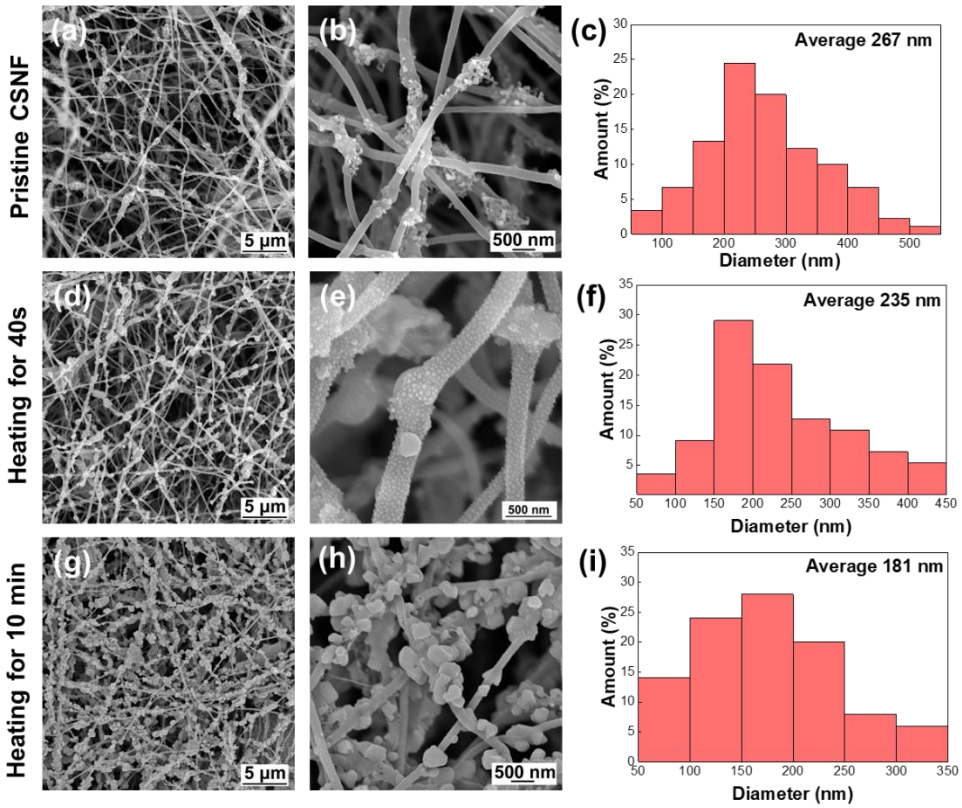

Figure 3-6 (a) and (b) SEM images of the pristine CSNF at different magnifications. (c) Fiber diameter distribution for the pristine CSNF. (d) and (e) SEM images at different magnifications of the SiC nuclei formed in-situ on the surface of the CSNF after a Joule heating treatment for 40 s. (f) Fiber diameter distribution for the SiC/C nanocomposite after a steady Joule heating treatment for 40 s. (g) and (h) SEM images for the necklace-like SiC/C nanocomposite structures after a steady Joule heating treatment for 10 min. (i) Fiber diameter distribution for the SiC/C nanocomposite after a steady Joule heating treatment for 10 min.

After a Joule heating treatment for 40 s, SiC nuclei with an average diameter of less than 10 nm are homogeneously distributed on the interconnected fibers (Figure 3-6d and e). The surfaces of the fibers function as platforms and reservoirs for the formation of SiC nuclei, providing both the C and Si sources and facilitating the heterogeneous nucleation. The SiC nanoparticles on the wrinkled nanofiber areas presented a faster growth rate than those on the smooth fiber surface, because larger concentrations of defects on the wrinkled portions could remarkably reduce the nucleation barrier and enhance the growth rate. Compared with the pristine CSNF, the average diameter of the fibers after Joule heating for 40 s decreases to 235 nm because of the continuous consumption of the Si nanospheres and amorphous carbon during the SiC nucleation and growth process on the surface of the fibers (Figure 3-6f).

After a steady Joule heating treatment for 10 min, as can be seen from Figure 3-6g and h, the diameter of the SiC nanoparticles significantly increases to several hundreds of nanometers. The SiC nanoparticles, bonded with the fibers, form a

necklace-like interconnected network structure. Some SiC particles with diameters larger than 500 nm exhibit a polygonal geometry, indicating the formation of new lattice planes during grain growth processes. With the growth of the SiC nanocrystals, the diameter of the carbon nanofibers continues to be reduced due to the consumption of C. Figure 3-6i shows the average diameter distribution of SiC/CSNF nanocomposites after the Joule heating treatment for 10 min. The average diameter of the SiC/CSNF dropped from 267 nm to 181 nm, with a shrinking rate of 32%. Brunauer–Emmett–Teller (BET) surface area analysis shows that the product possesses a BET surface area about 101.55 m2/g (Figure 3-8), consistent with that of carbon nanofiber achieved by electrospinning method.

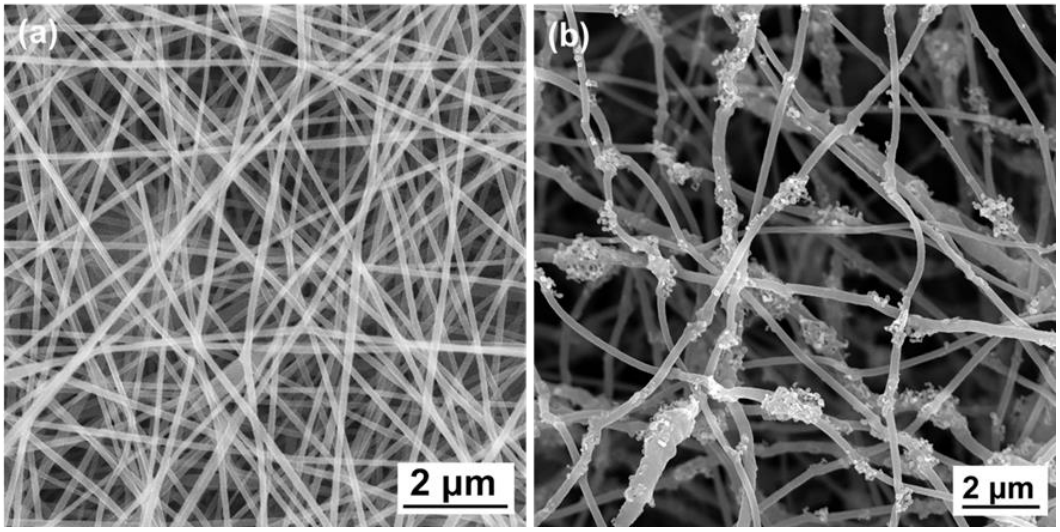

Figure 3-7. (a) Conventional carbon nanofibers with smooth fiber surface in long-range scale. (b) CSNF with twig-like morphology, in which the nods greatly decrease the conductivity of the sample.

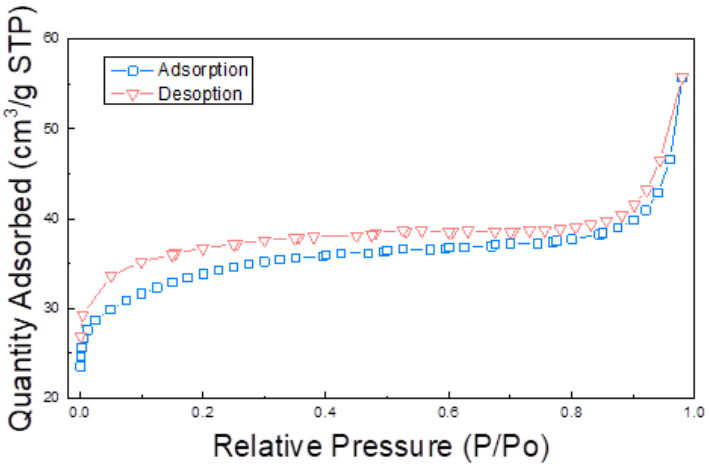

Figure 3-8. BET surface area analysis of SiC/C nanocomposite

To further characterize the newly formed SiC nanoparticles, X-ray diffraction method (XRD) was employed to determine the phase compositions of the composite after the Joule heating for 40s. Figure 3-9 shows the XRD pattern for the CSNF composites after Joule heating for 40s. As shown by the resulting diffraction pattern, the sample is a mixed composite of C, Si and new-formed cubic SiC(β or 3C). The diffraction peaks at 35.88°, 41.78°, 60.24°and 71.97°correspond to the (111), (200), (220) and (311) crystal planes of β-SiC (3C), respectively. The peak at 26.05° corresponds to the crystal plane (002) of graphite, which is formed during the Joule heating process. The broadening peaks around 26°and 43°indicate the amorphous state of the carbon fibers, which is further confirmed by the relatively low electrical conductivity before Joule heating treatment. Peaks at 28.4°, 47.3° and 57.0° correspond to (111), (220) and (311) crystal planes of Si.

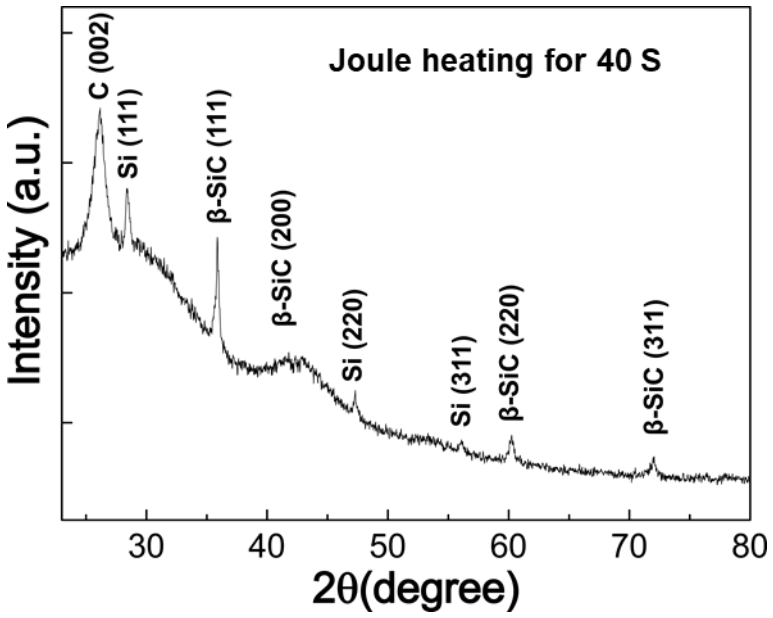

Figure 3-9. XRD pattern of the nanocomposite after Joule heating for 40 s.

To further determine the elemental distribution, energy-dispersive spectroscopy (EDS) analysis was carried out by testing the composite fibers, which ultimately presented a homogenous distribution of element carbon and Si (Figure 3-10).

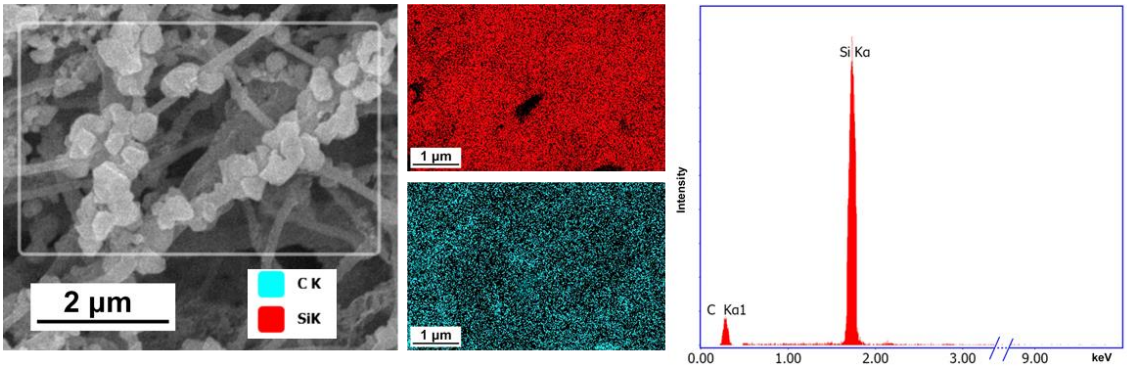

Figure 3-10. EDS mapping of the SiC/C nanocomposite after Joule heating for 10 min

To characterize the phase change of the carbon, Raman spectra tests were conducted for the fiber films before and after Joule heating treatment for 10 min (shown

in Figure 3-11). Pristine CSNF films show a strong peak for Si at 520 cm^{-1} while relatively weak signals for carbon because the pristine carbon fibers were in an amorphous state; this result is consistent with the state of pure carbon nanofibers. After the Joule heating treatment in the inert-gas environment of Argon, the peak for Si at 520 cm^{-1} vanishes and a new peak at approximately 790 cm^{-1} emerges, which indicates the formation of SiC. On the other hand, the characteristic peaks for carbon become much sharper than the pristine CSNF sample prior to the Joule heating treatment. The D-band peak, which stands for the defects and disorder in the carbon fibers, was obviously suppressed compared with the G-band, which corresponds to graphitic, or ordered, carbon. This is related to the graphitization effect, that is, the defects in the carbon nanofiber are annealed in the diffusion process at high-temperature. This is also consistent with the increased conductivity following the Joule heating treatment.

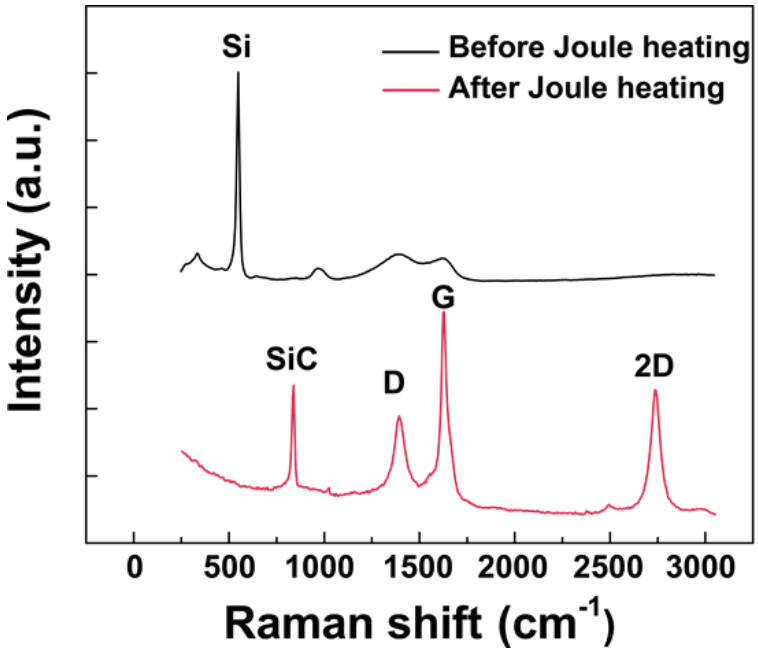

Figure 3-11. Raman spectra for the films before and after the Joule heating treatment.

Transmission electron microscopy (TEM) was exploited to characterize the morphology and bonding of the nanocomposite. TEM images of the necklace-like particles (Figure 3-12a) show that SiC nanoparticles tend to show an angular morphological structure welded on the fiber surface. After ultra-sonication in water for 10 min, the necklace-like structure can still be observed by TEM, indicating good bonding between the SiC nanoparticles and the nanofibers, owing to the in-situ formation mechanism of SiC by Joule heating. The nanofibers offer outstanding effective interfaces for the heterogeneous nucleation of the SiC particles to reduce surface energy by decreasing the contact angles needed for nucleation. The cubic-SiC phase was also confirmed by high-resolution transmission electron microscopy (HR-TEM) imaging and its Fast Fourier Transform (FFT) result is shown in Figure 3-12b. The HR-TEM image shows the cubic SiC plane along [112] direction and the inset is the FFT results with plane indices assigned within. The planes in the FFT results are also outlined on the image.

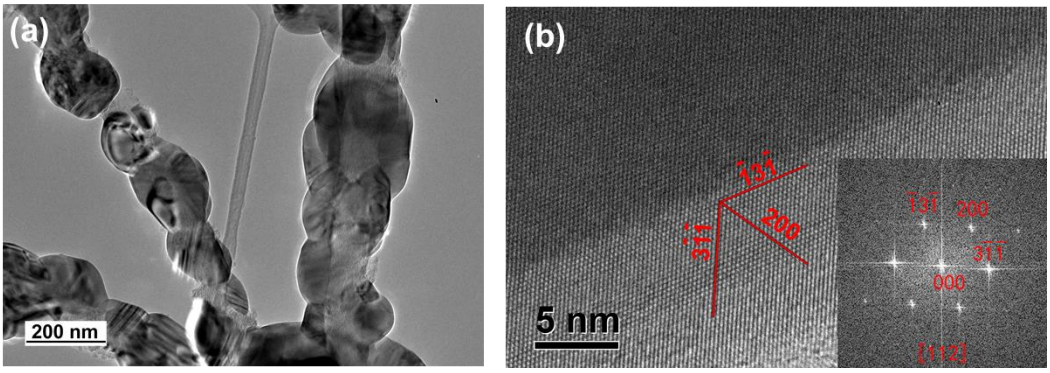

Figure 3-12. (a) TEM image of the SiC/C nanocomposite which shows solid bonding between the SiC and the carbon after ultra-sonication. (b) HR-TEM micrograph of the cubic SiC along the [112] direction. Inset is the FFT results with plane indices assigned within; the respective planes are also outlined on the image.

3.4 Conclusion

Joule heating on the C/Si nanocomposite fibers was used for the first time to do an in-situ synthesis of a SiC/carbon necklace-like nanostructure, in which the nanoparticles of SiC can be interconnected with each other while still maintaining their high specific surface area. The CSNF acts as a reservoir to provide C and Si atoms before Joule heating, as a micro furnace to heat the pristine reagent during Joule heating, and finally as the substrate to host the formed SiC nanoparticles. The thermal radiation information during the Joule heating process was recorded using a spectrometer and gray-body radiation theory was utilized to acquire the heating temperature. Pristine CSNF films were heated to 2000 K, which significantly improved the graphitic structure of the carbon nanofibers, thereby increasing the conductivity of substrate. The high-temperature enabled by the Joule heating efficiently boosts the in-situ formation of SiC, while also enhancing the bonding strength between the SiC nanoparticles and carbon nanofibers. SiC nanoparticles can be homogeneously distributed and strongly anchored on the carbon nanofibers, which is advantageous for the potential application of this novel composite. Joule heating, as an effective and scalable method, has the potential to promote the in-situ synthesis of other homogenous carbide nanoparticles, which in turn could have enhanced bonding strengths with carbon-based substrates and similar homogeneous distribution similar to the results discussed herein.

3.5 Experimental

CSNF Preparation

Si nanoparticles were purchased from SkySpring Nanomaterials, and the particles sizes were between 70 nm to 120 nm. These particles were well crystallized without any surfactant or oxide layers on their surfaces. PAN (Mw=150,000) and solvent DMF were purchase from Sigma Aldrich. PAN was dissolved in DMF to form an 8 wt% transparent solution and stirred at 65 ℃ for 12 h. Then the same amount Si nanoparticles were added in the PAN solution and were ultra-sonicated in water bath for 24 h to form a homogenous dispersed suspension. The suspension was electrospun at a voltage of 15 kV. The spinning distance is 15 cm with a feeding rate of 1ml/hour. A rotating drum was used to collect the dry fibers to get a thick pristine film with iso-thickness. The PAN/Si nanofiber film was stabilized at a temperature of 280℃ for 3 h and carbonized at 800℃ in an Argon atmosphere to get the CSNF film.

Joule heating process

Prepared CSNF films segmented into rectangles were fixed on the glass stage with silver paste and extended with copper tape. The sample used for the Joule heat possesses a length of 10 mm, a width of 4 mm. The thickness of the sample is about 30 μm. The Joule heating process was carried out in a glove box with argon atmosphere. A Keithley power source was exploited to apply the current through the film. A homemade Labview program was used to control the current and power value that applied through the CSNF film. For the initial process, a small current (about several mA) was applied to the sample. The emission spectra were collected and monitored by an optic fiber and processed by spectrometer from Ocean Optics Company.

Characterizations

Tescan XEIA3 SEM and JEOL 2100 LaB6 TEM were used to characterize the morphology of nanofibers before and after Joule heating treatments. An EDS from EDAX company was used to test the elements on the nanoparticles formed by Joule heating effects. Raman characterization was done with the laser wavelength at 532 nm. The conductivity of the films was measured by a four-probe method. XRD pattern was achieved through D8 Advanced X-ray Diffraction system.

Chapter 4: High-Temperature-Pulse Synthesis of Ultrathin-Graphene-Coated Metal Nanoparticles*

4.1 Abstract

Reducing the use of precious metals presents a grand challenge for ensuring the sustainability of modern industry. Nanostructured materials comprising earth-abundant elements show great potential as substitutes for scarce, expensive materials, but degradation and contamination issues in working environments severely limit their practical applications. Here we report a facile and scalable strategy to synthesize ultrathin-graphene-coated cobalt nanoparticles which are achieved by the application of an electrical current pulse to a carbon-based substrate and by generating a transient high temperature of up to 1500 K in 50 ms to induce the nanoparticle growth and graphene coating. Thickness of the graphene shell is effectively controlled to be under three atomic layers, favorable for charge transfer and electrocatalytic applications. The one-step derived ultrathin-graphene-coated Co nanoparticles exhibit high activity and durability for the oxygen reduction reaction. Our one-step synthetic strategy provides a universal, scalable and cost-effective approach for the fast synthesis of metal-carbon core-shell nanoarchitectures for catalytic and other applications.

* The results in this chapter have been submitted: Xie, H.; Liu, Y.; Li N., et al. High-Temperature-Pulse Synthesis of Ultrathin-Graphene-Coated Metal Nanoparticles

4.2 Introduction

Global sustainability gives strong impetus towards the innovation of materials and their methodologies; consequently, developments in nanotechnology have burgeoned and strived to meet the demanding technological requirements over the past decades. Materials with nanostructures possess attractive properties such as remarkably high chemical activities and enhanced electron-transfer capabilities, which are promising for energy storage[78,79], nanoelectronics[80,81], as well as electrocatalysis[82–85]. Noble elements are preferred for many specific reactions because of their excellent catalytic performance[86–91], however, their high prices have forced researchers to develop and explore alternatives composed of more economically-viable transition metals[13,15,17,92–94]. Despite the promise of transition metal nanomaterials, several drawbacks have impeded their long-term utilization toward technological applications. One of the most challenging problems is stability, in which degradation in the form of agglomeration, morphological transformations, and detachment from the substrate, can lead to degraded properties and even deactivation. Contamination is another important issue that occurs especially when the active sites, such as specific lattice planes, are exposed to toxic environments. To address these issues, various approaches have been undertaken to bolster the chemical stability and electrocatalytic durability. A typical approach is to form a protective shell of organic molecules or carbon[18,19]. However, many of these structures involve complicated operations, or the protective coatings are undesirably thick, hindering the effective reaction pathway, which severely impairs the performance of the nanomaterials.

To protect nanomaterial morphology and to retain their chemical stability and electrocatalytic durability, an innovative yet simple synthetic technique can circumvent these limitations. Therefore, a robust, low-cost and scalable Joule heating method of creating ultrathin and durable coating layers on nanoparticles is introduced in this work. Here, we synthesize metallic nanoparticles with a desired thickness of graphene layers by applying one single high-temperature pulse to metal precursor loaded carbon substrates. No complicated organic materials were exploited for the formation of the ultrathin graphene shells. Amorphous carbon sources, such as carbonized nanofibers or carbonized wood, act as reservoirs which supply carbon atoms towards the formation of ultrathin graphene shells. Tuning both the pulse temperature and time enables precise control over the amount of graphene layers to under three. Our strategy presents several advantages: (1) the procedure successfully fabricates core-shell nanostructures in one facile step; (2) shell thickness can be effectively tuned to under three atomic layers; (3) this unique approach facilitates control over material design, where an abundance of substrates and precursor salts can be used. The enhanced chemical stability and electrocatalytic durability of the resultant core-shell nanoparticles are advantageous for a diverse array of applications.

4.3 Results and discussion

Our synthesis strategy is briefly illustrated in Figure 4-1, which schematically reveals the fabrication process of graphene/transition metal core-shell nanoparticles. Cobalt(II) chloride ($CoCl_2 \cdot 6H_2O$) was exploited as a precursor salt loaded onto carbon-based supports through solution-based processing. Specifically, melamine can be

added in the precursor as a nitrogen source to realize nitrogen doping, which further improves the electrocatalytic activity. Note that the substrates, such as carbon nanofibers (CNF) and carbonized wood, are readily available and easily manufacturable. A controlled transient current was applied to the conductive substrate with a time span of 50 ms to instantaneously raise the localized temperature to approximately 1500 K. The high temperature achieved provides the energy necessary to decompose the $CoCl_2$ precursor and to form Co clusters. Meanwhile, carbon atoms from the substrate are also supplied enough energy to detach locally from the substrate. Rapid quenching occurs after the high temperature pulse at a rate of ~30,000 K/s, which enables the formation of non-agglomerated core-shell nanoparticles anchored to the defective sites of the carbon substrates. It is supposed that the Co nanoparticle cores function as catalysts aiding the epitaxial growth of the ultrathin graphene shells, which resembles the fabrication of graphene by chemical vapor deposition (CVD)[95,96]. The ultrathin graphene shell acts as a citadel to separate the nanoparticles to inhibit the agglomeration, to protect Co nanoparticles from contamination, as well as to anchor firmly the nanoparticles on the substrate, while still allowing electrons from oxygen to penetrate the thin graphene and react with the Co nanoparticles.

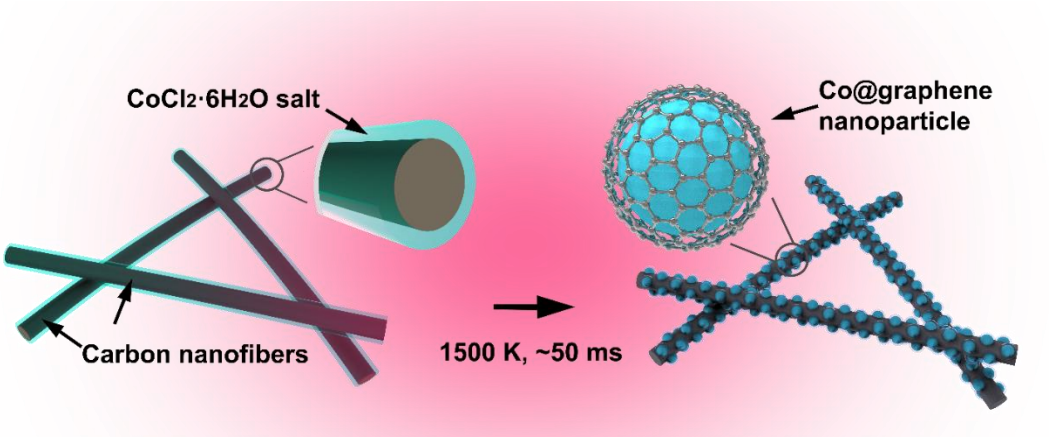

Figure 4-1. Schematic demonstrating the high-temperature-pulse method to controllably synthesize core-shell nanoparticles, such as Co@graphene, with one to three graphene coating layers.

Figure 4-2a and b present the typical morphological evolution of the samples before and after the high temperature pulse. After the high temperature pulse, Co nanoparticles coated with graphene are homogenously anchored onto the CNF (Figure 4-2b).

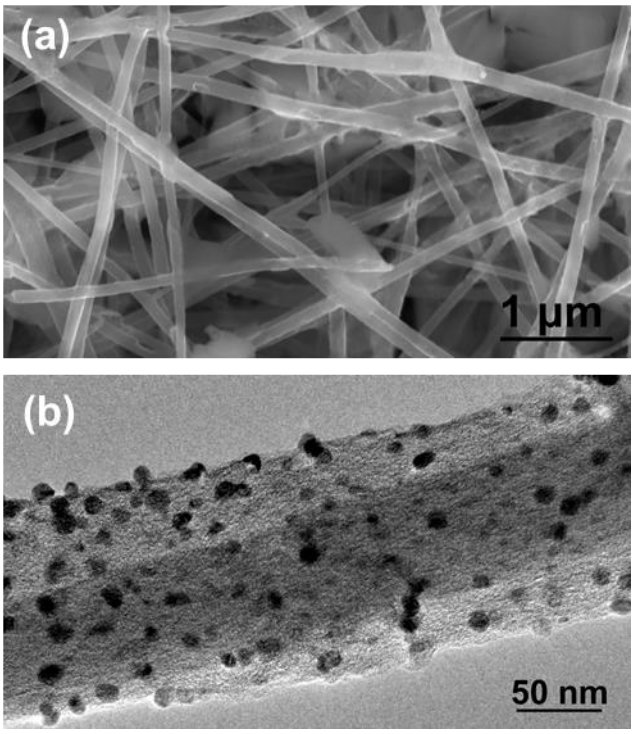

Figure 4-2. (a) Scanning electron microscope (SEM) image of the CNF film loaded with the cobalt precursor salt. (b) Low-magnification TEM image of the Co@graphene nanoparticle anchored onto the CNF substrate.

Transmission electron microscopy (TEM) images, shown in Figure 4-3a, are typical examples of Co nanoparticles with coatings of 1 to 3 graphene layers

respectively. Dimensional statistics of the nanoparticles (Figure 4-3b) conform to a typical Gaussian distribution with particle diameters ranging from 4 nm to 30 nm. Figure 4-3c illustrates the distribution for the core-shell nanoparticles produced by the high temperature pulse technique, with characteristic graphene shells from 1 to 3 layers thick.

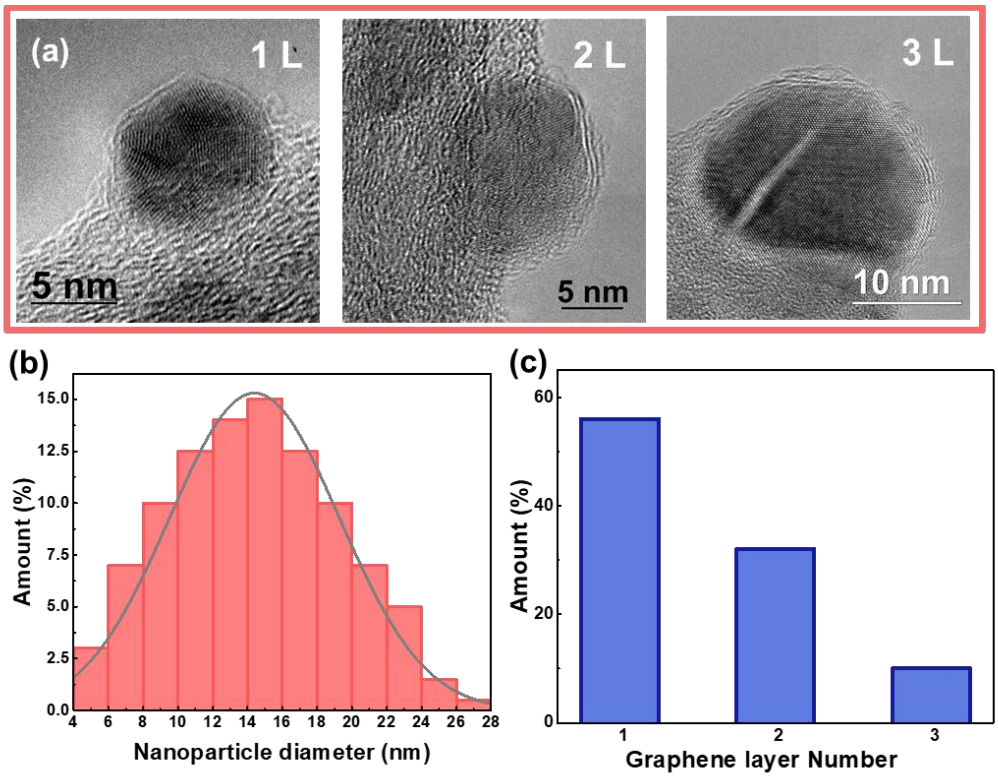

Figure 4-3. (a) TEM images showing graphene coatings composed of 1 to 3 layers, respectively, on Co nanoparticles. (b) Distribution plot showing the range in (Co) nanoparticle diameters. (c) Graphene coating layer distribution plot for the core-shell Co@graphene nanoparticles.

It is noted that a strong correlation between the number of graphene layers and the nanoparticle size can be found based on the statistics: the nanoparticles with smaller size tend to maintain a single graphene layer, whereas bilayer and trilayer graphene

shells are often observed for relative larger nanoparticles (Figure 4-4). This interesting phenomenon offers insight into the rearrangement mechanism of the carbon/Co clusters during the transient high temperature exposure.

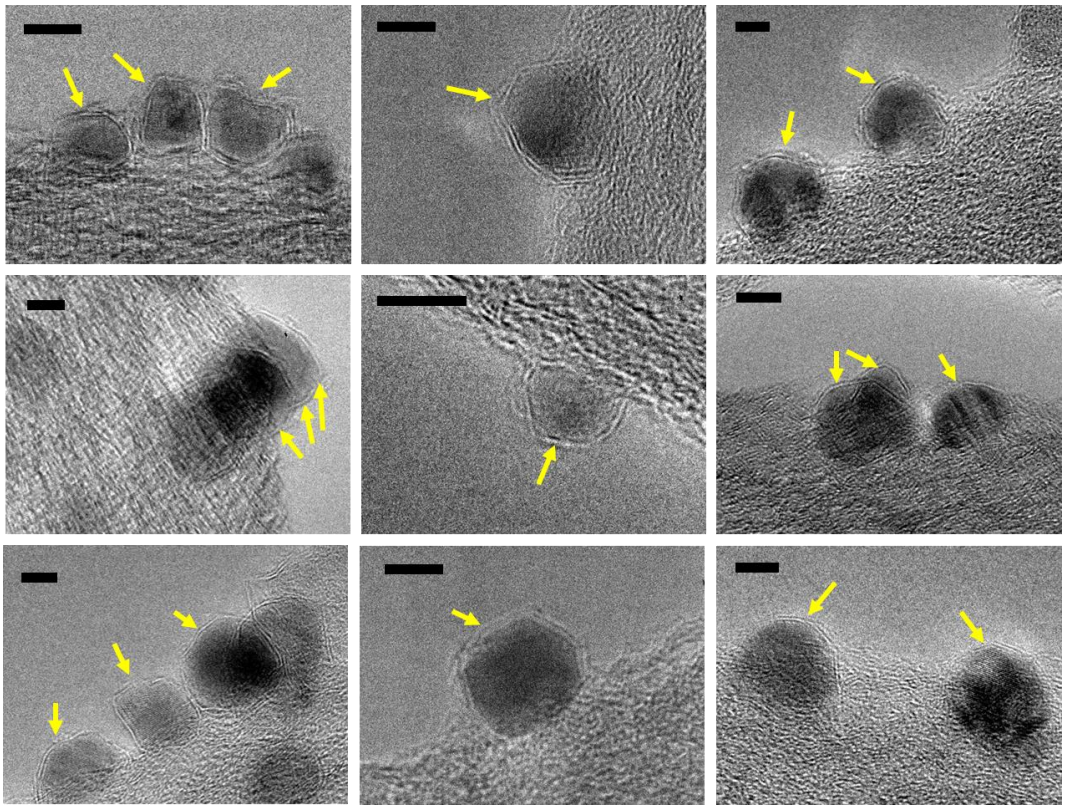

Figure 4-4. Examples of Co nanoparticles with graphene layers less than 3 (Scale bar: 5 nm), at a pulsing temperature around 1500 K with a time span of 50 ms. The optimized parameters guarantee the graphene layers were well controlled under 3.

Our hypothesis is that the quench rate has an influence on the layer numbers, as a slow cooling rate can extend the carbon atom deposition process on the surface of nanoparticles. As a result, more carbon atoms were stacked to form thicker graphene layers, along with the growth of nanoparticles. The hypothesis may explain the correlation between the graphene layer number and particle dimensions, which further

prove that the graphene thickness is controllable with this technique. We tuned the processing parameters and employed a high temperature pulse with a prolonged duration around 500 ms. Accordingly, the metallic clusters become agglomerated with nanoparticles on the order of 100 nm in diameter. As expected, the graphene shell increases in thickness to approximately 10 layers (Figure 4-5).

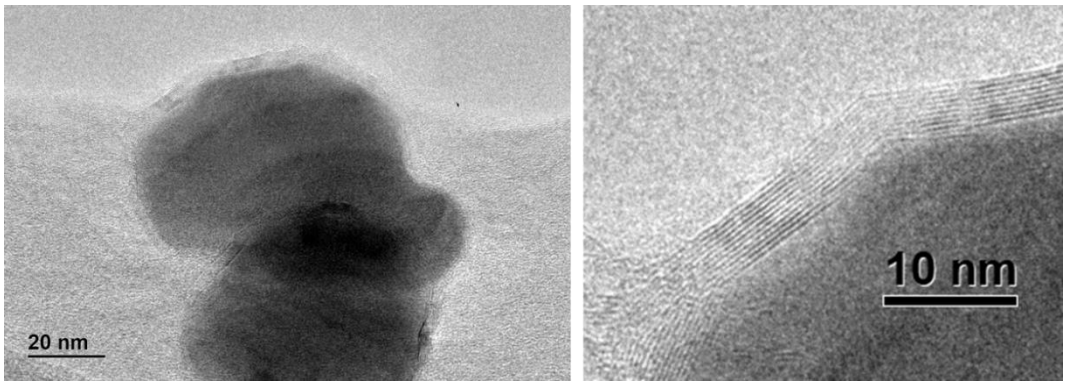

Figure 4-5. Co nanoparticles with dimensions around 100 nm coated with around 10 layers of graphene. Increasing the thermal pulse duration to 500 ms helps increase the nanoparticle dimension and graphene thickness, proving the controllable correlation between graphene layer number and nanoparticle sizes.

Note that the graphitization of carbon atoms is also influenced by the pulsing temperature, since high temperature can help the graphitization process, while lower local temperature decreases the kinetics and is not elevated enough to furnish migration energy to form crystalized graphitic structure. As a result, a thick amorphous carbon coating can be observed on the surface of the Co nanoparticles after a prolonged thermal pulse (Figure 4-6).

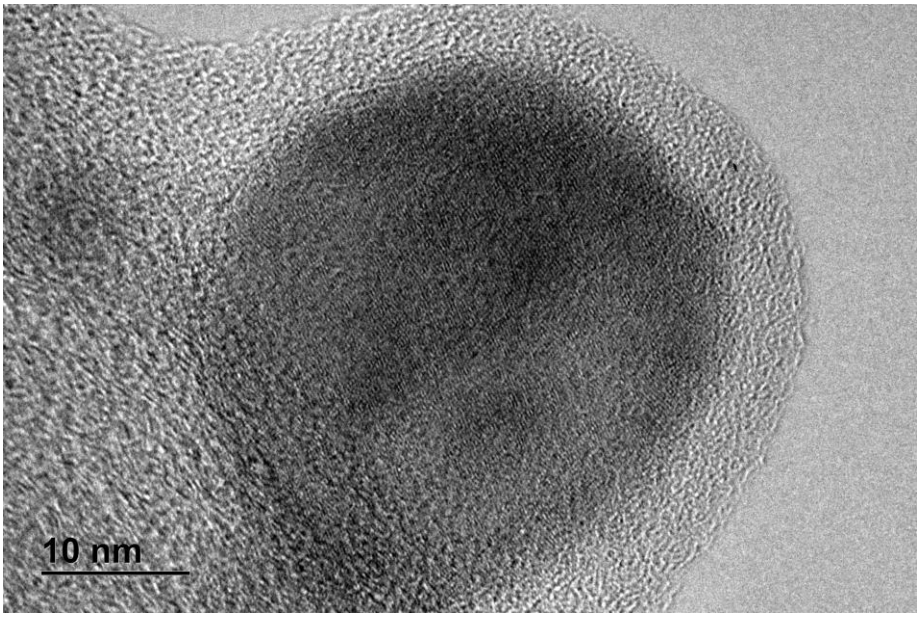

Figure 4-6. Amorphous carbon coatings on Co which form due to the lower temperature of 1300 K induced by the 500 ms pulse. The lower temperature could not offer enough energy for carbon atoms to form a crystalized graphene structure. To form graphene layers, a relatively higher temperature (above 1400 K) should be achieved.

Figure 4-7a illustrates the X-ray diffraction pattern in which peaks at 44.22°, 51.52°, and 75.85° are attributed to the (111), (200), and (220) planes of the Co nanoparticles, corresponding to a face centered cubic (fcc) structure (Fm $\bar{3}$m). The peaks consist well with our simulation result with an average size of 15nm (Figure 4-7b).

Note that cubic Co is the high temperature phase which can be successfully preserved due to the rapid quenching process (~30,000 K/s). The graphene-coated Co nanoparticles also exhibit good chemical stability, as no obvious oxidation was observed after 2 h heat treatment in air at 200 °C (Figure 4-8).

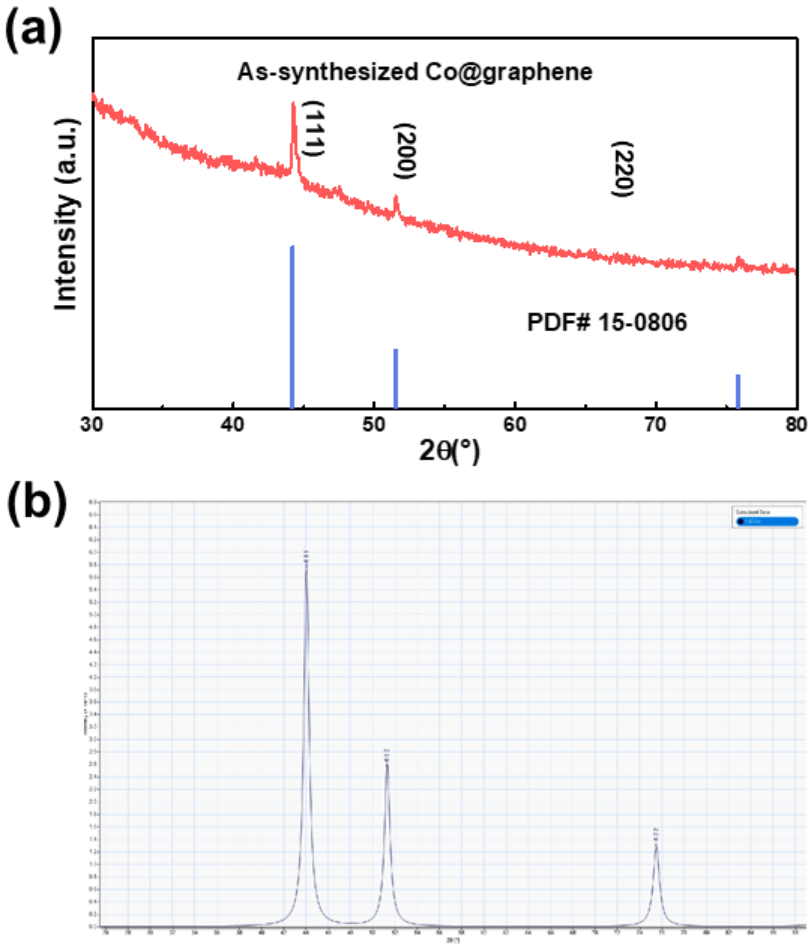

Figure 4-7. (a) XRD pattern for the Co@graphene core-shell nanoparticles. (b) Simulated XRD pattern with Co nanoparticle dimension of 15nm

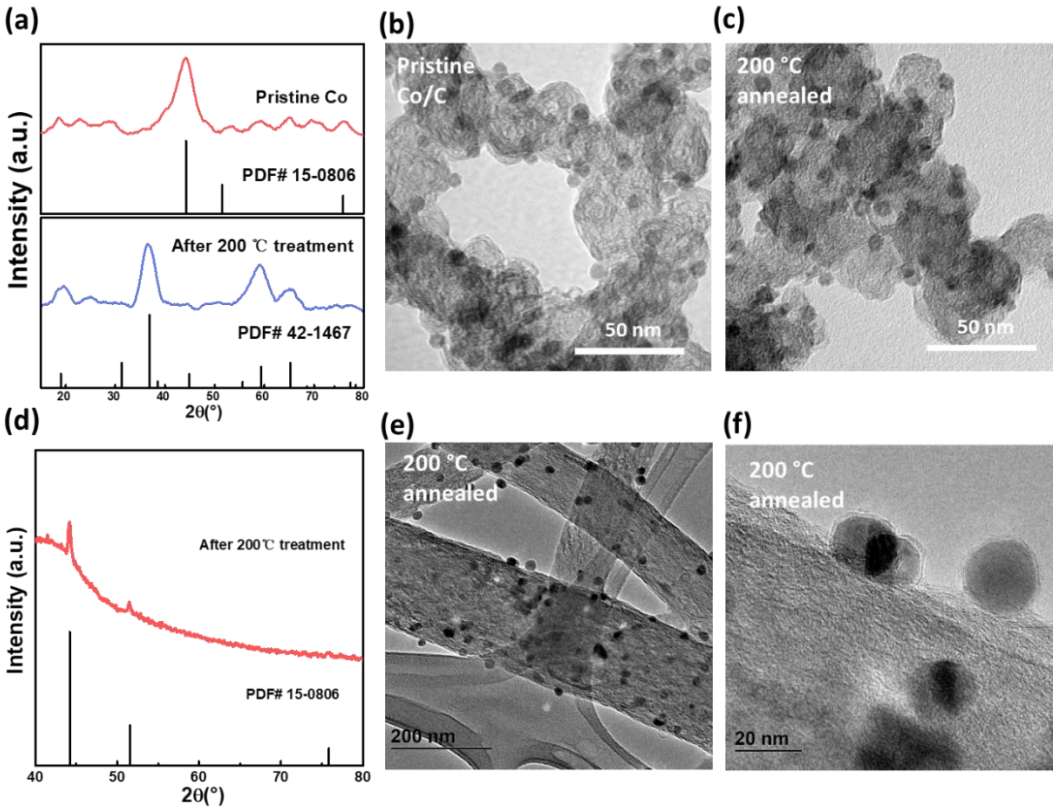

Figure 4-8. Chemical stability study for Co@graphene and Co/C. (a-c) XRD patterns and TEM images collected on Co/C before and after 2 h of annealing in air at 200 °C. The Co nanoparticles were oxidized to Co3O4 as indicated by the XRD pattern. (d-f) XRD pattern and TEM images collected on Co@graphene after 2 h of annealing in air at 200 °C. The metallic phase and the core@shell nanostructure were preserved due to the protection by the graphene shell.

Figure 4-9a depicts high resolution (HR-) TEM analysis, together with the selected area electron diffraction pattern (Figure 4-9b) showing that the Co nanoparticles are cubic (fcc) structure, which coincides with the aforementioned XRD pattern. The characteristic Co peaks confirm the formation of metallic Co nanoparticles from the precursor salt (Co atomic ratio: around 3.2%). Figure 4-9c presents the

electron energy-loss spectroscopy (STEM-EELS) elemental mappings of the Co@graphene nanoparticles. It is evident that the nanoparticles formed by high temperature pulse are core-shell structures, with cobalt and carbon atoms displayed in red and green, respectively. We can assume that the Co nanoparticles act as catalytic centers, which promotes the growth of graphene layers epitaxially on the nanoparticle surface.

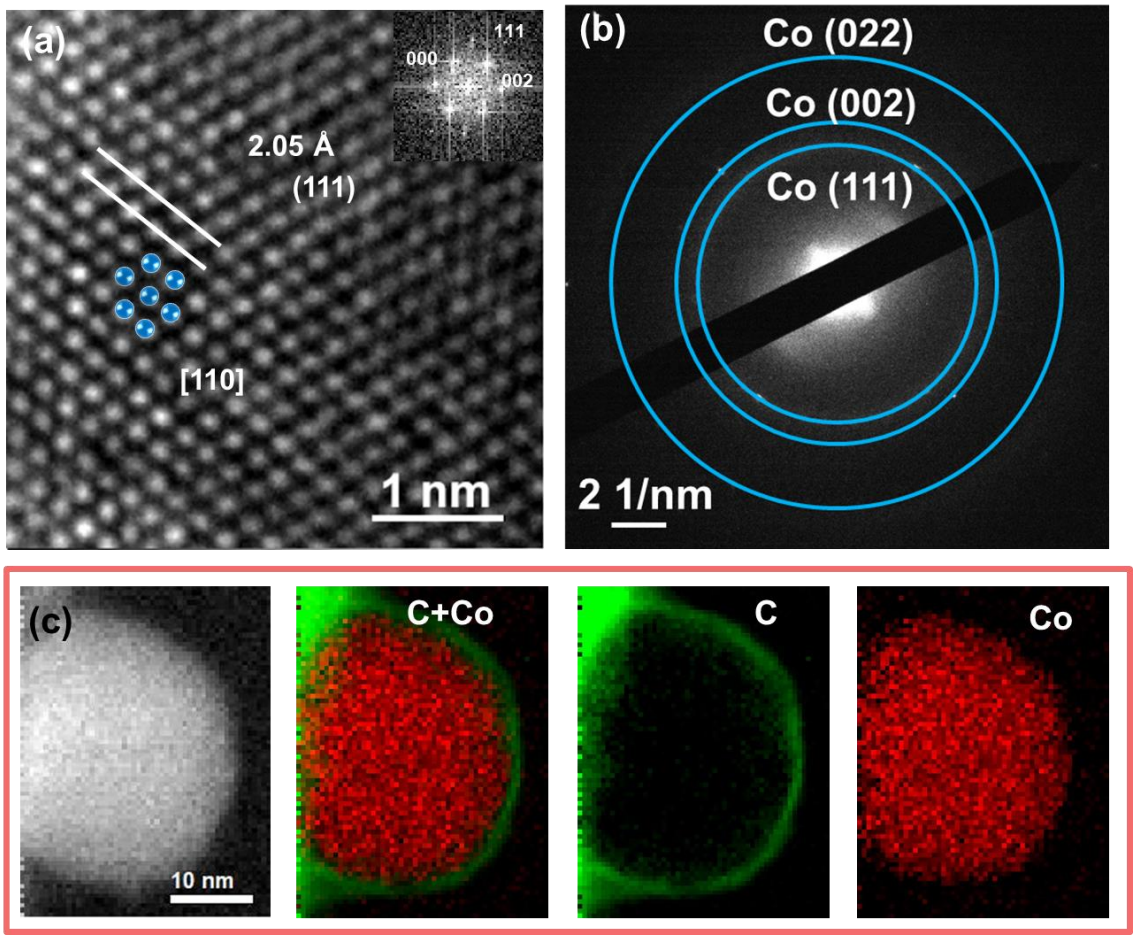

Figure 4-9. Compositional analysis of the Co@graphene nanoparticles. (a) HR-TEM analysis of the lattice of nanoparticles. (b) Selected area electron diffraction pattern shows the fcc structure of Co nanoparticles. (c) STEM-EELS maps of the core-shell nanoparticles.

X-ray photoelectron spectroscopy (XPS) spectra of the core-shell supported nanoparticles are shown in Figure 4-10. XPS analysis was employed to differentiate the composition variation of nitrogen for samples with and without N-doping (Figure 4-10b and c). The sample from precursors with melamine as N-source presents a significant increase in pyridinic N (398.0 eV), as well as the decrease of graphitic N (401.1 eV). It is noted that this composition shift should be attributed to formation of N-doped thin graphene layer superimposed on the Co nanoparticles.

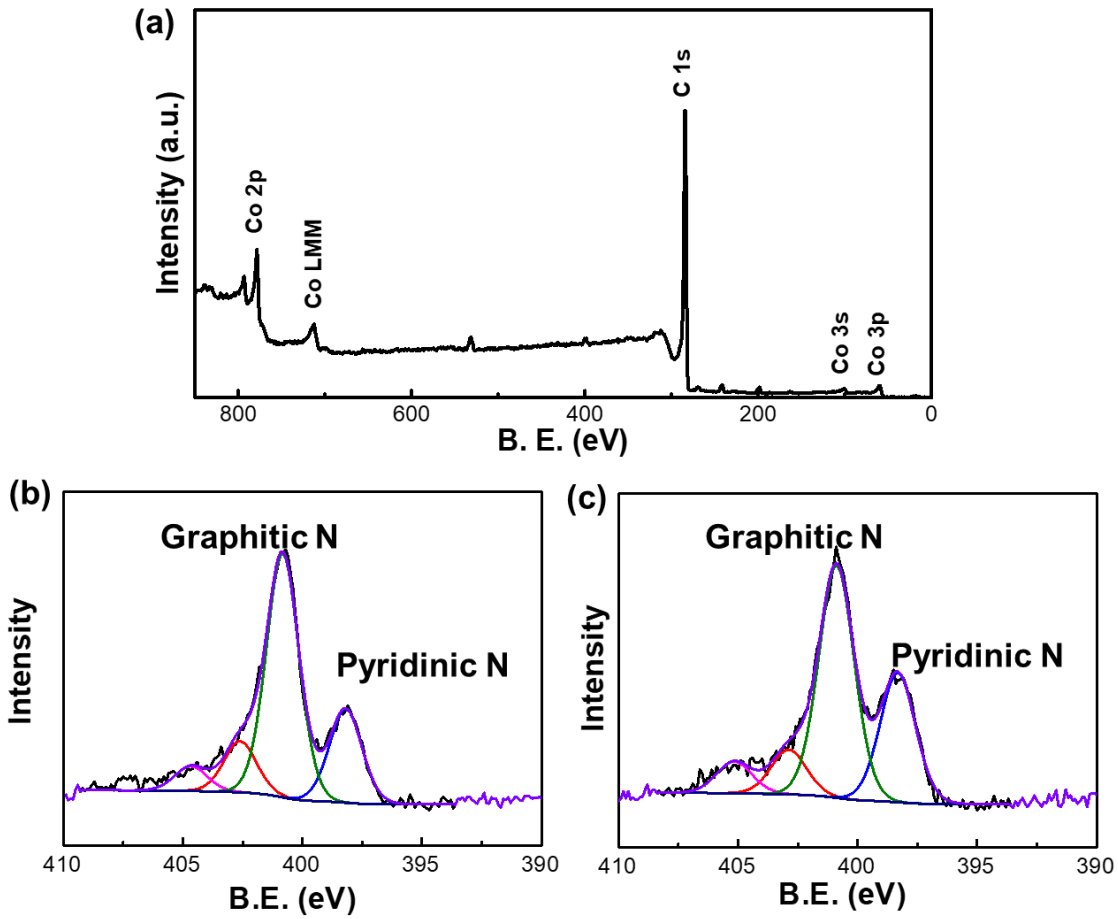

Figure 4-10. (a) XPS spectrum of the supported Co@graphene core-shell nanoparticles. XPS N 1s peaks for sample without (b) and with (c) melamine N-doping. The N element without melamine doping comes from the carbonized polyacrylonitrile nanofibers. After the Nitrogen doping, the ratio of pyridinic N v.s. graphitic N increased from 0.385 to 0.557, which is owing to the N-doping of the ultrathin graphene on Co nanoparticles.

As a demonstration of the functional applications, we performed electrocatalytic studies on the graphene-coated Co nanoparticles (denoted as N-Co@graphene and Co@graphene) for the oxygen reduction reaction (ORR), the cathode reaction in fuel cells. As a control, Co nanoparticle supported on high-surface-area carbon black (denoted as Co/C, see method section for the details of catalyst preparation) was also evaluated under similar conditions. The electrocatalytic studies were performed using the rotating disk electrode (RDE) method in 0.1 M KOH. Figure 4-11 shows the voltammograms recorded in Argon and oxygen-saturated electrolytes. No pronounced peaks were observed in the Ar-saturated electrolyte for all three catalysts. When the electrolyte is saturated with O_2, a pronounced oxygen-redcution peak appears in the cathodic scan. The onset potential of this peak is positively shifted by 100 mV and 60 mV for N-Co@graphene and Co@graphene as compared to Co/C. Correspondingly, the peak current for N-Co@graphene and Co@graphene was also found to be as high as 1.5 – 1.7 times of that for Co/C.

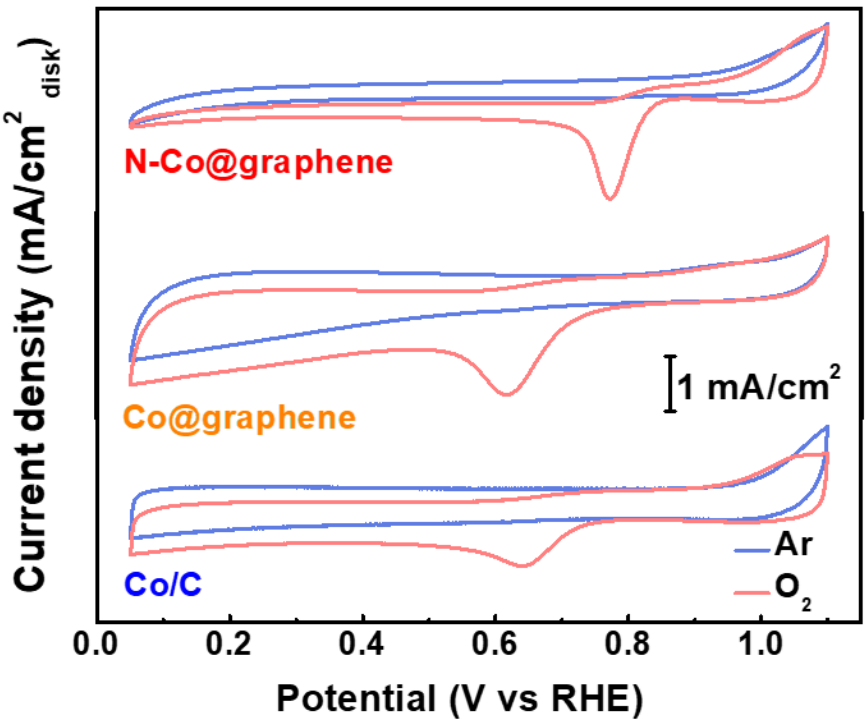

Figure 4-11. Voltammograms recorded for N-Co@graphene, Co@graphene and Co/C in Ar- and O2-saturated 0.1 M KOH.

These results indicate that graphene coated cobalt nanoparticles are much more active than Co/C for the ORR, which is further confirmed by the ORR polarization curves measured with disk rotation (Figure 4-12a). At 1600 rpm, N-Co@graphene and Co@graphene reaches a diffusion-limited current of ~4.9 mA/cm^2, which is high for platinum group metal (PGM)-free electrocatalysts,[97–99] as compared to 4.4 mA/cm^2 by Co/C. The more facile reaction kinetics of N-Co@graphene was confirmed by its low Tafel slope in kinetic region (Figure 4-12b). The high activity of graphene coated cobalt nanoparticles for the ORR can be ascribed to the synergy between the metallic Co core and the ultrathin graphene coating (<3 atomic layers in thickness), which may stabilize oxygenated adsorbates (e.g., *OOH and *OH, where * denotes an adsorption site on the catalyst surface) on the surface due to the strong coupling between and

hybridization of the sp^2 and *d*-orbital electrons of graphene and cobalt, respectively[100–102]. More specifically for N-Co@graphene, its activity could be further enhanced by Co-N species that facilitates formation of HO_2^- according to dual-site mechanism[103].

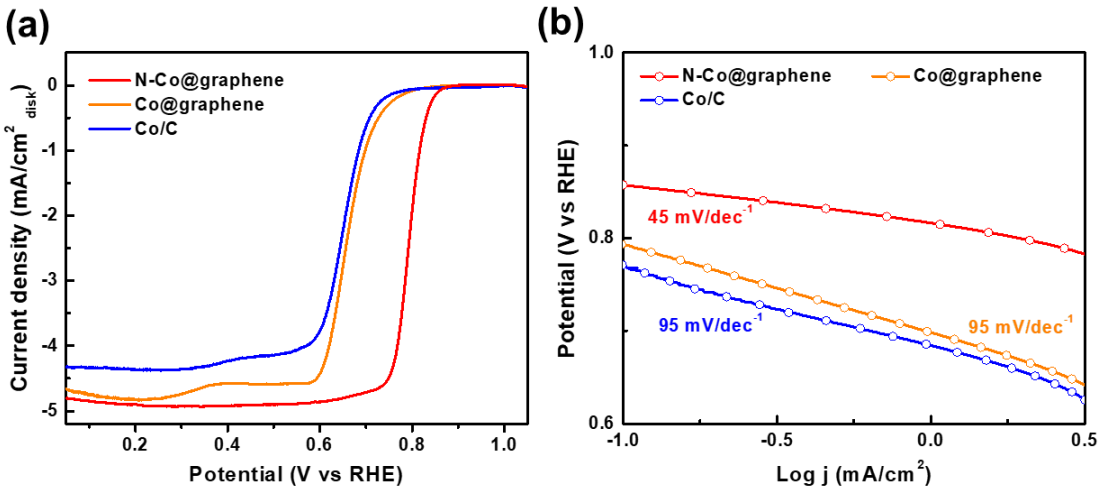

Figure 4-12. (a) ORR polarization curves at 1600 rpm and (b) corresponding Tafel plots.

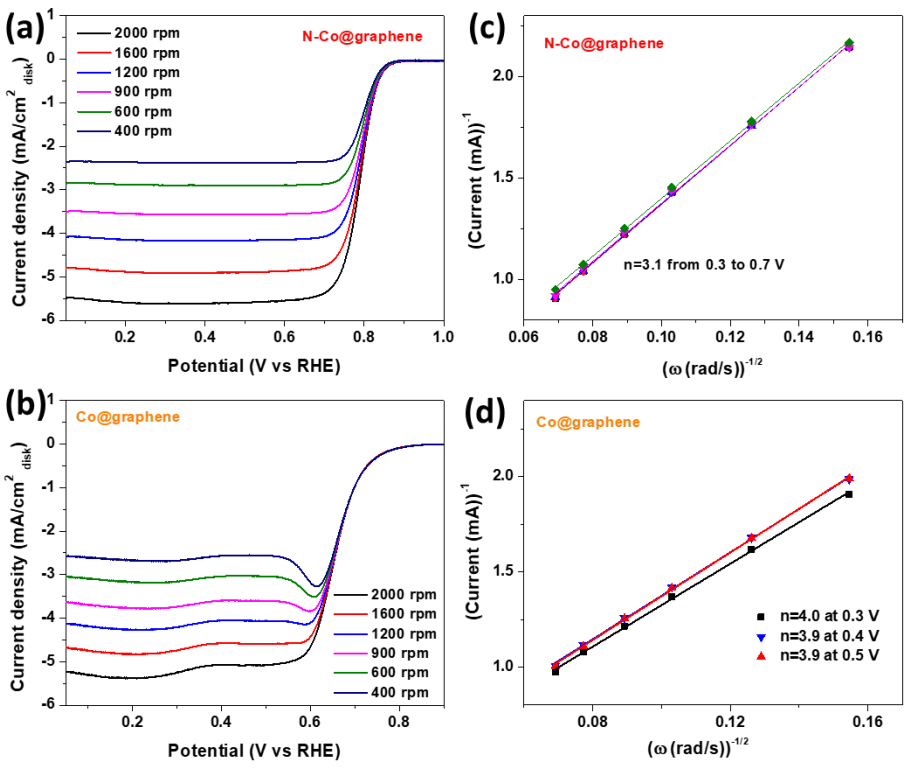

Figure 4-13. ORR polarization curves recorded at various rotation rates for N-Co@graphene (a) and Co@graphene (b), with the corresponding Koutecky-Levich plots shown in (c) and (d), respectively.

It is noted that the Co@graphene nanoparticles were found to be highly durable for the ORR, with negligibile degradation after 3,000 potential cycles between 0.6 and 1.0 V (Figure 4-14). Such a high durability is superior to most of the PGM-free electrocatalysts reported in the literature, comparable to some of the precious metal-based electrocatalysts (e.g., Pt and Pd).[104,105]

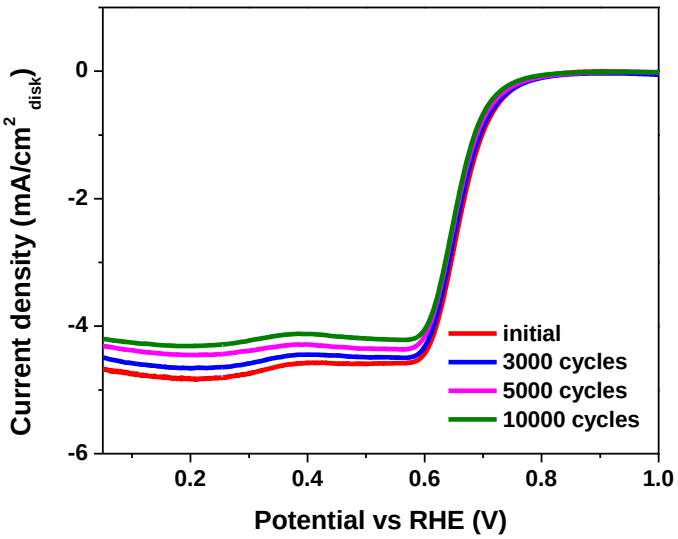

Figure 4-14. Durability study for the Co@graphene catalyst subjected to potential cycles between 0.6 and 1.0 V at 50 mV/s.

TEM images collected after the durability study showed that the nanoparticles maintained their core-shell nanostructure (Figure 4-15), which is in line with the high chemical durability as discussed above (Figure 4-8). The excellent chemical stability and electrocatalytic durability of graphene coated cobalt nanoparticles could be attributed to protection of the metal core by the carbon shell, which has prevented the metal element from oxidation and leaching.[102]

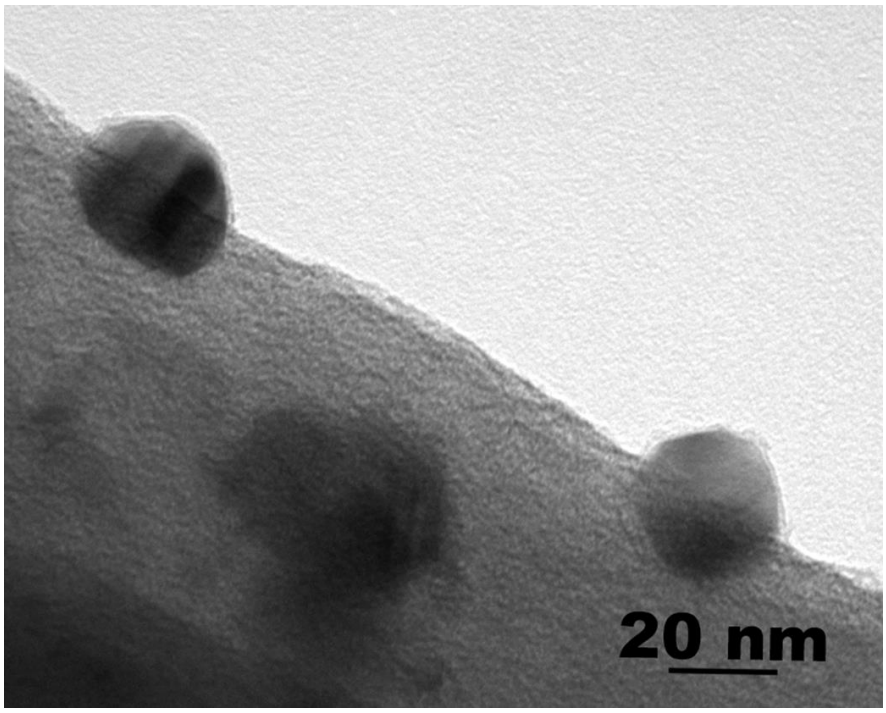

Figure 4-15. TEM images for nanoparticles after polarization cycles, in which the core-shell structure remains intact.

To understand the origin of the observed activity and stability of Co@graphene core-shell catalysts for ORR, first-principles density functional theory (DFT) calculations were performed to reveal the interactions between thin graphene layer and Co nanoparticles. As shown in Figure 4-16, the Co@graphene catalysts were modelled as a perfect graphene layer on top of a four-atom tetrahedral Co cluster, representing a local contact of graphene shell with the atomic islands on the surface of Co nanoparticle cores, through which electron charge transfer happens between the core (Co) and shell (C atoms). The calculated charge density difference map (Figure 4-16) shows that the carbon atoms adjacent to the Co cluster would have lower electron density than the carbon atoms in other regions. Especially, the carbon atom marked with the dashed-

circle in the figure was found to exhibit the greatest degree of electron density depletion and act as active site of the catalyst for ORR.

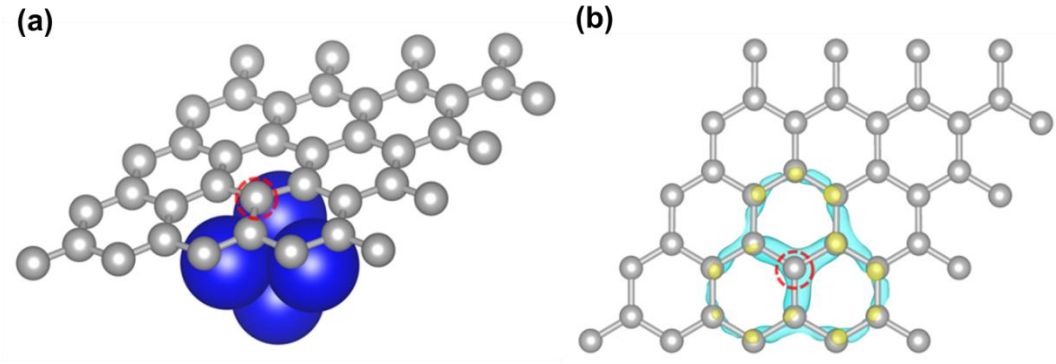

Figure 4-16. (a) Structure of a graphene layer in contact with a four-atom Co cluster, which was used to model Co@graphene catalysts. In the figure, the gray balls represent C atoms and the blue balls represent Co atoms. (b) Predicted electron density change on the carbon atoms induced by the local contact between Co cluster and graphene layer. Isosurface level is set as $0.05e\text{Å}^{-3}$. Color yellow and cyan indicate electron accumulation and depletion, respectively.

Moreover, we predicted the configurations (Figure 4-17) and energies (Table 4-1) of ORR species (including O_2, OOH, O, OH, HOOH, and H_2O) adsorbed on the top of this active carbon site. Based on these DFT results, we applied the computational hydrogen electrode method developed by Nørskov *et al*.[106] to calculate the free energy evolution of a four-electron (4e-) ORR pathway on the Co cluster induced active carbon. Following this pathway, The ORR starts with an O_2 molecule adsorption, followed with O_2 protonation to form OOH, which dissociates into O and OH, and ends with O and OH protonation to form two H_2O.

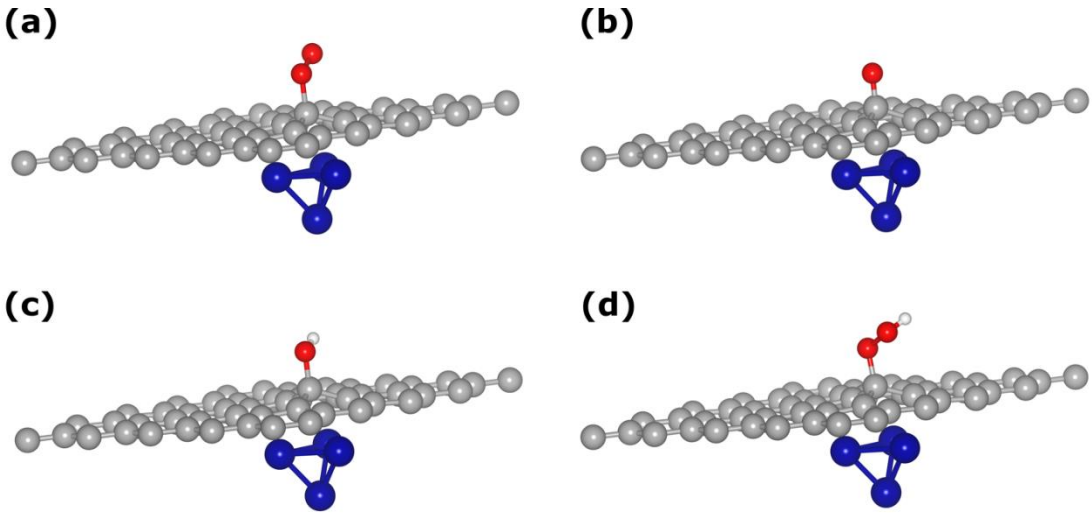

Figure 4-17. Optimized structures of O_2, O, OH and OOH adsorption on an active carbon atom of a graphene layer. In the figure, the grey, blue, red and blue balls represent C, Co, O and H atoms, respectively.

Table 4-1. Predicted adsorption energies of various ORR species on Co@graphene catalysts. The adsorption energies were calculated as the difference in energy between the adsorption system and the corresponding isolated systems. Hence, negative value of the adsorption energy indicates attractive interaction between the ORR species and ORR active sites.

E_{ad} (eV)	Co@graphene
O_2	-0.06
O	- 3.38
OH	- 2.51
OOH	- 1.13
H_2O	0.00

The calculated free energy evolution was presented in Figure 4-18. When the electrode potential U is lower than a limiting potential of 0.57 V, all the elementary reactions involving charge-transfer become exergonic and thermodynamically favorable on the active carbon. Consequently, our DFT calculations proved that local contact between Co core and graphene shell could produce carbon atoms with lower electron density than other carbon atoms of the graphene layer, and these carbon atoms with depleted electron density could promote $4e^-$ ORR. This synergic effect can also explain the stability and durability of nanoparticles, since there is no direct contact between Co and O atoms in the ORR process, in which the graphene layer acts as an electron messenger involved in the interactions between Co and O atoms.

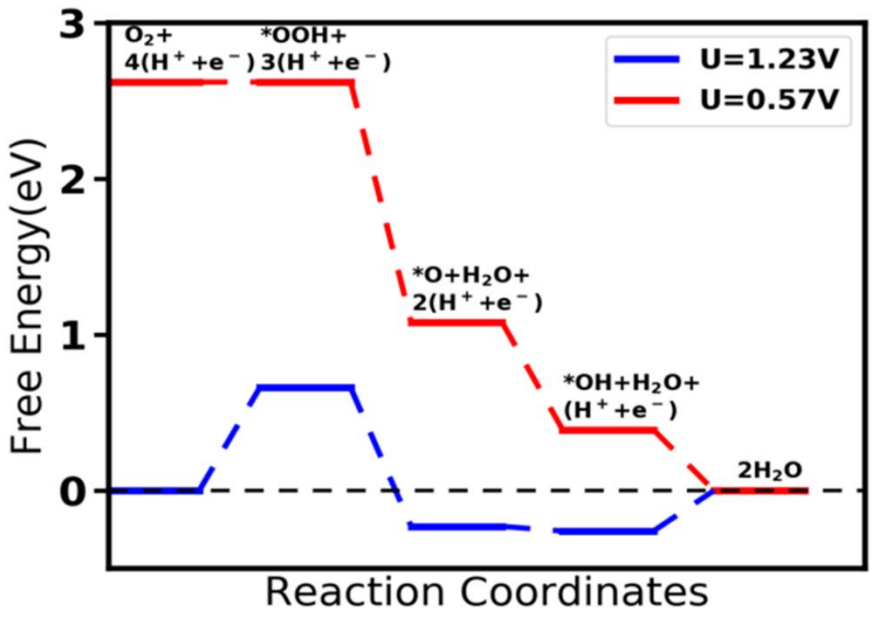

Figure 4-18. Calculated free energy evolution diagram for the ORR through 4e- associative pathway on the active carbon sites.

This one-step strategy for synthesis of graphene protected nanoparticles also presents its universality, which can be applied to other transition metal elements as well. Figure 19a, b and Figure 4-20 present the TEM morphologies and XRD patterns of iron and nickel-based core-shell nanoparticles, the structures and dimensions of which show similar results to the Co@graphene nanoparticles.

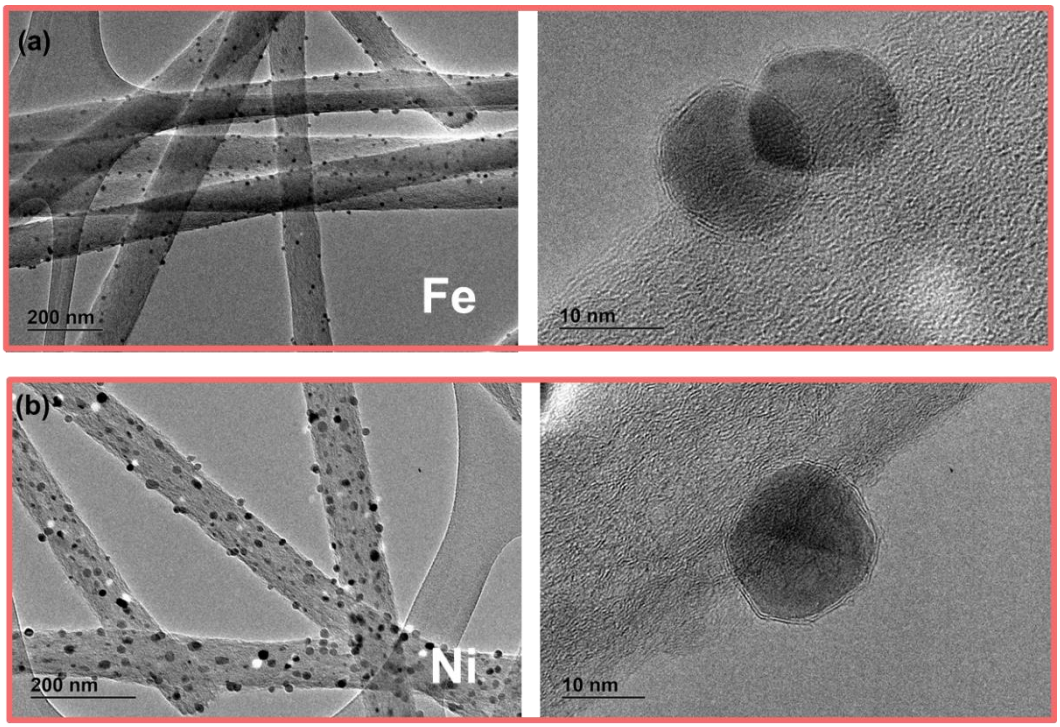

Figure 4-19. (a) Morphology of iron@graphene core-shell nanoparticles. (b) Morphology of nickel@graphene core-shell nanoparticles. TEM images show the existence of ultrathin graphene layers, which proves universality of this high temperature pulsing technique for many transition metals.

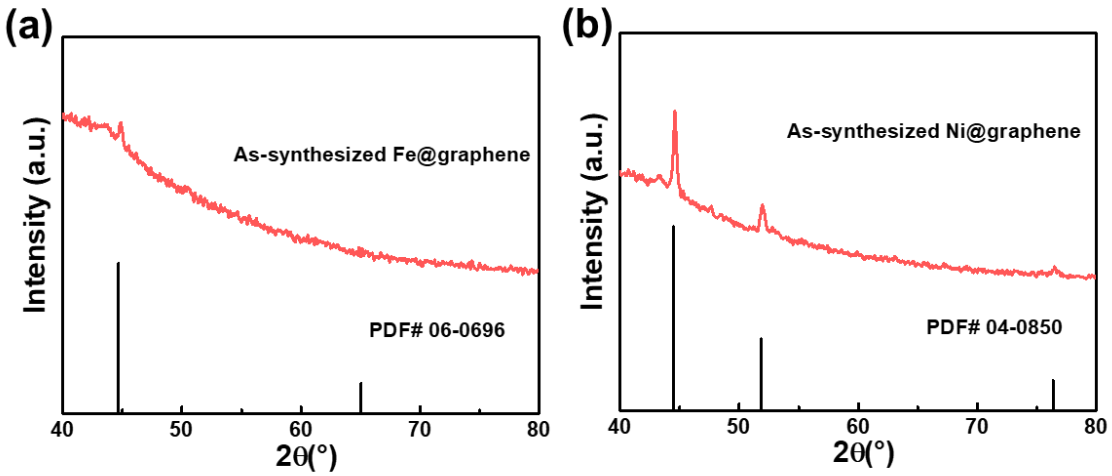

Figure 4-20. Fe (a) and Ni (b) XRD patterns.

Besides, there is a broad range of carbon-based substrates that enable this high temperature pulsing technique. Apart from two-dimensional (2D) CNF thin film (Figure 4-21a), a block of three-dimensional (3D) carbonized wood can also function as the substrate to generate core-shell nanoparticles. The 3D carbonized wood layer consists of aligned open channels (diameter of tens of micrometers) that can act as a chamber to accommodate the pristine salt and the deposition surface where the as-formed core-shell nanoparticles can get anchored (Figure 4-21b). The SEM images shows that all the channels are filled with the homogeneously dispersed Co@graphene nanoparticles. The inexpensive wood substrate can be utilized as a large-scale manufacture substrate, which can tremendously increase the loading amount of nanoparticles with a facile large scale manufacturing.

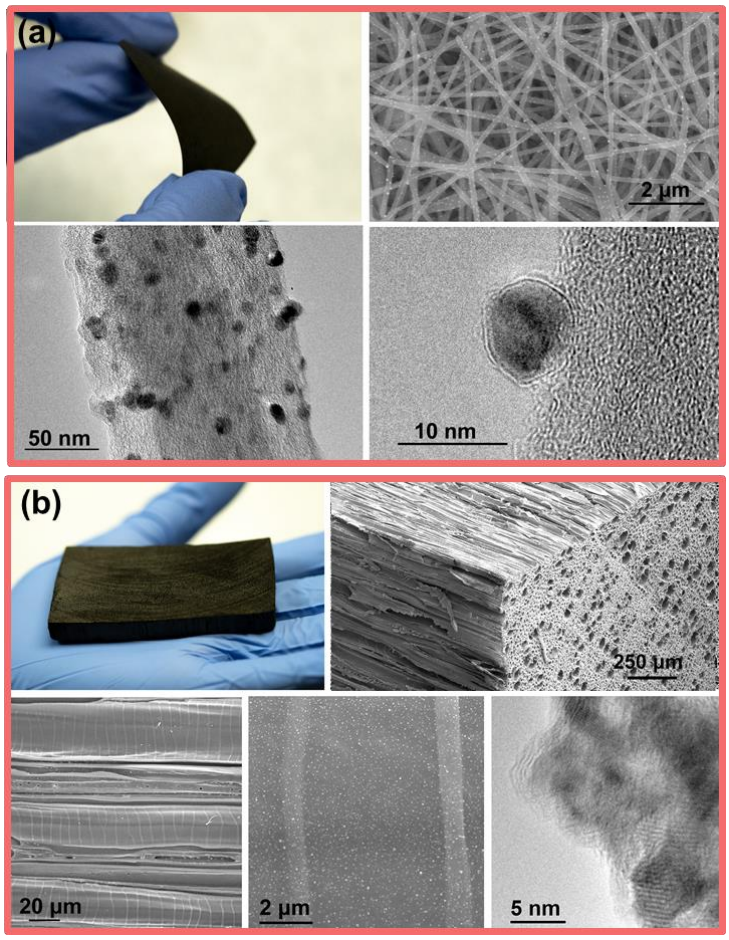

Figure 4-21. (a) CNF as the supported substrate (b) Carbonized wood as the supported substrate.

4.4 Conclusion

We report a one-step synthetic technique to simultaneously fabricate supported Co@graphene core-shell nanoparticles. This strategy presents several advantages, such as generation of core-shell nanostructures in one facile processing step, tunability and control over graphene shell thickness down to monolayer graphene, as well as the abundance of substrate candidates. The ORR test shows that their stability and

durability exceeded previously reported PGM-free catalysts. DFT calculations proved that local contact between Co core and graphene shell produces carbon atoms with lower electron density which promote ORR process. This facile synthetic approach provides a pathway towards the design and development of metal/graphene core-shell nanoparticles with controllable graphene coating thickness for a wide range of potential applications in the fields of catalysis and beyond.

4.5 Experimental

Preparation of CNF

An 8% by mass solution of polyacrylonitrile (PAN) (Sigma Aldrich) in dimethylformamide (DMF) was electrospun at a voltage of 10 kV, a spinning distance of 15 cm, and a feeding rate of 1 mL/hour. The as-spinned nanofibers were collected by a rotation drum at a speed of 80 rpm. The electrospun film was then converted into CNFs after stabilizing in air at 280°C for 5 h and carbonizing at 600°C in an argon atmosphere.

Fabrication process of supported core-shell nanoparticles

Cobalt (II) chloride ($CoCl_2 \cdot 6H_2O$) salt was dissolved in ethanol to form a 0.05 mmol/mL solution. The precursor solution was dropped onto the CNF or carbonized wood substrate in a controlled manner. The as-prepared film was then connected to copper electrodes and silver paste was employed to glue the carbon substrate to the electrodes. A high temperature pulse was applied to the substrate in an argon-filled glovebox using an external Keithley 2425 Source Meter. The emitted light from the

substrate was collected by a high-speed spectrometer camera and fitted using the blackbody radiation equation.

The emission spectrum of the CNF film during the high temperature pulse was recorded with a high-speed camera, from which the temperature can be evaluated through black-body radiation analysis. The light emission intensity during the pulse period and the corresponding temperature vs. time curves including the heating and cooling process can be also be acquired.

Preparation of Co/C control sample

Co nanoparticles were synthesized following a slightly modified reported method.[107] Briefly, 100 ul oleic acid, 160 ul dioctylamine and 15 ml of dichlorobenzene were slowly heated to boiling point of dichlorobenzene (~ 182 °C). To this solution, 100 mg of dicobalt octacarbonyl dissolved in 3 ml dichlorobenzene were injected. The mixture was kept at ~ 182 °C for 15 minutes before cooled down to room temperature. Co nanoparticles were recovered by adding ethanol and centrifuging. The sediment was dispersed in toluene before adding ethanol and centrifuging again. The resulting product was dispersed in toluene. To make the Co/C catalyst, high surface area carbon (Tanaka Inc.) was added into cobalt dispersion before ultrasonication for 30 minutes. Cobalt weight loading on carbon was controlled to be ~ 18% to be consistent with Co@graphene. To remove organic surfactant on Co, ethanol was added into the above dispersion before it was centrifuged. Sediment was dispersed in hexane and centrifuged again. Co/C catalyst was acquired by drying sediment under vacuum for 20 minutes.

Materials characterization

The low-magnification morphological images of the carbon substrates were acquired using a field-emission SEM (Tescan XEIA FEG SEM). TEM at an accelerating voltage of 200 kV to was used to characterize the nanoparticle morphologies at high resolution. Atomic resolution TEM images as well as EELS maps were also obtained. XPS analysis was performed on a multi-technique photoelectron spectrometer with a standard dual (Mg/Al) anode and monochromatic (Al) X-ray sources. The XRD pattern in supporting information for control sample was achieved by PANalytical X'Pert Powder X-Ray Diffractometer. All other XRD patterns were achieved using a D8 Bruker Advanced X-ray Diffraction system.

Electrode preparation

Both Co@graphene and Co/C were mixed in aqueous solvent containing 0.05% Nafion and 10% isopropanol with a concentration of 1 mg/mL. The mixture was ultrasonicated for at least 30 minutes to achieve a homogeneous ink. The ink was then drop-casted onto a 5 mm diameter glassy carbon rotating disk electrode and allowed to dry to form a uniform catalyst film. Total catalyst loading, including the Co and carbon, was 0.2 $mg/cm^2_{disk.}$

Electrochemical measurements

Electrochemical tests were conducted with a Metrohm Autolab PGSTAT302N potentiostat connected to a three-electrode cell made with Teflon. Hg/HgO and platinum wire were adopted as the reference and counter electrodes, respectively. 60 mL of 0.1M KOH was prepared with de-ionized water and implemented as the electrolyte. Polarization curves were measured with a scan rate of 50 mV/s.

The electron transfer number during ORR was calculated based on the Koutecky-Levich equation:

$$\frac{1}{J} = \frac{1}{J_L} + \frac{1}{J_K} = \frac{1}{B\omega^{1/2}} + \frac{1}{J_K}$$

where J, J_L, J_K are nominal, diffusion limiting and kinetic current density, respectively. The reverse of the K-L plot slope, B, is:

$$B = 0.2nF\nu^{-1/6}C_0D_0^{2/3}$$

where n is the electron transfer number, F is the Faraday constant (96485 C/mol), ν is the kinetic viscosity ($0.01 cm^2/s$), C_0 is the concentration of oxygen within the electrolyte (1.2 mmol/L), and D_0 is the diffusion coefficient of oxygen within the electrolyte ($1.9 \times 10^{-5} cm^2/s$).

Accelerated stability tests were conducted by cycling the electrode between 0.6 V and 1.0 V (vs RHE) at 50 mV/s in an oxygen-saturated electrolyte.

Computational method

The first-principles spin-polarized density functional theory (DFT) calculations[108,109] were performed using Vienna ab-initio Simulation Package (VASP)[110]. Projector augmented wave (PAW) pseudopotential[111,112] was used to describe the core electrons and energy cutoff was set as 400eV to expand the wave function. The Perdew-Burke-Ernzerhof (PBE) functionals[113] were used to describe the exchange-correlation effects. The atomic structures were optimized until the force was below 0.01eV/Å. The Brillouin zone was sampled with Monkhorst-pack[114] 4 × 4 × 1 k-points grids. A vacuum region of 14 Å was added into the simulation cell to avoid the interaction between two adjacent images. Zero-point energy (ZPE) corrections were included in all the reported adsorption energies.

4.6Supporting Information

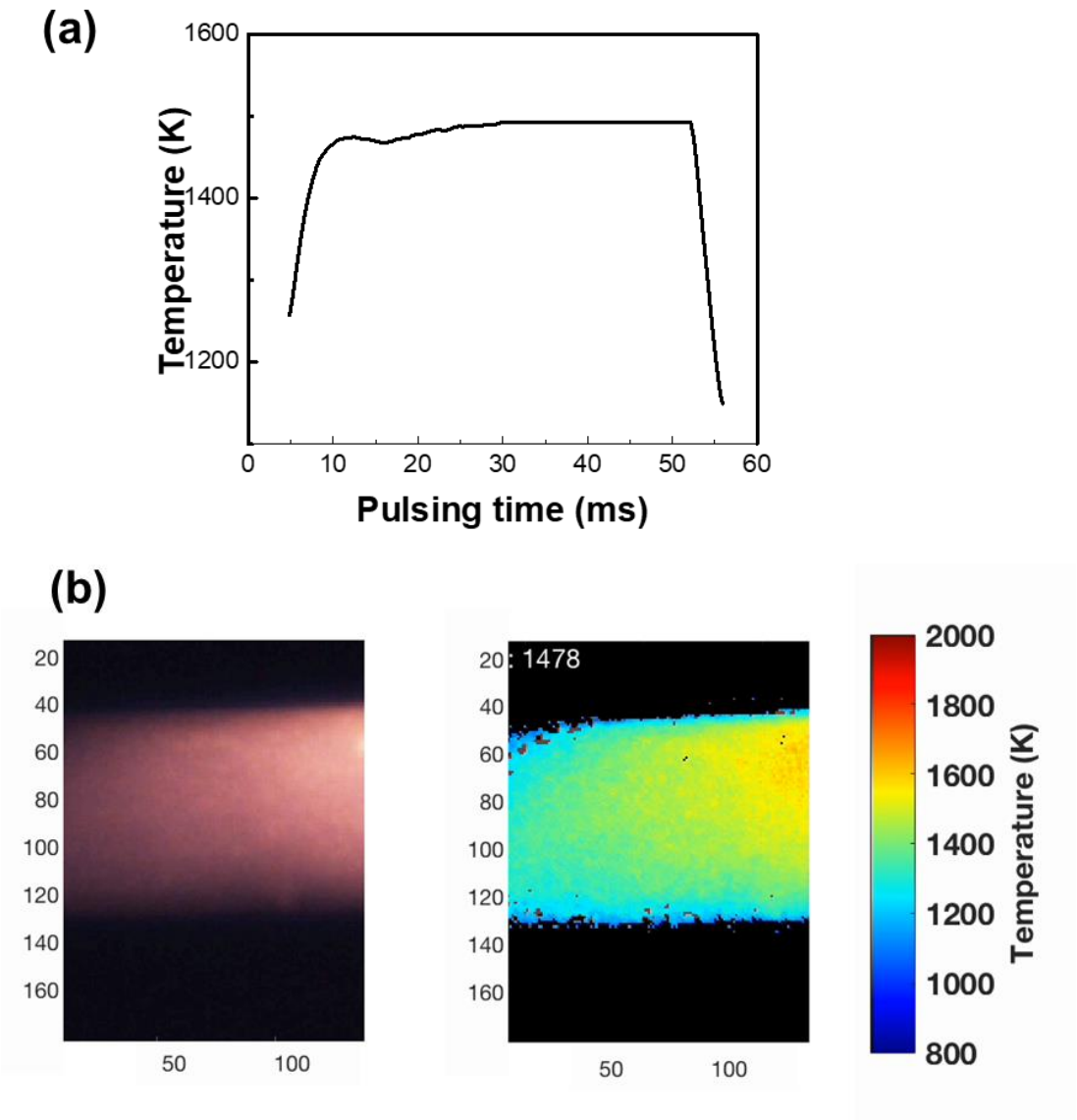

Figure 4-S1. Characterization of the Joule heating process. (a) Light emission spectra at different times from 0 to 60 ms, covering both the heating and cooling regimes of the 50 ms thermal pulse. (b) Temperature distribution at peak power with an average temperature of 1478 K.

Chapter 5: Universal Soldering of Lithium and Sodium Alloys on Various Substrates for Batteries*

5.1 Abstract

Developing safe batteries with high energy density is one of the most attractive goals for energy storage researchers. The high theoretical specific capacity of lithium (Li) metal and the non-flammability of solid state electrolytes (SSEs) make the solid state Li metal battery a promising option to achieve this goal. To make the switch from liquid to solid state electrolyte, the high interfacial resistance resulting from the poor solid-solid contacts between Li metal and SSEs needs to be addressed. Herein, we present a one-step soldering technique to quickly coat molten Li onto different substrates including metals, ceramics, and polymers. It is deduced that the surface energy and viscosity of the molten Li can be tuned by adding alloy elements, which improves the wettability against various substrates. When soldered onto the surface of garnet-based SSEs, the Li alloys exhibit significantly improved contact, which leads to an interface resistance as low as ~ 7 $\Omega \cdot cm^2$. While cycling under high loads, the alloy elements show some segregation from the newly plated Li. However, the newly plated Li still maintains tight contact with the garnet surface and demonstrates excellent electrochemical stability. Several Li binary alloys as well as a sodium (Na) binary alloys are successfully tested on various substrates to demonstrate the versatility of this soldering technique for potential battery applications.

* The results in this chapter have been published: Wang, C.※; Xie, H. ※; Zhang, L.; Gong, Y.; Pastel, G.; Dai, J.; Liu, B.; Wachsman, E. D.; Hu, L. Universal Soldering of Lithium and Sodium Alloys on Various Substrates for Batteries. *Adv. Energy Mater.* **2017**, *1701963*, 1701963.

5.2 Introduction

Lithium (Li) metal has attracted a lot of interest to develop high energy density energy storage devices because it boasts the lowest reduction potential (-3.05 V) and highest theoretical specific capacity (3860 mAh/g).[115–118] However, the widely-known issues, dendritic Li growth along with the flammability of liquid organic electrolytes, can cause serious safety problems and therefore inhibit Li metal batteries for practical applications. One of the most attractive and effective strategies to develop practical Li metal batteries is to use solid state electrolytes (SSEs) because of their non-flammability and mechanical strength to block dendritic Li growth.[119,120] Among the many SSEs studied,[121–128] the cubic garnet phase SSEs[46,129–134] are more attractive because of their excellent chemical stability,[135,136] high ionic conductivities,[47,129,130,137] and wide electrochemical potential window.[138–140]

One of the major challenges for the application of the garnet based solid state Li metal batteries is the poor interfacial contact between garnet SSEs and electrode materials.[47,141,142] Direct contact between Li metal foil and garnet pellets normally results in poor contact and large interfacial resistance. By adding a polymer interface[143,144] or applying pressure,[145,146] the Li and garnet interface can be improved marginally, but still has high resistance. The poor wettability of molten Li against garnet substrates also makes it unfeasible to directly coat Li metal on garnet SSEs. In our previous work,[147–150] the wettability of garnet pellets against molten Li was significantly improved by coating a modification layer on the garnet surface, and the

interfacial resistance was decreased from more than 1000 $\Omega \cdot cm^2$ to as low as 1-20 $\Omega \cdot cm^2$.[147,148] However, for large-scale practical applications, this additional surface modification step under high vacuum is time-consuming and an additional cost. Therefore, a lower cost and more effective method is still strongly desired to solve the interfacial problem between Li metal anode and garnet SSEs for practical solid state Li metal batteries.

Fundamentally, the poor wetting between molten Li metal and garnet pellets is due to the large difference in surface energy. Our previous strategy introduces new interfaces that have better wettability against molten Li but another strategy is to tune the surface energy of molten Li itself to match with the garnet SSEs. This wetting issue between liquid metals and ceramic substrates has been extensively studied for multiple applications, such as metal-ceramic joining by brazing and fabricating metal matrix composites.[151–153] To improve the wettability between liquid metals and ceramic substrates, alloying elements were normally added to tune the surface energy of the liquid metals and significantly decrease the contact angle on ceramic substrates.[151,153,154] Recently, with the rise in solid state Li metal batteries, the metal-ceramic contact has become a critical challenge towards the development of high energy density and safe energy storage devices.

Inspired by the strategies used in developing metal matrix composites and metal-ceramic joining, we successfully demonstrated a universal soldering technique that can quickly coat molten lithium or sodium metals onto different substrates for solid state batteries and other applications. By adding the alloying elements, both the surface energy and viscosity of the molten Li were increased.[155] The Li-rich molten alloys show

a much improved wettability on substrates including ceramics, metals, and polymers. To demonstrate this coating technique for solid state batteries, a molten Li-Sn alloy was successfully coated onto a fresh-polished garnet pellet in less than 10 seconds, much like a quick soldering step. The SEM images confirm the tight and conformal contact between the alloy and garnet surface, which results in an interfacial resistance as low as ~7 $\Omega \cdot cm^2$. The Li plating-stripping cycling further demonstrate the stability of the Li-rich alloy anode and its interface with garnet SSEs. To demonstrate the versatility of this coating technique, several Li-based binary alloys were tested and successfully coated onto various substrates. Similar behavior is observed with Na-based molten alloys and a Na-Sn alloy shows significantly improved wettability on an aluminum substrate. Therefore, this alloy-based soldering technique fundamentally solves the contact issue between Li metal anodes and garnet SSEs for solid state Li metal batteries. It also inspires new strategies to use Li or Na metals for battery applications, such as flexible Li or Na metal batteries and solid state Na metal batteries.

5.3 Results and discussion

Figure. 5-1 depicts the different wetting behaviors of pure lithium metal and lithium alloys on a solid substrate. The pure molten lithium dewets most solid substrates, such as ceramics, polymers, and even metals due to the large difference in surface energy (Figure. 5-1a). By adding other elements that can alloy with Li, the surface energy of molten Li can be tuned so that the molten alloys can wet well on the

aforementioned substrates. The Li alloys can be easily soldered onto the substrates in around 10 seconds and show much improved wettability (Figure. 5-1b).

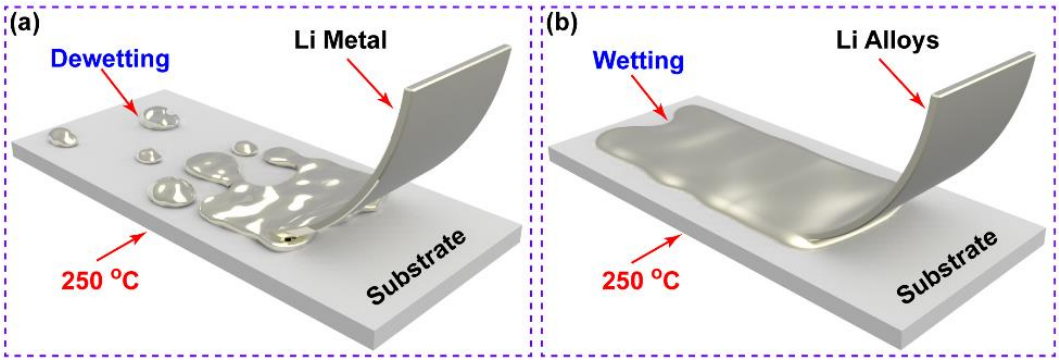

Figure 5-1. Schematic of soldering Li and Li alloy onto substrates (*e.g.*, ceramics, polymers, and metals). (a) Pure molten Li shows poor wetting behavior on the solid substrates. (b) Li alloys can be easily soldered on the substrates for much improved contact.

To demonstrate the effect of alloying elements on the wettability of molten Li, Li-Sn alloys with various weight ratios were prepared to test the wetting performance on alumina substrates (Figure. 5-2a). While both pure molten Li and Sn dewet on alumina substrates, their binary alloys show improved wettability as the ratio of tin increases. Above 10 wt% tin, the molten Li alloy starts to wet the substrate, but still has a large contact angle greater than 90°. When the ratio of tin is increased to 20 wt%, the molten alloy wets the substrate with a contact angle less than 90°. The Li-Sn alloys with 50 wt% or more of Sn can be smeared on the alumina substrates like paint with negligible contact angles. To demonstrate the application of Li alloys for solid state batteries, the Li-Sn alloy was coated on garnet-based SSE to improve the contact between the Li metal anode and garnet SSE. Unlike our previous methods, no surface

treatments are required to improve the wettability on the garnet pellets. In the demonstration (Figure. 5-2b), the polished garnet pellet can be quickly and uniformly wetted by the molten Li-Sn alloy (20-50 wt% Sn) within 10 seconds, much faster than all previous reports.[147–150] The SEM images (Figure. 5-2 c,d) also confirm the the excellent and uniform coating of the Li-Sn alloy on the garnet pellet. In the zoomed-in SEM image (Figure. 5-2d), the alloy shows a tight and conformal contact with the garnet SSE, which further demonstrates the effectiveness of the Li-Sn alloy soldering technique.

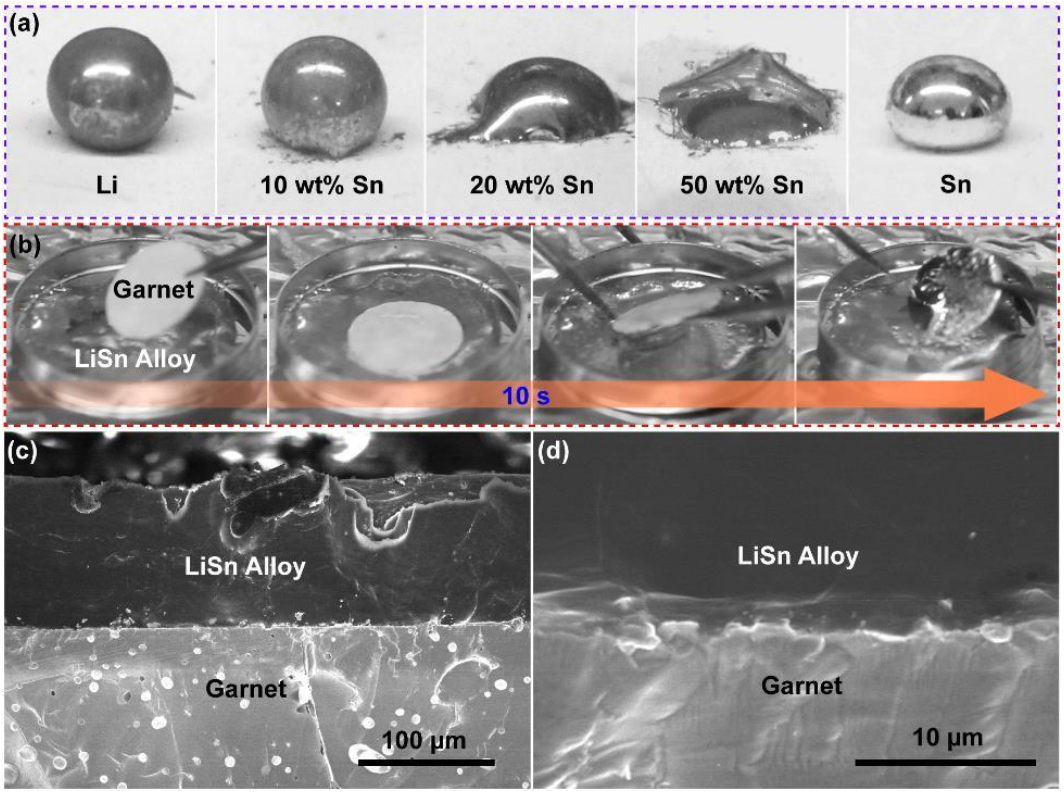

Figure 5-2. Wettability of Li-Sn alloys on ceramic substrates. (a) Wettability of molten Li-Sn alloys with different ratios of Sn on alumina substrates. The increasing content of Sn significantly improves the wettability of molten Li against alumina. (b) Images demonstrate the effectiveness of the Li-Sn alloy welding process on garnet SSE pellets.

In less than 10 seconds, the polished garnet pellet was successfully coated with uniform Li-Sn alloy. (c, d) Cross-sectional SEM images of the garnet pellet coated with Li-Sn alloy at different magnifications, which indicate a conformal interface between the alloy and garnet SSE.

The continuous and conformal contact between the Li alloy and garnet SSE also results in excellent electrochemical performance in solid state cells. To evaluate the interfacial properties of Li alloy and garnet SSE, Li-Sn/garnet/Li-Sn symmetric cells were fabricated to conduct electrochemical impedance spectroscopy (EIS) and symmetric DC stripping-plating measurements. Figure. 5-3a exhibits the results from EIS measurements of the symmetric cells made with the same garnet pellet coated with gold or lithium on both sides, respectively. The Au/garnet/Au symmetric cell was made by coating the polished garnet pellet with gold paste on both sides and then annealed at 800 ^{o}C for 30 minutes to ensure a good contact. Since the gold electrodes can block Li ion transport, the EIS measures the bulk resistance of the garnet pellet and has a long Warburg diffusion tail at low frequencies. The semicircle part of EIS is fitted to intercept with the real axis (inset of Figure. 5-3a) to estimate the bulk resistance of the garnet pellet. Then, the Au coated garnet pellet was carefully polished to remove the gold electrodes and quickly coat with the Li-Sn alloy (~ 30 wt% Sn) by following the aforementioned procedure to prepare a Li/garnet/Li symmetric cell. The EIS of the Li-Sn/garnet/Li-Sn symmetric cell does not have diffusion tail at low frequencies because of the presence of lithium metal on both sides. For this cell configuration, the overall resistance consists of bulk resistance due to the garnet pellet and the interfacial

resistance between the Li-Sn alloy and garnet pellet on both sides. Therefore, the difference in the real axis intercepts can be used to estimate the change in interfacial resistances between the Li-Sn alloy and Au coated garnet pellet. The interfacial resistance is calculated to about 7 $\Omega \cdot cm^2$, which is much smaller than most of the previously reported values.[143,145,147–150,156,157] Considering the efficiency and effectiveness of this technique, Li-Sn alloys offer an appealing solution to solder Li metal anodes on garnet SSEs for practical solid state batteries. Therefore, this technique is one of the most effective and feasible ways to solve the contact and interfacial resistance issues between Li metal anodes and garnet-based SSEs.

To further study the stability of the interface between the Li-Sn alloy and garnet pellet, Li-Sn/garnet/Li-Sn symmetric cells were tested by DC plating-stripping experiments. According to the EIS measurements shown in Figure. 5-3b and the corresponding voltage profile in Figure. 5-3c, the resistance of the symmetric cells remains constant while cycling for 100 hours. The voltage profile shows slight periodic variation about every 24 hours, which is attributed to the change in the ambient temperature conditions during the day and night. The insets of Figure. 5-3c show smooth and stable curves which indicates excellent stability of the soldered Li-Sn alloy and garnet pellet interface during electrochemical cycling. To further investigate the interface of the Li-Sn alloy and LLZO garnet, we also applied first principles calculations using the same approach as in our previous study.[149,150] For the four kinds of Li-Sn alloy we investigated: $Li_{17}Sn_4$, $Li_{13}Sn_5$, Li_7Sn_2, and LiSn; none of them exhibit reactions with the LLZO garnet. This further confirms that Li-Sn alloys indeed have good stability with garnet.

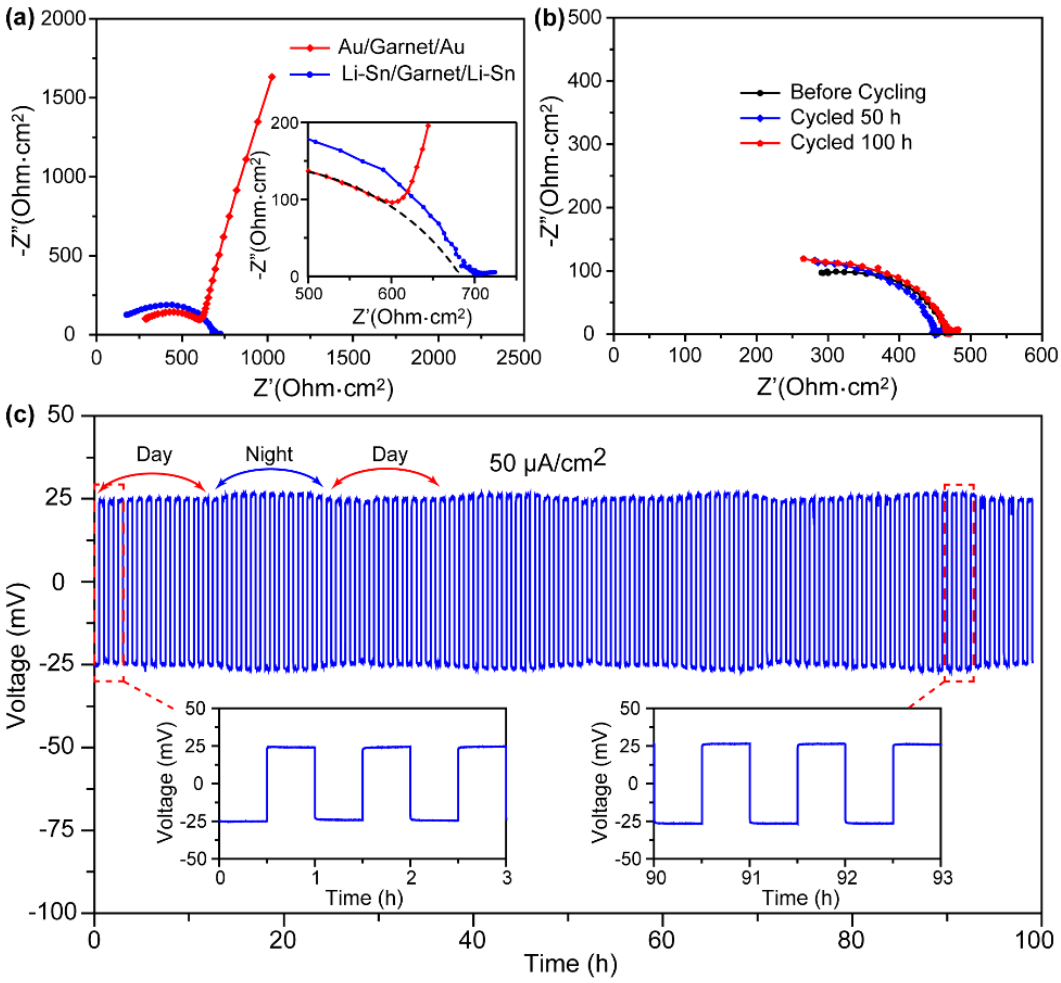

Figure 5-3. Electrochemical measurements of solid state symmetric cells. (a) EIS measurements of Au/garnet/Au and Li-Sn/garnet/Li-Sn symmetric cells for calculating interfacial resistance. (b) EIS measurements of the Li-Sn/garnet/Li-Sn symmetric cell before, during, and after Li plating-stripping at different times, which indicates a stable interfacial resistance. (c) Voltage profiles of the corresponding Li-Sn/garnet/Li-Sn symmetric cells during plating-stripping cycling at a current density of 50 μA/cm^2. The periodic variation is attributed to the temperature change during the day and night. The insets are zoomed-in snapshots of the profile at different times.

In the aforementioned study, the symmetric plating-stripping only involved a small amount of lithium transport. As the anode of lithium metal solid state battery for practical application, most of the lithium in Li-Sn alloy will be involved in battery cycling. Therefore, the stability of the Li-Sn alloy electrode during large capacity cycling needs to be studied further. For this case, a special symmetric cell was prepared to conduct the large capacity cycling. As Figure. 5-4a illustrates, to cycle under high capacity loads, one side of the symmetric cell is controlled to have a thin Li-Sn layer, while the other side is much thicker. While cycling, about 1 mAh/cm^2 of Li from the thick layer was continuously plated onto the thin layer. Initially, the thin layer is only about 2 μm thick, with continuous and tight contact to the garnet SSE (Figure. 5-4b). After cycling, the total thickness of the plated Li increases to about 10 μm and the electrode maintains good contact between the newly plated Li and garnet pellet (Figure. 5-4c). According to the energy-dispersive X-ray spectroscopy (EDS) mapping of the same area shown in Figure. 5-4d, the alloy element Sn is mainly on the top surface, indicating that the original Li-Sn alloy layer is lifted up by the newly plated Li. For the stripped side, the original Li-Sn alloy layer is about 100 μm thick and has the same continuous and tight contact as the other side (Figure. 5-4e).

After Li is stripped, the thickness of the Li-Sn alloy decreases to about 50-70 μm on the thicker electrode (Figure. 5-4f). Even after large amount of Li has been stripped from the electrode, the leftover Sn does not show any local accumulation at the interface in EDS mapping measurements as shown in Figure. 5-4g. Therefore, characterization of the interface and electrode morphologies after large capacity

platting-stripping further establishes the stability of the soldered Li-Sn alloy on garnet SSE during the battery cycling.

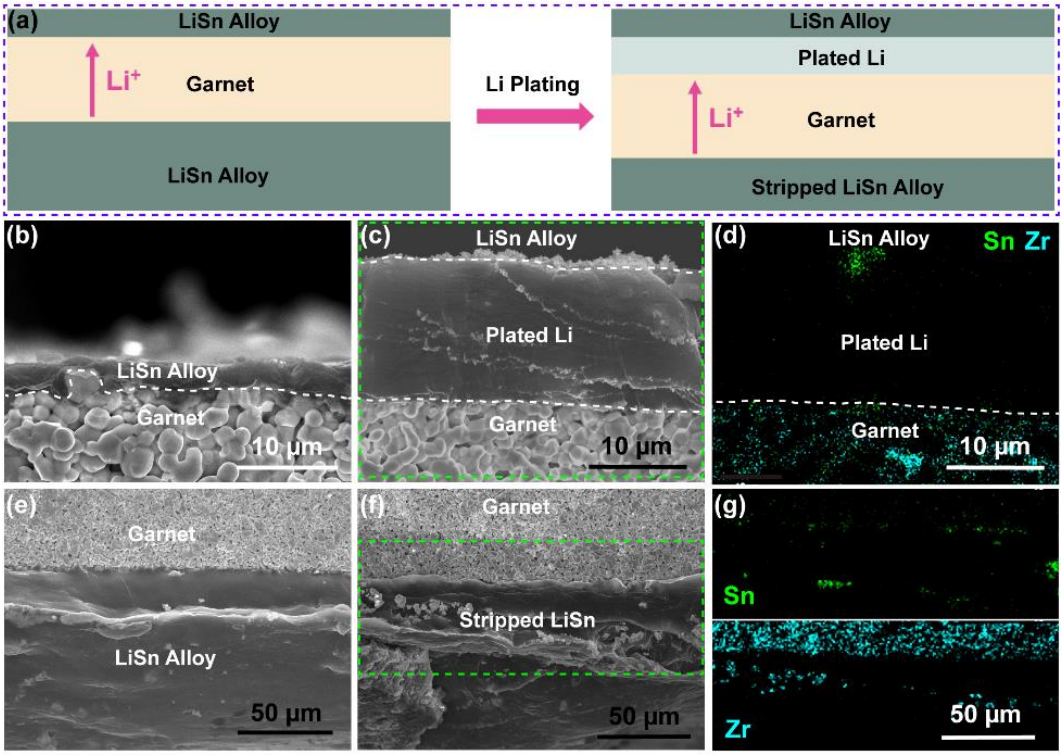

Figure 5-4. Characterization of the Li-Sn/garnet/Li-Sn symmetric cell morphology and interfaces during large capacity Li plating-stripping. (a) Schematic of the large capacity Li plating-stripping process for the Li/garnet/Li symmetric cell. Li is plated onto the thin Li-Sn alloy layer. Cross-sectional SEM images of the Li-Sn alloy coated garnet before (b) and after (c) Li plating. (d) EDS mapping of the Li plated area marked with a green dashed line in (c). The newly plated Li is between the original Li-Sn alloy layer and garnet pellet. Cross-sectional SEM images of the Li-Sn alloy coated garnet before (e) and after (f) Li stripping. (g) EDS mapping of the Li stripped area marked with a green dashed line in (f), where the leftover Sn does not show local accumulation at the interface.

To further demonstrate the versatility of this technique, we also studied this alloy based soldering technique using several different binary alloys and various substrates, including metals, polymers and ceramics. In this work, we tested four typical elements (Sn, Zn, Si, and Al) that can alloy with Li as well as a Na-Sn alloy on an alumina substrate. Figure. 5-5a exhibits the XRD patterns of several typical binary alloys that have been tested to have excellent wettability. The three Li-based alloys have peaks corresponding to the pure Li metal phase and binary alloy phases corresponding to the most stable compound in the phase diagram to balance an excessive stoichiometric ratio of Li metal (*i.e.* LiZn for Li-Zn alloy,[158] $Li_{22}Sn_5$ for Li-Sn alloy,[159] and $Li_{22}Si_5$ for Li-Si alloy[160]). Therefore, we can deduce that the addition of a binary alloy phase can significantly improve the wettability of molten Li metal. The soldering alloys are also observed to have higher viscosity than Li metal, which makes them much stickier in application to the various substrates. The changes in surface tension and viscosity agree with previous studies of alloys in the literature.[155] The XRD pattern of a Na-Sn alloy only shows the peaks of Na metal, which is attributed to the minimal amount of Sn in the alloy. Figure. 5-5b and e are digital images of titanium (Ti) foil wetted by molten Li and Li-Sn alloy, respectively. The molten Li can partially wet Ti foil, but shows a large contact angle (Figure. 5-5b). In contrast, the Li-Sn alloy coats well on the Ti foil and has a small contact angle (Figure. 5-5e).

Besides the typical ceramic and metal substrates, the Li-Sn alloy can also be soldered on some polymers. Figure. 5-5c and f depict Kapton film wetted by the molten Li and Li-Sn alloy, respectively. The Li-Sn alloy shows much better wettability than the Li metal and can be uniformly coated on the Kapton film. The alloy coated Kapton

film demonstrates excellent flexibility and outstanding mechanical strength, which is promising for flexible Li metal battery applications. Similar improvements to wettability can be achieved with Na-based molten alloys on alumina substrates (Figure. 5-5d, and g), which is particularly significant for solid state Na-β-alumina batteries. These results demonstrate the versatility of this alloy-based soldering technique for coating Li or Na metal onto various substrates for battery applications.

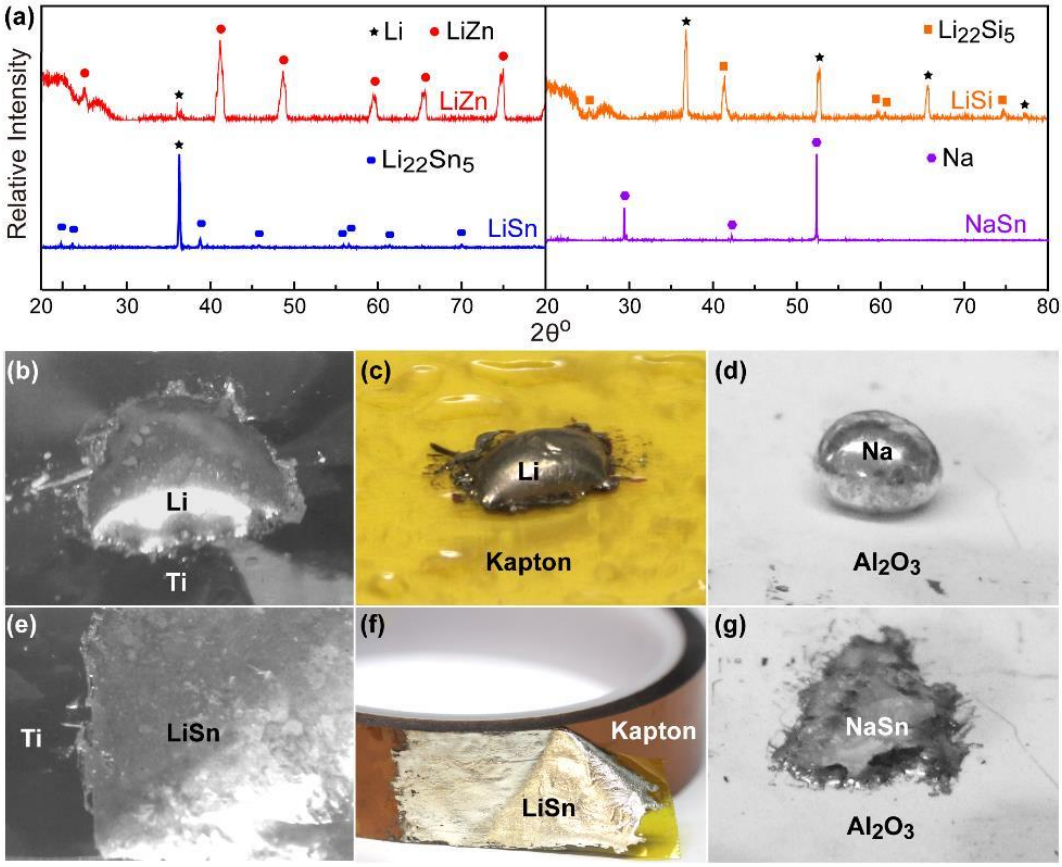

Figure 5-5. Alloy wetting on various substrates. (a) XRD patterns of binary alloys with good wettability. Photographs of molten Li wetted on (b) Ti foil and (c) Kapton film. (d) Photograph of molten Na on an alumina substrate. (e-f) Digital images of a molten Li-Sn alloy coated on Ti foil and Kapton film. (g) Photograph of molten Na-Sn alloy wetted alumina substrate.

5.4 Conclusion

By adding alloying elements to molten Li and Na, the surface energy and viscosity of negative electrodes can be manipulated to directly solder onto various substrates. As a demonstration, a Li-Sn alloy was soldered onto the surface of garnet SSEs within 10 seconds and exhibits a conformal and tight contact. The alloy significantly decreases the interfacial resistance against garnet SSE to as low as ~7 $\Omega \cdot cm^2$. Subsequent electrochemical studies confirm the excellent stability of both the interface and the alloy electrodes during the long time and high capacity cycling. To demonstrate the versatility of this alloy-based soldering technique, several other Li binary alloys were studied and display similar wetting behavior on metal, ceramic, and polymer substrates. Moreover, this direct soldering technique was extended to molten Na alloy systems, and in particular, a Na-Sn alloy was successfully coated on an alumina substrate. This direct soldering technique will inspire new strategies to develop safe Li and Na metal batteries with high energy densities.

5.5 Experimental

Synthesis of garnet solid-state electrolytes. Cubic garnet electrolyte of $Li_{6.75}La_{2.75}Ca_{0.25}Zr_{1.75}Nb_{0.25}O_{12}$ was synthesized by following a previous method.[148] Specifically, stoichiometric amounts of $LiOH \cdot H_2O$ (Alfa Aesar, 98.0%), La_2O_3 (Alfa Aesar, 99.9%), $CaCO_3$ (Alfa Aesar, 99.0 %), ZrO_2 (Inframat® Advanced Materials, 99.9%) and Nb_2O_5 (Alfa Aesar, 99.9%) were thoroughly ball milled in isopropanol for

24 h. To compensate for volatilization of lithium during the calcination and sintering processes, 10 wt% excess $LiOH \cdot H_2O$ was added. After the well-mixed precursors were dried, pressed and calcined at 900 °C for 10 h, the as-calcined pellets were broken down and ball-milled for 48 h in isopropanol. The dried powders were then pressed into 12.54 mm diameter pellets at 500 MPa, which were fully embedded in the mother powder and sintered at 1050 °C for 12 h. The alumina crucibles are used during the whole synthesis process. The as-made garnet pellets is about 1 cm in diameter, which were mechanically polished on both sides to about 500 μm thick to produce clean and flat surfaces for battery testing.

Direct soldering of Li or Na alloys and cell preparation. All the soldering and coating experiments were conducted on a hot plate at ~250^{o}C in an argon filled glovebox. To test the dependence of the alloy element ratio on the wettability, different weight percentages of alloy elements (Sn, Zn, Si, Al) were mixed with the molten Li and the alloys were smeared on substrates to show the wettability. All the binary alloys started to show an improved wettability when the weight percentage of the alloy elements exceeds 20 wt%. As the ratio of the alloying element increases, the viscosity and the wettability were observed to increase accordingly. To make Li-alloy/garnet/Li-alloy cells for electrochemical measurements, each side of the polished garnet pellets were directly placed and smeared with molten Li-Sn alloy (30-50 wt% of Sn) to ensure a conformal coating. Au/garnet/Au cells were prepared by coating gold paste on both sides of garnet pellets followed by annealing at 800 ^{o}C for 30 min. Titanium foil, Kapton film, and alumina substrates were first heated on the hot plate at about 250 ^{o}C, then the alloys were melt and smeared on the substrates to form a uniform coating. In

the control experiments, pure molten Li or Na metal was melted and coated onto the substrates following the same process.

Electrochemical measurement. Electrochemical tests of Li/garnet/Li symmetric cells were conducted on a BioLogic VMP3 potentiostat at room temperature. The electrochemical impedance spectra (EIS) were performed with a 20 mV AC amplitude in the frequency range of 100 mHz to 1 MHz for Li/garnet/Li cells and 100 Hz to 1 MHz for Au/garnet/Li cells, respectively. Galvanostatic stripping-plating of the Li/garnet/Li symmetric cells was recorded at room temperature with a current density of 50 $\mu A/cm^2$. The cells were placed in an argon filled glovebox to conduct all measurements.

Materials characterization. The morphologies and the elemental mapping of the Li alloy-garnet cross sections were conducted on a Tescan XEIA Plasma FIB/SEM at 10 kV. X-ray diffractions (XRD) of the binary alloys were performed on a C2 Discover diffractometer (Bruker AXS, WI, USA) using a Cu Kα radiation source operated at 40 kV and 40 mA.

Chapter 6: A General, Highly Efficient, High Temperature Thermal Pulse Toward High Performance Solid State Electrolyte*

6.1 Abstract

Surface contamination and degradation are two main issues leading to performance decay of ceramic-based solid-state electrolytes (SSEs). The typical strategies used to clean surface contaminants and restore ceramic materials involve mechanical polishing or high temperature thermal treatment. However, mechanical polishing can cause other side reactions and cannot clean contaminants on the grain boundaries of SSEs, while conventional thermal treatment using a furnace is often energy- and time-intensive, as the heating and cooling processes are slow. In this work, we for the first time demonstrate a high temperature thermal pulse technique for rapid ceramic surface processing. As a demonstration, we cleaned a garnet-based Li conductive SSE featuring lithium carbonate surface contamination in less than 2 seconds. The thermal pulsed garnet SSE exhibits an improved ionic conductivity of 3.2×10^{-4} S/cm—a two-fold increase compared to the starting material. Symmetric cells featuring the thermal pulsed garnet SSE can cycle at current densities up to 500 $\mu A/cm^2$, while control cells short-circuit at a current density of 100 $\mu A/cm^2$.

* The results in this chapter have been published: Wang, C.※; Xie, H. ※; Ping, W.; Dai, J.; Feng, G.; Yao, Y.; He, S.; Weaver, J.; Wang, H.; Gaskell, K.; et al. A General, Highly Efficient, High Temperature Thermal Pulse toward High-Performance Solid-State Electrolyte. *Energy Storage Mater.* **2019**, *17*, 234–241.

6.2 Introduction

Surface contamination and degradation are detrimental to the performance of ceramic materials, since many applications involve physical or chemical processes at the interfaces[161,162]. As lithium (Li) conductive ceramic materials, solid state electrolytes (SSEs) are especially plagued with these surface issues due to the high mobility and reactivity of Li ions[138,163,164]. SSEs have attracted great interest for replacing organic liquid electrolytes in Li-ion batteries due to their nonflammability, which makes it possible to use Li metal anodes without serious safety concerns[47,143,144,165]. Cubic garnet phase $Li_7La_3Zr_2O_{12}$ (LLZO) ceramic SSEs are among the most attractive candidates for achieving Li metal batteries due to the material's excellent chemical[136] and electrochemical stability against Li metal and its potential ability to block dendritic Li growth[119,130,133,140,166–169].

However, surface contamination or degradation of the ceramic leads to poor interfacial Li ion transport properties, which negatively affect electrochemical performance. Recent studies have shown that low ionic conductivity, poor electrolyte-electrode interfaces, and the secondary phase contaminations at grain boundaries of garnet can cause the short-circuit of garnet SSEs at high current densities[170–175]. Because of the high reactivity and mobility of Li ions, lithium carbonate (Li_2CO_3) contamination is one of the main reasons responsible for these problems. Particularly for aged garnet SSEs, Li_2CO_3 can easily accumulate on the surface or even at grain boundaries[176,177], making the storage of garnet SSEs a challenge in practical battery fabrication.

The conventional strategies to remove Li_2CO_3 and other surface contaminations involve mechanical polishing or high temperature thermal treatment to directly decompose the contaminations. However, mechanical polishing can cause other side reactions and cannot clean contaminants on the grain boundaries of SSEs, while conventional thermal treatment using typical thermal equipment (*i.e.*, a furnace) takes at least several hours to conduct the high temperature treatment, which is too long for practical battery manufacturing. Another issue associated with high temperature treatment of garnet SSEs is the Li loss that occurs due to the volatility of Li_2O at high temperature, which readily vaporizes at 600 ^oC[178] and can cause a phase change and poor ionic conductivity[166]. To simplify the thermal treatment and prevent Li loss, it is necessary to decrease the heating time while still maintaining the cleaning effect. Therefore, a fast and effective thermal treatment for garnet SSEs would be highly desirable for practical battery manufacturing.

In this work, we for the first time demonstrate a unique thermal pulse process that can successfully remove surface contamination from ceramics and restore aged garnet SSEs in less than 2 s. The maximum pulse temperature can reach up to 1250 ^oC (higher than the decomposition temperature of Li_2CO_3)[179] in 1 s, fully removing Li_2CO_3 contamination from both the surface and grain boundaries of garnet SSEs. The ultra-short pulse time also successfully prevents Li evaporation loss and the corresponding phase change problem. Because of the high treatment temperature and the inert gas atmosphere, an additional benefit of the thermal pulse process is the generation of oxygen vacancies in the garnet SSE, which recent studies have indicated play an important role in the electrochemical properties of the ceramic. Oxygen vacancies have

been demonstrated to affect Li ion transport and therefore the ionic conductivity of garnet SSEs[180,181], which can be a new strategy to further improve the electrochemical performance. The thermal pulsed garnet SSEs turn white and feature a 2-fold increase in the ionic conductivity, which we believe corresponds to the formation of oxygen vacancies. Benefiting from these effects, the thermal pulsed garnet SSE demonstrated improved electrochemical stability.

The schematic in Figure 6-1 demonstrates the rapid thermal pulse process and its effects on garnet SSEs. In this process, a grayish garnet pellet is placed on top of a carbon-felt heater in an argon-filled glove box. The carbon felt strip is rapidly powered through Joule heating, and the temperature of the garnet pellet increases up to 1250 ^{o}C, in which the slight evaporation of lithium oxide introduces oxygen vacancies. Since the temperature is much higher than the decomposition temperature of Li_2CO_3[179], and the carbon felt can also act as a reductant at high temperature[182], Li_2CO_3 on the garnet surface and grain boundaries can be thoroughly removed during the thermal pulse treatment. The cleaning effect is important in the real fabrication of garnet-based solid-state Li metal batteries, as the storage of garnet SSEs will inevitably result in the formation of Li_2CO_3 on the surface. The short treatment time ensures the Li loss due to evaporation is not significant, which is critical to maintain the phase and ionic conductivity of garnet SSEs. The unique rapid Joule heating method also enables the potential for a roll-to-roll process to clean garnet SSEs for real applications.

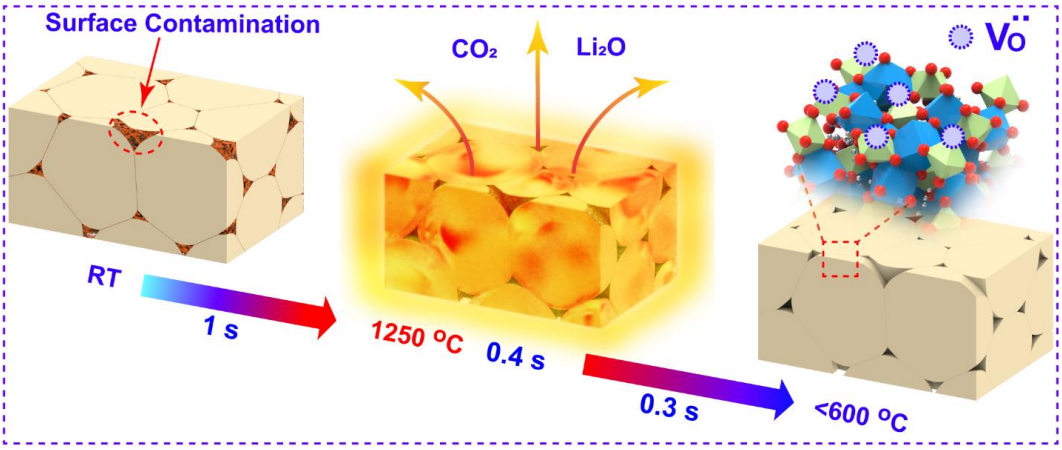

Figure 6-1. Schematic of the rapid thermal pulse treatment process of garnet SSE. During the treatment, Li_2CO_3 contamination is removed, simultaneously generating oxygen vacancies.

6.3 Results and discussion

Figure. 6-2a shows the thermal pulse treatment of the garnet SSE, in which we can clearly see that the pellet color changes from grayish to white. The cross-sectional image in Figure. 6-S1 demonstrates that this white color is not only on the surface but also in the bulk, indicating a whole pellet change after treatment. The images and the corresponding temperature profile indicate the garnet pellet was rapidly heated up from room temperature (RT) to 1250 ^{o}C in about 1 s, and this high temperature lasts for about 0.4 s. The subsequent natural cooling process only takes about 0.3 s, which makes the whole process less than 2 s long. Note that the temperature profile was acquired with a VIS-NIR spectrometer using a previous fitting method[183], which can be used to detect temperatures higher than ~600 ^{o}C. Due to the thermal capacity of the garnet pellets, the real temperature of the pellets may be slightly lower than the detected temperature of the carbon felt heating strip.

Cross-sectional scanning electron microscopy (SEM) images of the untreated and treated garnet pellets were used to characterize changes in morphology. Images of the near surface cross-section (Figure. 6-2b, c) show that the surface contamination was fully removed after the rapid thermal pulse treatment. Higher magnification SEM images of the interior grain boundaries further demonstrate the cleaning effect of the rapid thermal pulse treatment on the garnet SSE, in which the untreated garnet features rough contamination on the grain boundaries (Figure. 6-2d), while the same interfaces of the thermal pulse-treated garnet are much cleaner and smoother (Figure. 6-2e).

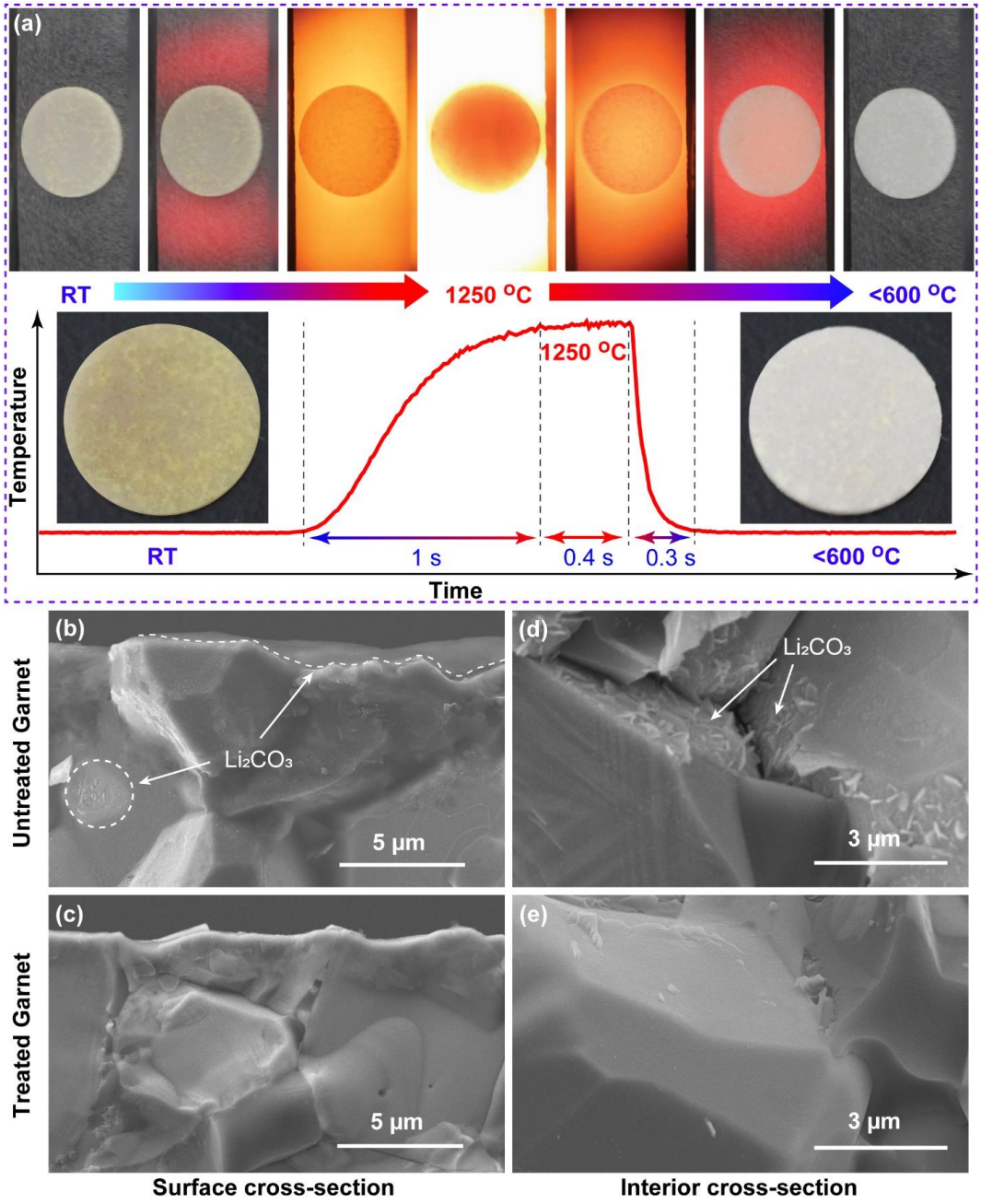

Figure 6-2. Rapid thermal pulse treatment of garnet pellets. (a) Images of the thermal pulse treatment process at different temperatures, and the temperature profile of the process. Cross-sectional SEM images near the surfaces of the garnet pellets (b) before and (c) after the thermal pulse treatment. (d, e) Cross-sectional SEM images of the

interior grain boundaries. The rough contamination of the untreated garnet (d) was removed after the thermal pulse treatment (e).

Besides the morphology change, we also studied potential crystal structural changes of the garnet SSE during the thermal pulse treatment. As previous works have reported[182,184], thermal treatment can remove Li_2CO_3 contamination from garnet. To demonstrate the effectiveness of Li_2CO_3 removal, we applied the rapid thermal pulse treatment to a garnet pellet aged for two weeks in air. Based on the SEM images in Figure. 6-S2, the grain size statistics of the treated and untreated garnet samples are shown in Figure. 6-3a, in which no obvious grain growth can be observed after treatment. X-ray diffraction (XRD) was used to characterize any phase change of the material (Figure. 6-3b). Small Li_2CO_3 peaks can be identified in the XRD pattern of the aged garnet, however, the peaks are absent in the pattern of the treated garnet, indicating the cleaning and restoring effect of the thermal pulse process. All the garnet peaks of both the untreated and thermal pulsed samples matched well with the standard cubic garnet phase (PDF#80-0457)[147]. The main difference is the relative intensity of each peak, especially the ones highlighted by the dashed-line box, which indicates a possible slight change in the lattice parameter. According to this XRD analysis, we can eliminate the possibility of a phase change from cubic to tetragonal due to excessive Li loss at high temperature.

Raman spectroscopy was also measured for the garnet SSE before and after the thermal pulse treatment. All the main bands corresponding to LLZO agree with the cubic garnet phase (Figure. 6-3c), which further confirms there was no phase change

after the thermal pulse treatment[185]. The Raman spectra also confirm the cleaning effect of the rapid thermal pulse treatment. The intense bands in the Raman spectrum at 158 cm^{-1} and 1091 cm^{-1} indicate a significant amount of Li_2CO_3 formation in the aged sample[185]. After rapid thermal pulse treatment, no obvious bands corresponding to Li_2CO_3 can be identified, which agrees with the morphology changes of the samples shown in Figure. 6-2 and the XRD analysis of Figure. 6-3b.

To characterize the lithium loss during the rapid thermal pulse treatment, neutron depth profiling (NDP) was used to quantitatively measure the lithium change[186,187]. Freshly-made garnet pellets were used to avoid the influence of Li_2CO_3, and the surface was dry-polished with 1200 grit SiC sandpaper[147] for both the untreated and thermal pulse-treated pellets just prior to NDP analysis. The Li depth distribution profiles of the untreated and the thermal pulse-treated garnet pellets are shown in Figure. 6-3d. The profiles are from the ^3H reaction products only. After integrating the counts over the whole energy range, the Li loss was calculated to be 1.59% ± 0.14% after treatment, much lower than that of other thermal treatments[166,182,188]. The quantitative NDP measurements indicate that Li loss during the rapid thermal pulse treatment is not significant within the bulk, which agrees with the XRD and Raman results.

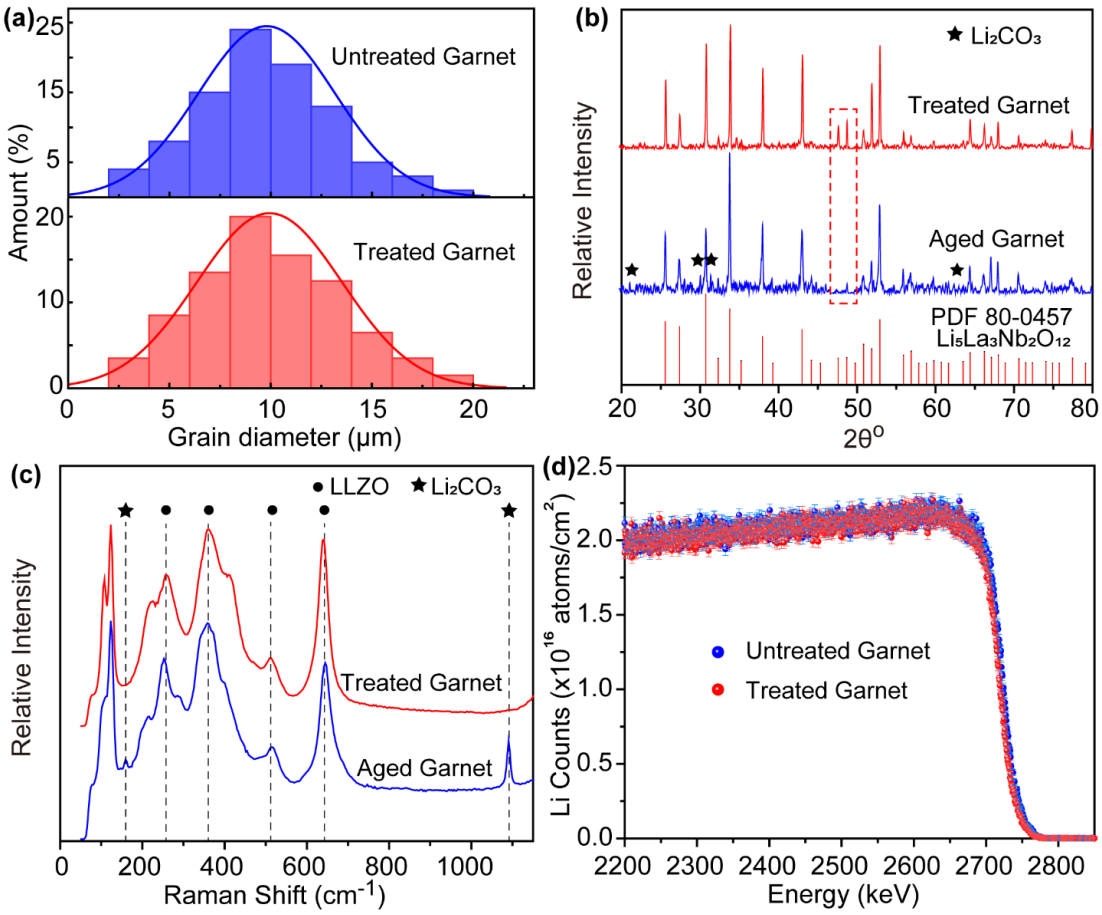

Figure 6-3. Characterization of the garnet SSE before and after thermal pulse treatment. (a) Grain size distribution of the untreated and thermal pulse treated garnet, indicating no grain size change. (b) XRD patterns and (c) Raman spectra of the garnet pellets before and after the thermal pulse treatment. (d) Li depth profile of the garnet pellets before and after the thermal pulse treatment, as measured *via* NDP analysis. The similar counts indicate that the Li loss to the bulk of the sample during thermal pulse treatment is negligible. Fractional error bars are calculated based on experimental counting statistics.

The color changes of the garnet pellets can be directly characterized by the UV-Vis absorption spectrum. On the UV-Vis spectra (Fig. 6-S3), the untreated garnet has higher absorption than the rapid thermal pulse-treated garnet, especially in the high wavelength range. The UV-Vis measurements indicate that the rapid thermal pulse-treatment increases the band gap of the garnet SSEs, which may potentially increase their chemical stability against Li metal[189]. This color change effect has been previously reported in several works. Goodenough and his coworkers thought the color change was due to the removal of Li_2CO_3 during thermal pulse treatment[182]. However, Doeff *et al*. have demonstrated that the sintering atmosphere can affect the color and the ionic conductivity of garnet pellets, and they proposed that the color change may be due to the formation of oxygen vacancies[190].

To understand the color change, we conducted X-ray photoelectron spectroscopy (XPS) analysis of the garnet pellets before and after the rapid thermal pulse treatment. Data was also collected after Ar ion sputtering to remove the post surface contamination for both the untreated and treated samples, designated as "untreated-S" and "treated-S," respectively. In the C 1s spectra (Figure. 6-4a), both the treated and untreated garnet SSEs before sputtering have peaks corresponding to Li_2CO_3 and hydrocarbon contaminations. After sputtering all the Li_2CO_3 and hydrocarbon have been removed from the treated-S sample, and most of it from the untreated-S sample, again showing that Li_2CO_3 is found in the form of an overlayer. The absence of the peak at ~290 eV corresponding to carbonate species for the thermal pulse-treated garnet further demonstrates the removal of Li_2CO_3 by the rapid thermal pulse treatment. The peaks in the O 1s spectra at 529 eV and 531eV correspond to the

O from garnet and Li_2CO_3, respectively (Figure. 6-4b)[182]. Before sputtering, the treated garnet displays a higher O^{2-} intensity at ~529 eV compared to the untreated sample, indicative of the larger attenuation of the carbonate overlayer after the thermal pulse. After sputtering, as seen by the absence of carbonate in the C 1s spectra (Figure. 6-4a), there should be no oxygen from carbonate in the O 1s spectra. However, there is still a peak at the higher binding energy (~531 eV) for the treated-S garnet sample. Since there is only one type of oxygen in the cubic LLZO crystal structure, it has been suggested that this peak could be due to oxygen vacancies[191], which is a common defect in garnet SSEs annealed in low oxygen atmospere[180,181]. Even though the intensities of the peaks at ~531 eV for treated-S and untreated-S in the O 1s spectra look equivalent on first glance, for the untreated-S sample there is actually still some carbonate remaining that is contributing to the signal. We calculated based on the C 1s peak that approximately 28% of the O 1s peak at ~531 eV for the untreated-S sample is due to carbonate. If the peak at ~531 eV is due to O vacancy, this would imply a larger number of vacancies in the thermal pulsed sample (treated-S) than the untreated garnet (untreated-S). Besides the difference in intensity, the peak at ~531 eV for the treated-S sample is slightly shifted to lower energy, which may also indicate the formation of O vacancies. In the Zr 3d and La $3d_{5/2}$ spectra, there were no obvious changes after the rapid thermal pulse treatment (Figure. 6-4c, d). Therefore, the two main possible reasons for the observed color change are the removal of Li_2CO_3 and the formation of oxygen vacancies.

To further exam these two explanations, a control experiment was conducted, in which the white thermal pulsed garnet pellets were re-annealed in pure oxygen

atmosphere at 800 ºC for 10 min. All the white pellets change back to a grayish color after this treatment. The result indicates that the color change during the rapid thermal pulse treatment is due to the formation of oxygen vacancies rather than the removal of Li_2CO_3, which is in agreement with previous reports that garnet SSEs annealed in argon are whiter than those annealed in air or oxygen[190]. Previous studies have shown that white garnet SSEs with more oxygen vacancies typically have better Li ionic conductivities[181,190]. However, the synthesis of garnet SSE in air is more practical and cost-effective, and the use of oxygen atmosphere can help densify the pellet during annealing[192]. Our rapid thermal pulse treatment can therefore take advantages of both processing conditions. Specifically, garnet SSE synthesized in air or oxygen can be rapidly treated in inert gas to introduce oxygen vacancies and improve the ionic conductivity.

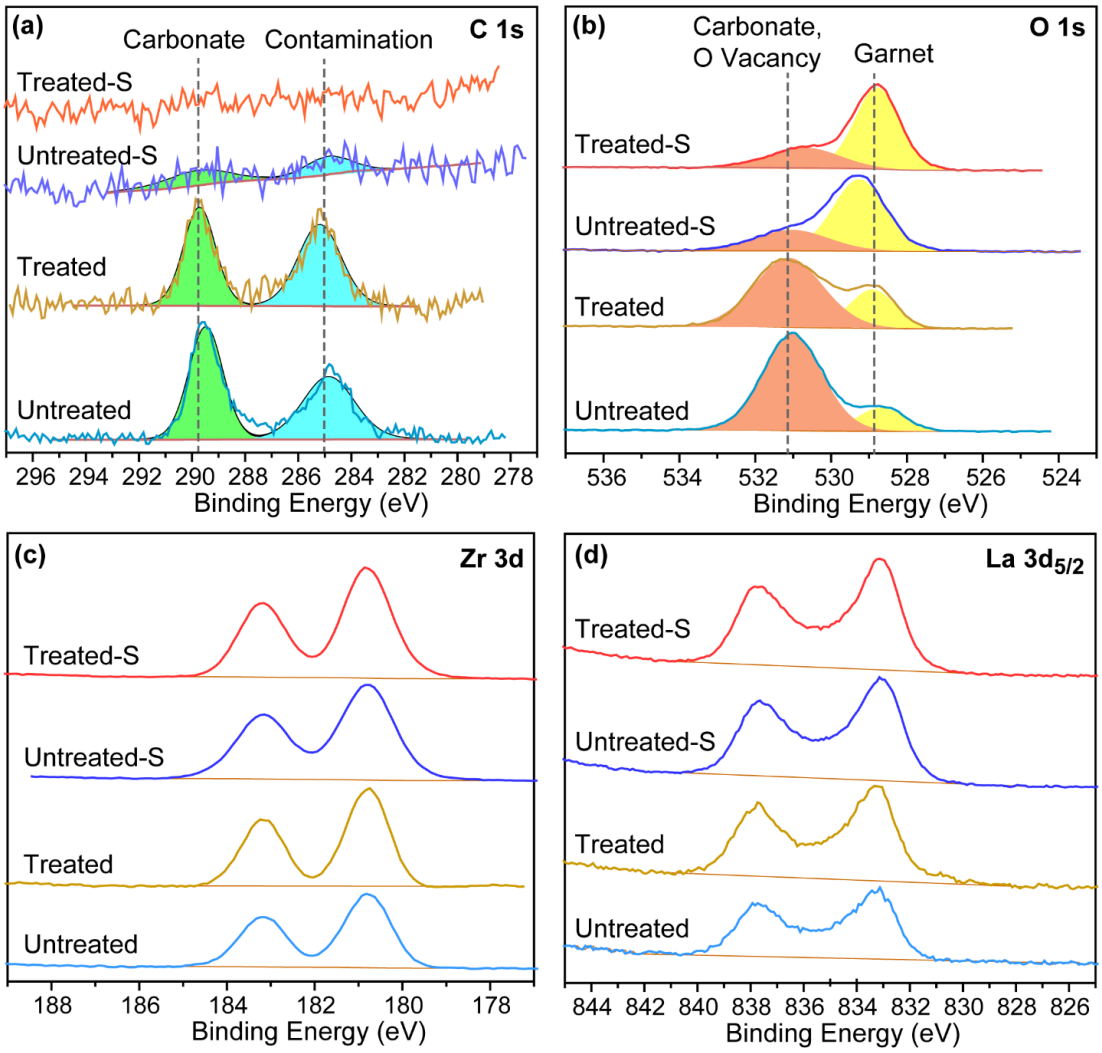

Figure 6-4. XPS measurement of garnet SSEs before (Untreated) and after (Treated) thermal pulse treatment, including (a) C 1s, (b) O 1s, (c) Zr 3d, and (d) La 3d spectra. The data was also collected after argon ion sputtering for both the untreated and treated samples, designated as "untreated-S" and "treated-S."

We studied the electrochemical properties of the rapid thermal pulse-treated garnet SSE by measuring the ionic conductivity and cycling performance of Li/SSE/Li symmetric cells. As electrochemical impedance spectroscopy (EIS) shows in Figure. 6-5a, the ionic conductivity of the thermal pulse-treated garnet (~3.2×10^{-4} S/cm) was

about twice that of the untreated material (~1.6×10^{-4} S/cm) due to the formation of oxygen vacancies, which is in agreement with the literature[180,190]. To further demonstrate the improved electrochemical properties of the thermal pulse-treated garnet, Li-Garnet-Li symmetric cells were assembled to conduct cycling at different current densities. The EIS spectra of the symmetric cells with the thermal pulse-treated garnet are shown in Figure. 6-5b, and the voltage profile of the cycling behavior is shown in Figure. 6-5c. The cell was cycled with elevated current densities from 100 μA/cm^2, and we observed the voltage profile was stable and smooth at current densities up to 300 μA/cm^2. At the end of the 300 μA/cm^2 cycling, the EIS was measured and shown in Figure. 6-5b, which only featured a slight increase from approximately 250 Ω·cm^2 to 280 Ω·cm^2, indicating excellent electrochemical stability. When the current density was further increased to 500 μA/cm^2, the voltage profile of the treated garnet starts to show polarization and becomes noisy at the fourth cycle (Figure. 6-5c). After 500 μA/cm^2, the EIS curve shown in Figure. 6-5b indicates a short-circuit, however, the current density achieved using the treated sample is comparable to the highest reported in the literature for garnet SSEs[184]. As a comparison, a control cell made with the untreated garnet was cycled at the same condition, and the cell died in the first cycle at a current density of 100 μA/cm^2 (Figure. 6-5c). Note that the starting garnet pellets used in this work only have moderate density and ionic conductivity. If we began with higher quality garnet, we expect the electrochemical performance of the treated material would be even further improved.

The improved electrochemical performance of the treated garnet can be attributed to the increased ionic conductivity and the removal of Li_2CO_3 during the

rapid thermal pulse treatment. Therefore, this treatment method can be used to quickly restore and boost the electrochemical properties of garnet SSEs during the practical fabrication of solid-state batteries. Compared with regular thermal treatment, the rapid thermal pulse has much shorter treatment time (Figure. 6-5d), which allows it to be integrated in roll-to-roll processes for potential scalable processing of ceramic materials. As the schematic in Figure. 6-5e shows, the untreated ceramic thin pellet with surface contamination and degradation can be quickly transported through two ultra-fast radiating heaters, in which the ceramic is thermally pulsed, producing a cleaner and more electrochemically stable material for battery application.

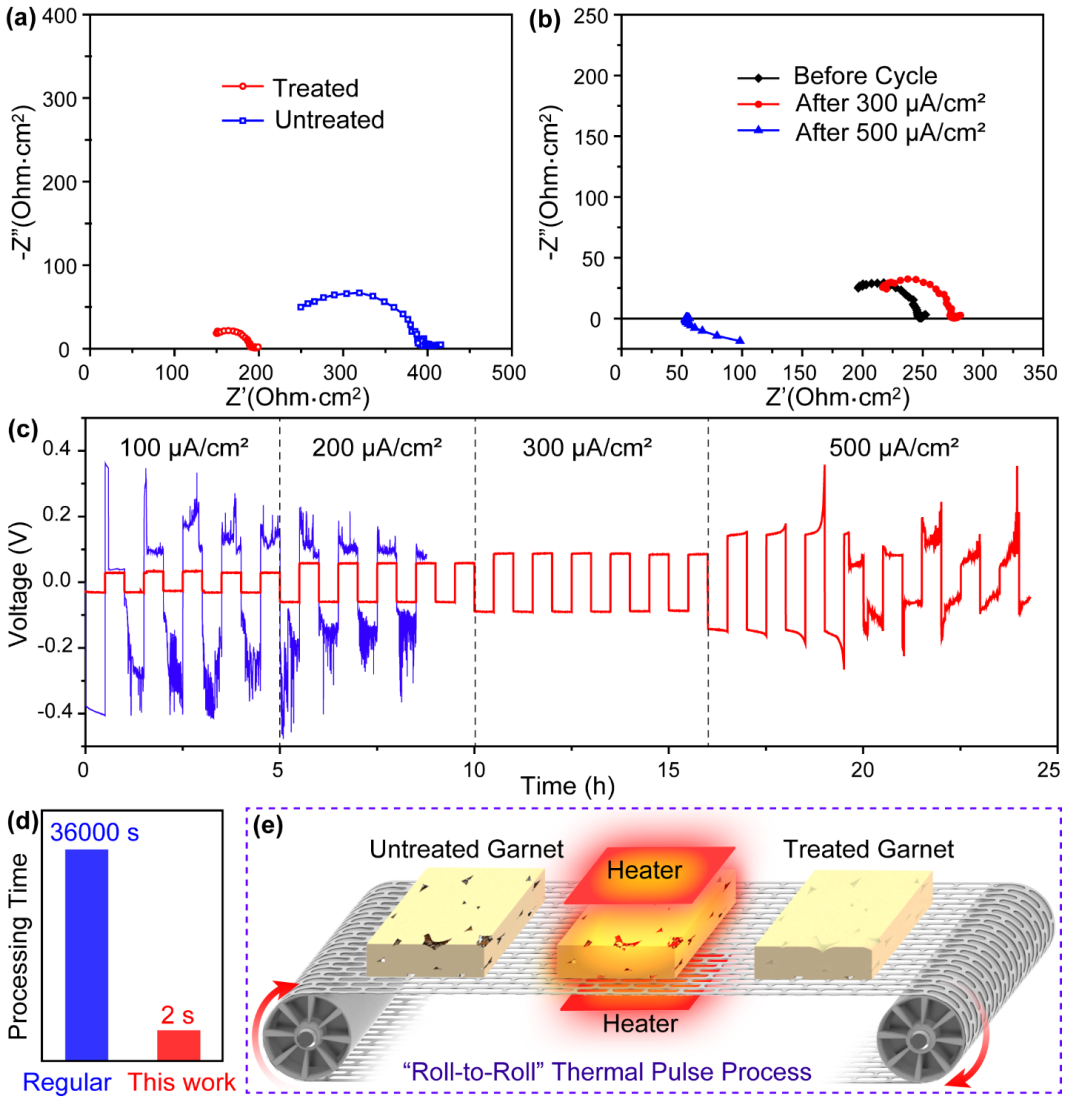

Figure 6-5. Electrochemical performance of the thermal pulse-treated garnet SSE. (a) EIS measurement of the garnet SSE before and after the thermal pulse treatment. (b) EIS measurement of the symmetric cells with the thermal pulse-treated garnet at different cycling stages. (c) Voltage profiles of the symmetric cells cycled at different current densities. The blue curve is the cell with the untreated garnet, and the red curve is the cell with the thermal pulse-treated garnet. (d) Processing time of thermal pulse and conventional thermal treatment techniques. (e) Schematic of the roll-to-roll process for rapid thermal treatment of ceramic materials.

6.4 Conclusion

For the first time, we have developed a thermal pulse technique for rapid ceramic surface processing that can quickly clean surface contamination and restore the materials in less than 2 s. As a demonstration, we successfully cleaned Li_2CO_3 contamination from the surface and grain boundaries of garnet SSEs. The ultra-short processing time prevented Li loss and any phase change of the garnet SSE at high temperature. We systematically studied the formation of oxygen vacancies by this process, which results in an increase in ionic conductivity of the garnet SSEs from about 1.6×10^{-4} S/cm to 3.2×10^{-4} S/cm. The rapid thermal pulse treatment also significantly improved the electrochemical stability of the material. Additionally, the critical cycling current density in symmetric cells increased from 100 $\mu A/cm^2$ to 500 $\mu A/cm^2$ after the thermal pulse treatment. This unique Joule heating method and ultra-fast process enable the potential for roll-to-roll processing for ceramic surface treatment in practical applications.

6.5 Experimental

Synthesis of the Garnet Solid-State Electrolyte. The Al-doped $Li_{6.75}La_3Zr_2O_{12}$ garnet electrolyte was synthesized via a solid-state reaction method. $LiOH\cdot H_2O$ (99.9%, Sigma Aldrich), La_2O_3 (≥ 99.9%, Sigma Aldrich), and ZrO_2 (99.9%, Sigma Aldrich) were used as precursors. Stoichiometric amounts were adequately mixed in isopropyl alcohol (IPA) for 12 h. 12% excess $LiOH\cdot H_2O$ was added to compensate for the loss of lithium during synthesis. Al_2O_3 nanopowder (~2 wt% of the total material) was

added to help the sintering process. The stoichiometrically mixed powders were calcined at 920 ºC for 12 h. Then the powders were mixed with IPA and ball-milled for 9 h. The powders were pressed into pellets with diameters of 10 mm at 300 MPa and sintered at 1150 ºC for 9 h. After the sintering process, the surface of the pellets was polished with 1200 grit sandpaper in an Ar-filled glovebox.

Thermal pulse treatment. Two tips of the carbon felt heating strip were attached to the edge of glass substrates using silver paste (SPI Supplies). Then a conductive copper tape was used to connect the heating strip with the power supply (VOLTEQ HY6020EX). The garnet pellets were directly placed on the heating strip. A Keithley 2400 power supply unit was used to generate signals that controlled a solid-state relay to control the power on and off. The thermal pulse process was recorded using a digital camera (Canon 60D, 30 frames s^{-1}). The temperature of the heater was calculated by fitting the radiation spectrum following a previous method[183], which was collected by a VIS-NIR spectrometer (USB2000+, Ocean Optics).

Electrochemical Measurement. A Li metal anode was coated on the garnet using a previous method[193]. Electrochemical tests of Li/garnet/Li symmetric cells were conducted on a BioLogic VMP3 potentiostat at room temperature. The EIS was performed with a 20 mV AC amplitude in the frequency range of 100 mHz to 1 MHz for Li/garnet/Li cells. Galvanostatic stripping-plating of the Li/garnet/Li symmetric cells were recorded at room temperature with various current densities. The cells were placed in an Ar-filled glovebox to conduct all measurements.

Materials Characterization. The morphologies and elemental mapping of the Li alloy-garnet cross sections were conducted on a Tescan XEIA Plasma focused ion

beam SEM at 10 kV. XRD spectra were measured on a C2 Discover diffractometer (Bruker AXS, WI, USA) using a Cu Kα radiation source operated at 40 kV and 40 mA. Raman characterization was done with a Horiba Jobin-Yvon equipped with a 532 nm laser and using an integration time of 4 seconds repeated for 4 measurements. The absorbance spectra were measured with a UV–Vis Spectrometer Lambda 35 (PerkInElmer, USA). XPS data was collected on a Kratos Axis 165 operating in hybrid mode using monochromatic Al Kalpha X-ray source (1486.7 eV). Charge neutralization was required to minimize sample charging. Survey spectra and high-resolution spectra were collected with pass energies of 160 eV and 40 eV, respectively. Data was collected both before and after argon ion sputtering. Sputtering was done at 4 kV and 25 ma emission current. The argon ion beam had a spot size of ~1 mm and was rastered to create a crater of 7 by 7 mm in size. The current measured at the sample holder when the beam was static (not rastered) was 2.5 μA. Samples were sputtered for 20 minutes. All the XPS spectra were calibrated to the lowest multiplet of the Zr $3d_{5/2}$ spin orbit split component at 180.8 eV. All samples were transported to the XPS instrument in an Ar environment, in which samples were polished in the glove box prior to transport to the XPS, and a glove bag was attached to the XPS instrument to minimize exposure to oxygen and water in an effort to prevent the formation of a thick Li_2CO_3 layer on the surface.

NDP data was collected at the Neutron Guide 5 (NG5), Cold Neutron Depth Profiling station at the NIST Center for Neutron Research (NCNR) at the National Institute of Standards and Technology (NIST, Gaithersburg, MD). The garnet pellets were dry polished with sand paper right before the measurement to reduce the effect of Li_2CO_3.

Samples were mounted with a 3.0 mm circular, Teflon® aperture. Each sample was irradiated at a near constant neutron fluence rate of cold neutrons (≈ 10^9 cm^{-2} s^{-1}), and all experiments were conducted under vacuum and at room temperature. NDP spectra were collected for ~10 h per sample. ^{6}Li nuclear reaction (^{6}Li(n,α)^{3}H) product triton particles (^{3}H) were detected using a circular transmission-type silicon surface-barrier detector that was positioned ~120 mm from the sample surface. Each spectrum was corrected for variations in the neutron fluence rate, detector dead time (≈ 0.01 %), and background noise. Li concentrations were calculated in reference to the known concentration of ^{10}B in a B-implanted concentration standard, according to the following equation. Fractional error was calculated based on experimental counting statistics.

$$[a] = [b]\frac{\sigma_{0,b}}{\sigma_{0,a}}$$

in which [a] and [b] are the concentrations (atoms/cm^2) of isotopes a and b being measured in the sample and standard, respectively, and σ_0 is the thermal neutron cross-section for the charged-particle emission. The slight difference in the position of the surface between the two samples is most likely due to the slight depletion of Li from the sample's surface during dry polishing.

6.6 Supporting information

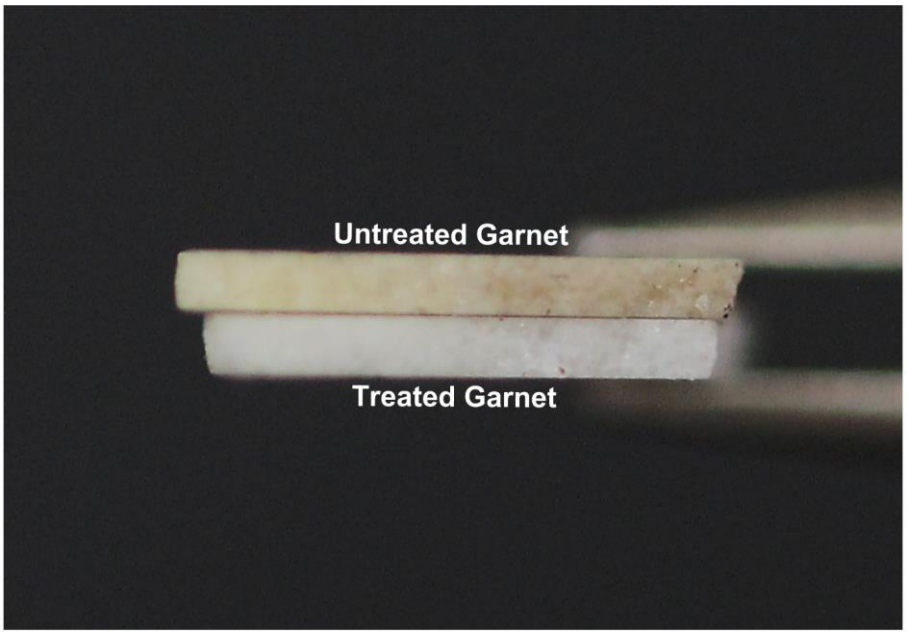

Figure 6-S1. Cross-sectional photograph of the untreated and thermal pulse-treated garnet pellets, indicating the color change occurs throughout the whole pellet.

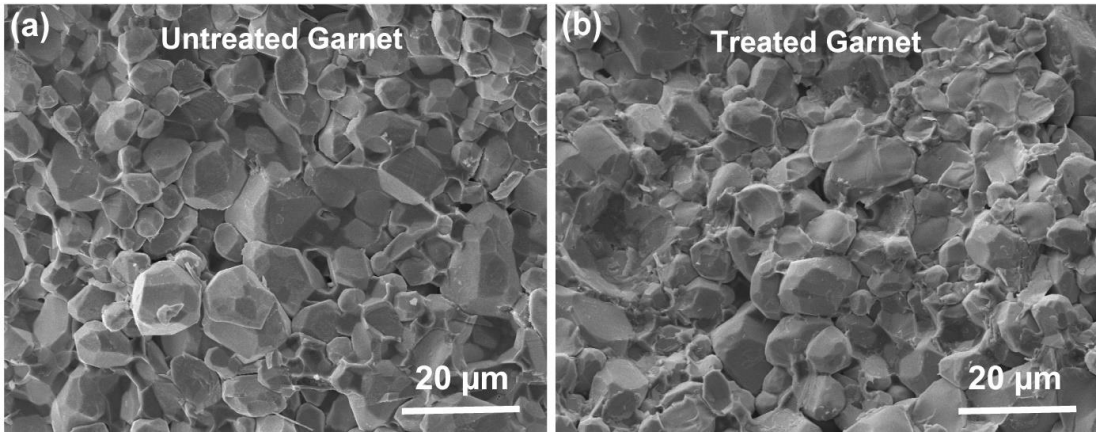

Figure 6-S2. Cross-sectional SEM images of the (a) untreated and (b) high-temperature treated garnet, indicating no obvious grain size change.

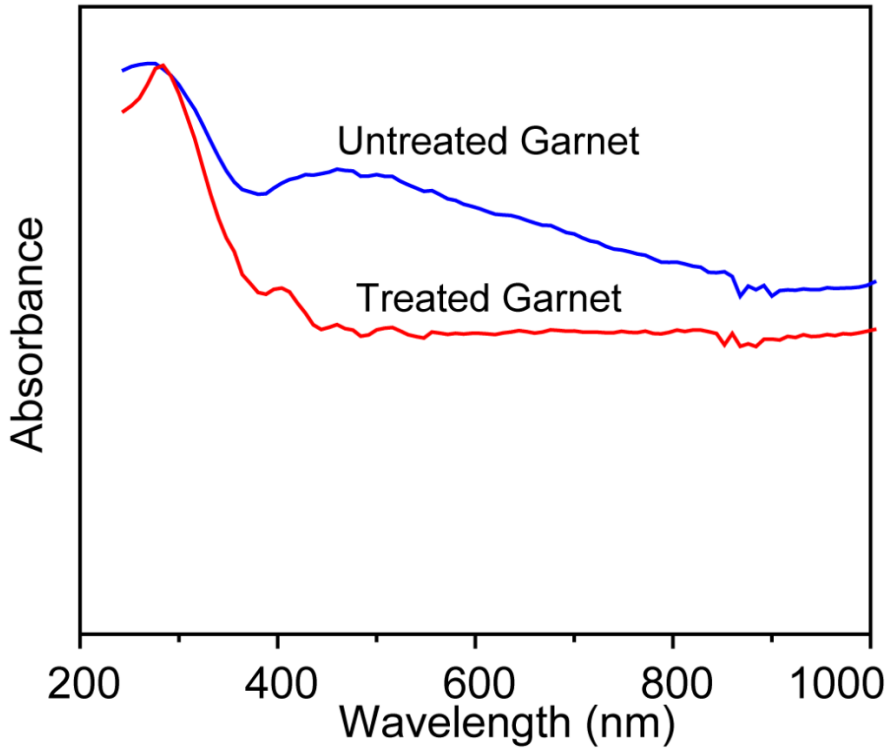

Figure 6-S3. UV-Vis absorbance spectra of the garnet pellets before and after the thermal pulse treatment. The untreated garnet has higher absorbance than the thermal pulse-treated material.

Chapter 7: Flexible, Scalable and Highly Conductive Garnet-Polymer Solid Electrolyte Templated by Bacterial Cellulose*

7.1 Abstract

Solid-state electrolyte is a promising candidate for the next-generation lithium-ion battery, as it has advantages of eliminating the leakage hazard of liquid solvent and elevating stability. However, inherent limitations such as the low ionic conductivity of solid polymer electrolytes and the high brittleness of inorganic ceramic electrolytes severally impede their practical application. Here, we report an inexpensive, facile and scalable strategy to fabricate a hybrid $Li_7La_3Zr_2O_{12}$ (LLZO) and poly(ethylene oxide)-based electrolyte by exploiting bacterial cellulose as a template. The well-organized LLZO network significantly enhances the ionic conductivity by extending long transport pathways for Li ions, exhibiting an elevated conductivity of 1.12×10^{-4} S $\cdot$ cm^{-1}. In addition, the hybrid electrolyte presents a structural flexibility, with minor impedance increase after bending. The facile and applicable approach establishes new principles for the strategy of designing scalable and flexible hybrid polymer electrolytes that can be utilized for high-energy-density batteries.

* The results in this chapter have been published: Xie, H.; Yang, C.; Fu, K. K.; Yao, Y.; Jiang, F.; Hitz, E. Flexible, Scalable , and Highly Conductive Garnet-Polymer Solid Electrolyte Templated by Bacterial Cellulose. *Adv. Energy Mater.* **2018**, *1703474*, 1–7.

7.2 Introduction

The future of electric vehicles, consumer electronics, and grid-scale renewable energy storage will place challenging demands on the performance requirements of portable energy storage[20–26]. While the lithium-ion (Li-ion) battery dominates the current battery market, improvement of the batteries in terms of cycle life, safety as well as system stability will be crucial to meet growing demands. However, traditional commercial electrolytes dissolved in organic solvents have the potential hazard of leakage and are extremely flammable, which can easily result in fire or explosion, causing more concerns about the safety issues of Li-ion batteries.[21] To address the safety issues and increase the durability, many strategies such as gel polymer electrolytes and all-solid-state electrolytes have been considered. Gel polymer electrolytes, which possess properties of both solid and liquid electrolytes, have been systematically scrutinized[27,29,30]. But their relative poor mechanical strength and high cost have limited further wide application. All-solid-state electrolytes are considered promising direction, two sorts of which are extensively studied: solid polymer electrolyte and inorganic solid electrolyte.[31–39] Polymer electrolytes, such as poly(ethylene oxide) (PEO) or polyacrylonitrile (PAN)-based matrices exhibit several advantages, including high flexibility and easy fabrication, using commonly available Li salts such as bis(trifluoromethane)sulfonimide lithium(LiTFSI) or $LiClO_4$ to impart sufficient ionic conductivity to the system.[40] However, solid polymer electrolytes usually present a relatively lower ionic conductivity compared to liquid electrolytes.[41] Although adding inorganic ceramic particles as fillers can increase their ionic conductivity, they still fall behind the requirements for commercial application.[42–44]

Compared with solid polymer electrolytes, inorganic solid electrolytes possess high ionic conductivity and have a high shear modulus to suppress the growth and penetration of Li dendrites. $Li_7La_3Zr_2O_{12}$, garnet-type Li solid-state electrolyte, has attracted much attention since it was first reported in 2007[45–48]. Despite its attractive ionic conductivity and excellent chemical and electrochemical stability, the brittleness and mass density of the ceramic ion conductor are too high to allow broad application of inorganic electrolytes.

One effective strategy to combat the limitations of both electrolyte types is to integrate both polymer and inorganic solid electrolytes into a single hybrid solid electrolyte[194–197] with the following advantages: (1) an enhanced ionic conductivity to reach the magnitude of 10^{-4} S/cm compared with controlled PEO-LiTFSI electrolyte; (2) improved electrochemical stability; (3) relative flexibility to bear the stresses resulting from cell fabrication and cycling; (4) reduced ceramic mass to increase the energy density per unit mass of the whole battery. However, experiments have proven that the simple combination of the solid polymer electrolyte and nano-size inorganic solid electrolyte does not always enhance the ionic conductivity of the electrolyte, owing to the agglomeration of the inorganic solid electrolyte.[127] Following a percolation mechanism, a long-distance Li-ion conductive pathway, which can be created by modifying the morphology of inorganic solid electrolyte inside the hybrid electrolyte, will allow the fast transport of Li ions in the pathway between the anode and cathode during charge and discharge cycles. Three-dimensional structures provide another possibility for combining inorganic and polymer solid electrolytes that is more efficient at achieving and maintaining conductivity than 2D or 1D structures.[198] To

achieve scalable 3D structures of sufficient feature dimensions and thus extend ion conduction paths, electrospinning is an attractive method capable of generating continuous inorganic solid electrolyte fibers. But there is still a need to find a strategy to decrease the cost of manufacture and to expand to large-scale fabrication.

Cellulose is one of the most copious natural polymer materials in the world, and bacterial cellulose, produced by cultivating *Acetobacter* with carbon and nitrogen sources, possesses very attractive properties, such as extremely fine and pure fiber network, high water absorption capacity, high mechanical strength and good physico-chemical stability[199–202]. These advantages make this low-cost natural polymer material a promising candidate as a template for engineering novel materials with similar porous morphology.[203–207]

Here, we designed a facile, low-cost, and large-scalable strategy to use bacteria cellulose (BC) as a template to synthesize a hybrid electrolyte membrane with a c-LLZO interconnected network and PEO polymer with LiTFSI. BC, produced by bacteria in the genus *Acetobacter*, possesses highly networked nanofibrils and presents a distinguished water absorption capacity.[200] Owing to its porous microstructure and high water-absorption capacity, bacterial cellulose can be exploited to absorb the relevant precursor salt solution to produce porous cubic-phase garnet-type LLZO nanofiber network after calcination. PEO-LiTFSI electrolyte was infiltrated into the LLZO nanofiber network to improve its flexibility and form a hybrid electrolyte. In this hybrid electrolyte, both the BC-templated c-LLZO and the conformal interface between PEO and LLZO offer interconnected channels for Li ions to move for long distances without obstacles. Because of these fast ion transport pathways and the high

aspect ratio of the LLZO network, the hybrid electrolyte is expected to have a high ionic conductivity comparable to that of a bulk LLZO disk. The addition of PEO Li-TFSI polymer not only acts as a cushion surrounding the LLZO to absorb the exerted external stresses and protect the fiber network from breaking into pieces, but it also works as a binder to connect the electrode and electrolyte, significantly reducing the interface issues and suppressing uneven Li deposition during cycling. This inexpensive but efficient strategy can also be applied to synthesize similar types of hybrid electrolyte in other electrochemical energy storage systems.

7.3 Results and discussion

Figure 7-1 illustrates the schematic strategy for the synthesis of LLZO/PEO-LiTFSI hybrid electrolyte. A BC aerogel membrane was exploited as a scalable and hydrophilic template for soaking in an LLZO precursor solution. After a calcination treatment, BC fibers can be completely removed and the c-LLZO membrane was fabricated. A polymer-ceramic hybrid electrolyte was successfully synthesized by mixing the PEO-LiTFSI polymer and c-LLZO membrane (for details, see the experimental method part). The fast Li-ion transport pathways are also schematically displayed in Figure 7-1, in which the c-LLZO network offer a fast Li-ion conductive route. Several mechanisms give rise to the significantly enhanced ionic conductivity of the hybrid electrolyte. The inorganic LLZO ceramic itself exhibits excellent bulk ionic conductivity, which can reach about $10^{-3}\,\mathrm{S\cdot cm^{-1}}$ at room temperature through doping various elements[208–210]. The continuous ion conducting network offers fast Li-ion conductive pathways inside the fibers and acts as a scaffold to offer mechanical

support for the solid polymer electrolyte. It is also reported that the interface interaction between the polymer and the inorganic ceramic can effectively increase the ion transport ability along the fiber surface.[211–216] The 3D interconnected fiber network and the conformal structure of the PEO polymer to the LLZO fibers contribute to the high flexibility of the hybrid electrolyte. The 3D fiber network's large length-to-diameter ratio and its intertwined structure facilitate the absorption of local strain energy and tailor the redistribution of stress by reducing the stress concentration at localized points. A PEO polymer coating on the LLZO fibers acts as the protection layer, enhancing the mechanical resilience of the structure. In addition, compared to the conventional liquid electrolyte, this hybrid electrolyte can not only reduce the safety concerns about the flammability of liquid solvent, but it can also substitute the separator to isolate anode and cathode during the operation of a battery. This facile and large-scalable method is also applicable to the fabrication of other types of hybrid electrolytes as well.

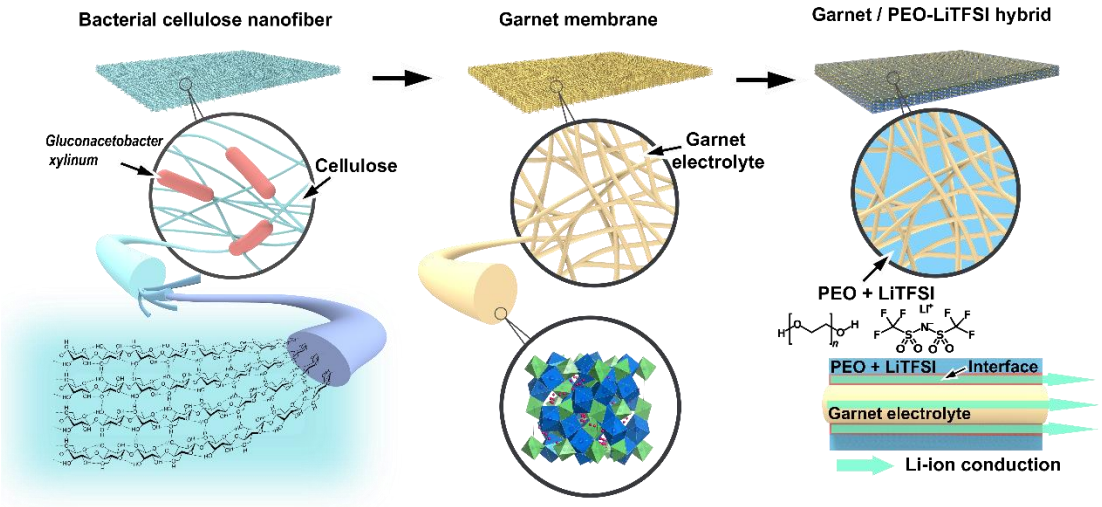

Figure 7-1. Schematic demonstrating the procedure for the synthesis of the hybrid electrolyte with BC as an inexpensive, scalable, and efficient template. The microstructures for Li-ion transport are also schematically illustrated.

Purified BC nanofibers typically present a white gel-like morphology, as is shown in Figure 7-2a, which can be acquired in large scale owing to its abundance. SEM images (Figure 7-2b) show that long, interconnected cellulose fibers assemble into larger BC fibrils, which are randomly distributed in a 3D porous network to form the overall membrane. A higher magnification image in Figure 7-2c indicates that the diameter of the interconnected cellulose fibers is around 30 to 100 nm, twisting at the connection nodes. Each fiber is composed of subordinate structures of elementary fibrils with numerous hydroxyl groups whose hydrophilic properties and 3D porous structure provide an excellent advantage when soak up the liquid precursor solution.

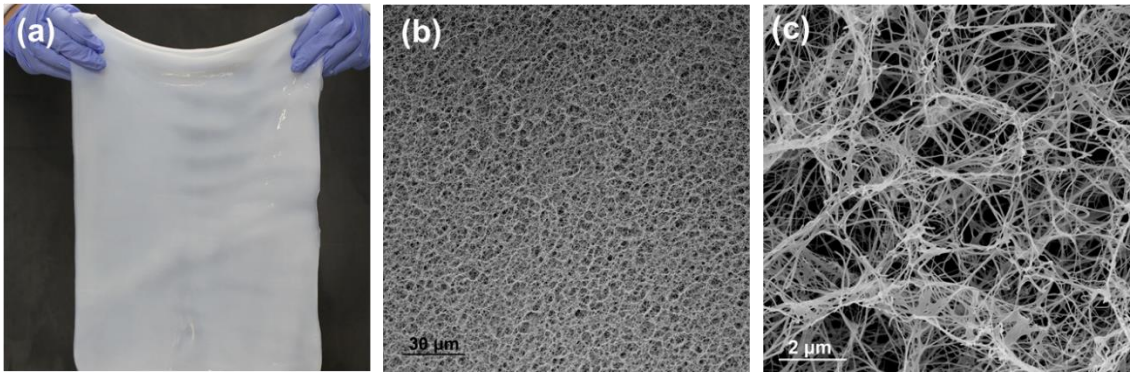

Figure 7-2. Fabrication of c-LLZO porous network with BC nanofiber as the template. (A) Digital photo of a large-scale BC membrane. (B) SEM image of the well-organized and interconnected 3D network structure of the BC aerogel membrane after freeze-drying treatment, which provides a high water absorption capacity. (C) Zoomed-in

SEM image of the cellulose fibrils, with a diameter under 100 nm to facilitate precursor solution absorption.

Thermal calcination is required to achieve the c-LLZO phase from the precursor and to remove the BC template. Figure 7-3a and b depict the microstructure and morphology of the as-calcined porous LLZO inorganic electrolyte membrane. Compared to the topography of original BC nanofibers, the ceramic membrane after sintering can maintain the well-organized, interconnected, and 3D porous structure. The apparent pore dimension in the ceramic membrane is increased compared to that of the porous BC nanofibers. However, the quintessence of the microstructure, namely the 3D interconnected network crucial for fast Li-ion transport, is well maintained after the BC fibrils are decomposed at high temperature. A high magnification SEM image (Figure 7-3b) depicts that the ceramic fibers have a width of 500 nm to 1 μm, which is a sufficiently high aspect ratio to realize structural flexibility.

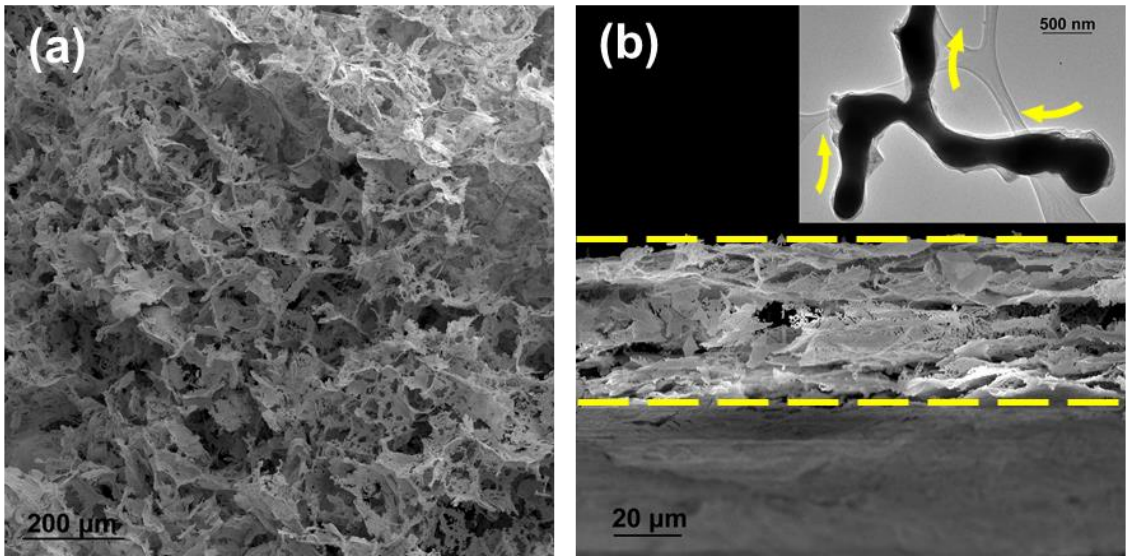

Figure 7-3. (a) SEM image of the LLZO membrane after calcination at 850 ℃, the 3D interconnected porous structure of which is critical to offer fast Li-ion transport pathways and to increase the concentration of free Li ions. (b) SEM image showing a cross-section view of the LLZO nanofiber network. Inset is the transmission electron microscopy (TEM) image of single LLZO fiber.

Figure 7-4 presents the X-ray diffraction (XRD) pattern of the as-calcined LLZO membrane, which indicates a good fit with data of the cubic garnet-type structure belonging to the $Ia\bar{3}d$ space group. In the cubic LLZO (c-LLZO) structure, Zr atoms are situated at the center of an octahedral site with six coordinated oxygen atoms around and La atoms are situated at the center of a dodecahedral site with eight coordinated oxygen atoms around. Owing to the existence of Li vacancies, Li ions can migrate or hop in the garnet vacancy network, exhibiting a three-dimensional conduction mechanism with a high ionic conductivity. It should be noted that the cubic garnet phase can be effectively stabilized at room temperature through doping with aluminum, as the conductivity of cubic-phase LLZO is 2 orders of magnitude higher than that of tetragonal LLZO.[217,218] In addition, compared to bulk LLZO sintering, which usually takes place at a temperature higher than 900 ℃, the 3D interconnected porous microstructure facilitates the formation of c-LLZO after calcination at a lower sintering temperature (850 ℃).

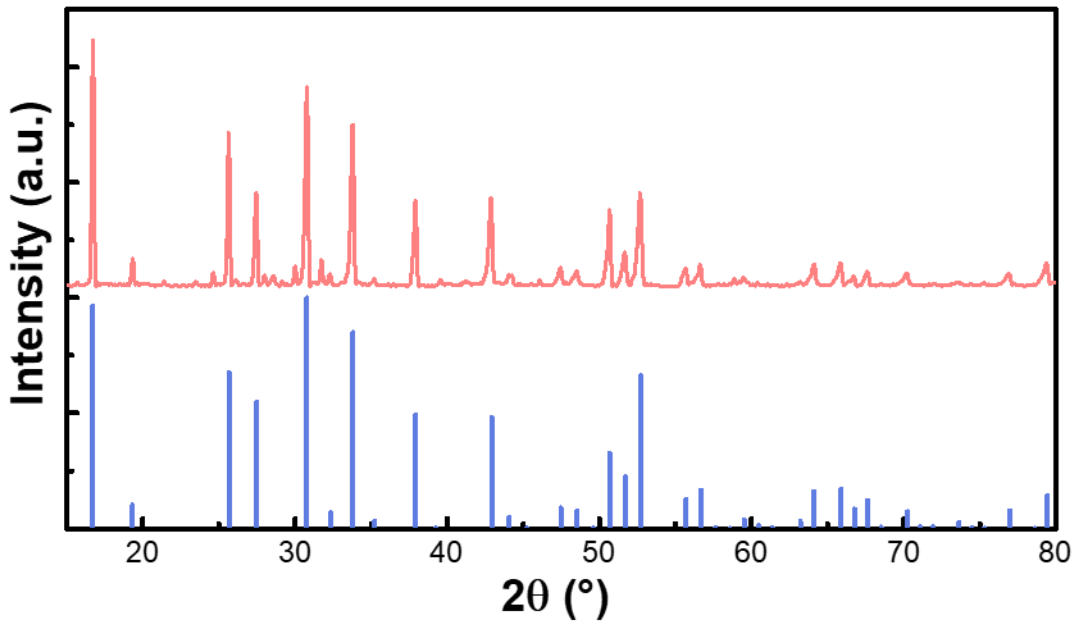

Figure 7-4. The XRD pattern of the as-achieved LLZO fiber network. The peaks correspond to cubic garnet type with space group $Ia\bar{3}d$ (PDF 01-080-4947), which presents a higher ionic conductivity compared with the tetragonal phase LLZO.

After calcination, PEO-LiTFSI electrolyte was infiltrated into the nanoporous c-LLZO membrane to obtain the hybrid electrolyte. Figure 7-5a and b depict the top surface morphology of the hybrid electrolyte, in which the LLZO ceramic membrane is covered by the polymer electrolyte. Because of the high viscosity of PEO after the volatilization of acetonitrile solvent, the polymer electrolyte and LLZO fibers can form very conformal microstructures, which effectively address interfacial concerns between the two types of electrolytes. It should be noted that this rugged morphology can further reduce the interfacial impedance between the hybrid electrolyte itself and electrodes due to the high viscosity of the polymer and improvement of their interfacial

contact. Figure 7-5c shows the cross section of the hybrid electrolyte. The thickness of the hybrid electrolyte is around 70–100 μm, much thinner than the usual bulk LLZO electrolytes (200 μm to 400 μm), in favor of small electrolyte resistance.[147] The hybrid electrolyte with a mixture of polymer and LLZO fibers significantly decreases the mass used in the electrolyte, which is further beneficial to the energy density per unit mass of the whole battery. Moreover, after the assembly of the electrolytes, the hybrid electrolyte presents a structural flexibility and can withstand bending (shown in Figure 7-5d), effectively addressing the fragility of inorganic electrolytes during mass manufacture. This flexibility is highly correlated with the 3D interconnected fiber network and the conformal structure, as the LLZO fibers are imbedded in the PEO polymer. Compared with bulk ceramics, the 3D fiber network possesses a large length-to-diameter ratio and intertwined structure, which facilitates the absorption of local strain energy and tailors the redistribution of stress by reducing the stress concentration positions.

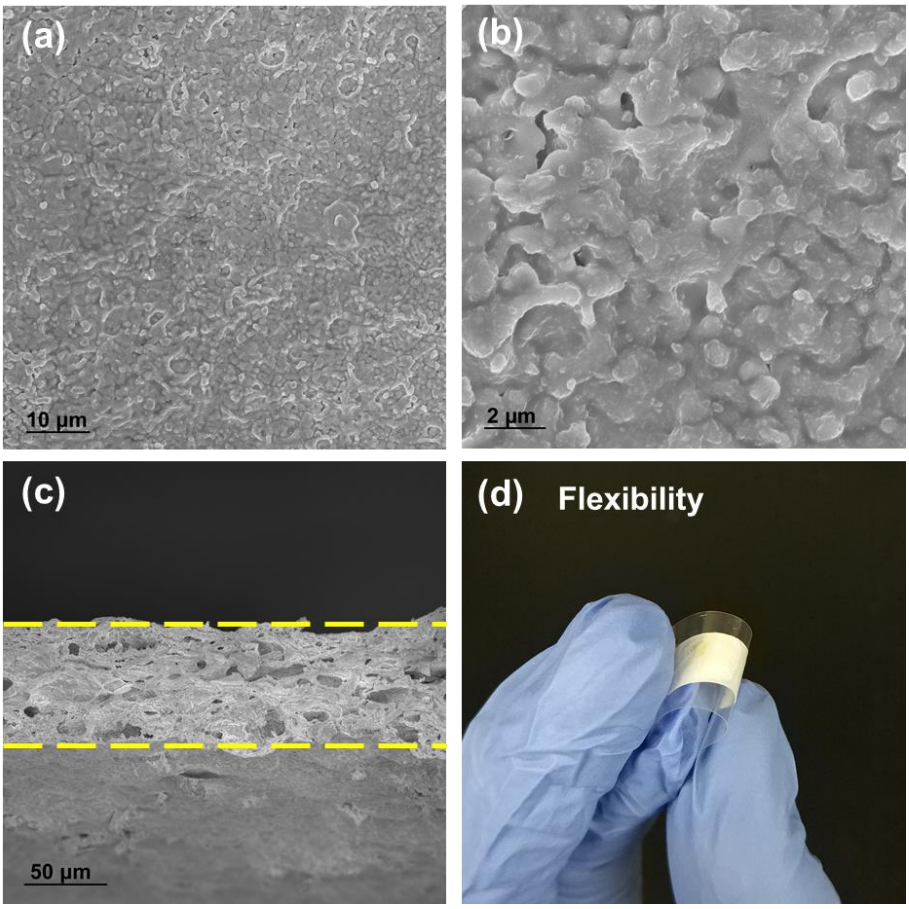

Figure 7-5. The morphology and flexibility of the hybrid electrolyte. (A) SEM image of the top surface of the hybrid electrolyte. The surface displays a rugged morphology. (B) Zoomed-in SEM image of the top surface of the hybrid electrolyte, presenting a conformal structure of ceramic fibers coated with PEO polymer. (C) Cross-sectional SEM image of the hybrid electrolyte with a thickness ranging from 70 μm to 100 μm, which also acts as a separator to isolate the electrodes. (D) Photo showing the flexibility of the hybrid electrolyte, which is associated with the fiber network and conformal structure between ceramic fibers and a polymer electrolyte.

Figure 7-6 shows the Fourier-transform infrared spectroscopy (FTIR) of hybrid electrolyte. Owing to the introduction of LLZO, the absorption peaks of PEO-LiTFSI around 870, 1425 and 1475 cm^{-1} are significantly enhanced, indicating that the two-component electrolytes have a synergistic effect, contributing to the high ionic conductive performance.

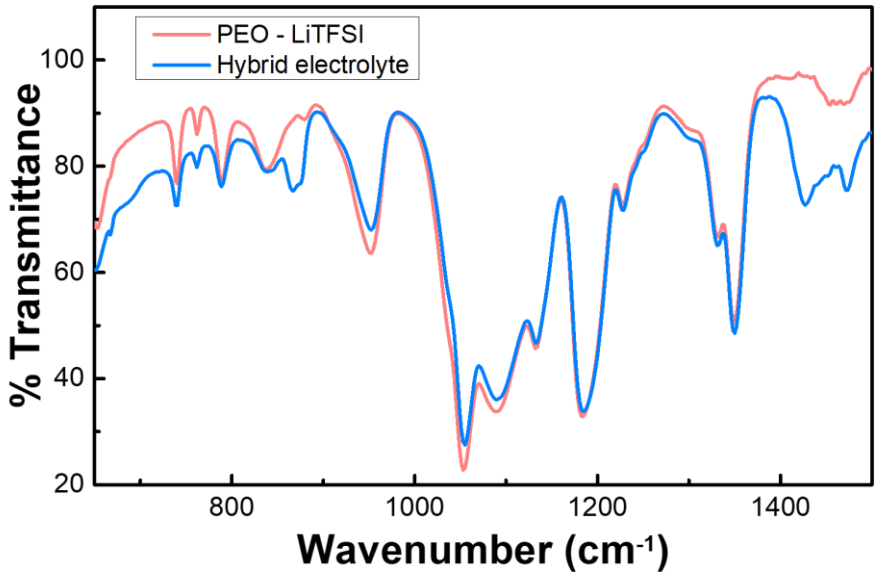

Figure 7-6 FTIR of the hybrid electrolyte, in which PEO-LiTFSI and LLZO present enhanced peaks around 870, 1425 and 1475 cm^{-1}.

Electrochemical impedance spectrum (EIS) was employed to measure the ionic conductivity of the hybrid electrolyte (Figure 7-7a) and the ionic conductivity for hybrid electrolyte at room temperature is $1.12 \times 10^{-4}\ S \cdot cm^{-1}$. As the temperature increases from room temperature, the ionic conductivity of the hybrid electrolyte also increases. Figure 7-7b depicts the relationship between ionic conductivity of the electrolyte and temperature for both the hybrid electrolyte and PEO-LiTFSI electrolyte.

Compared to the PEO-LiTFSI, the hybrid electrolyte presents a significant improvement of the ionic conductivity, much higher than that of controlled PEO-LiTFSI electrolyte (about $1 \times 10^{-6}\,S \cdot cm^{-1}$). Understanding the mechanisms that govern the impressive increase in the ionic conductivity can offer the guidance for the design of novel hybrid electrolytes. BC-templated LLZO ceramic membrane has played a significant role in the improvement of conductivity. The interconnected network functions as a single entity and effectively eliminates the degradation of ionic conductivity owing to the agglomeration of ceramic nanofibers, enhancing the transport along the fibers with less obstacles. In addition, the high aspect ratio of the ceramic network offers more interfacial areas between LLZO ceramic and PEO polymer, and the transport of Li ions in both PEO polymer and LLZO ceramic contributes to the impedance decrease of the hybrid electrolyte , augmenting the ionic conductivity. Figure 7-7c illustrates the linear sweep voltammetry (LSV) profile for the hybrid electrolyte. Compared to PEO-LiTFSI electrolyte, the hybrid electrolyte exhibits a very stable voltage window up to 6.0 V vs. Li^+/Li, revealing suitability of this hybrid for high-voltage Li-ion battery applications.

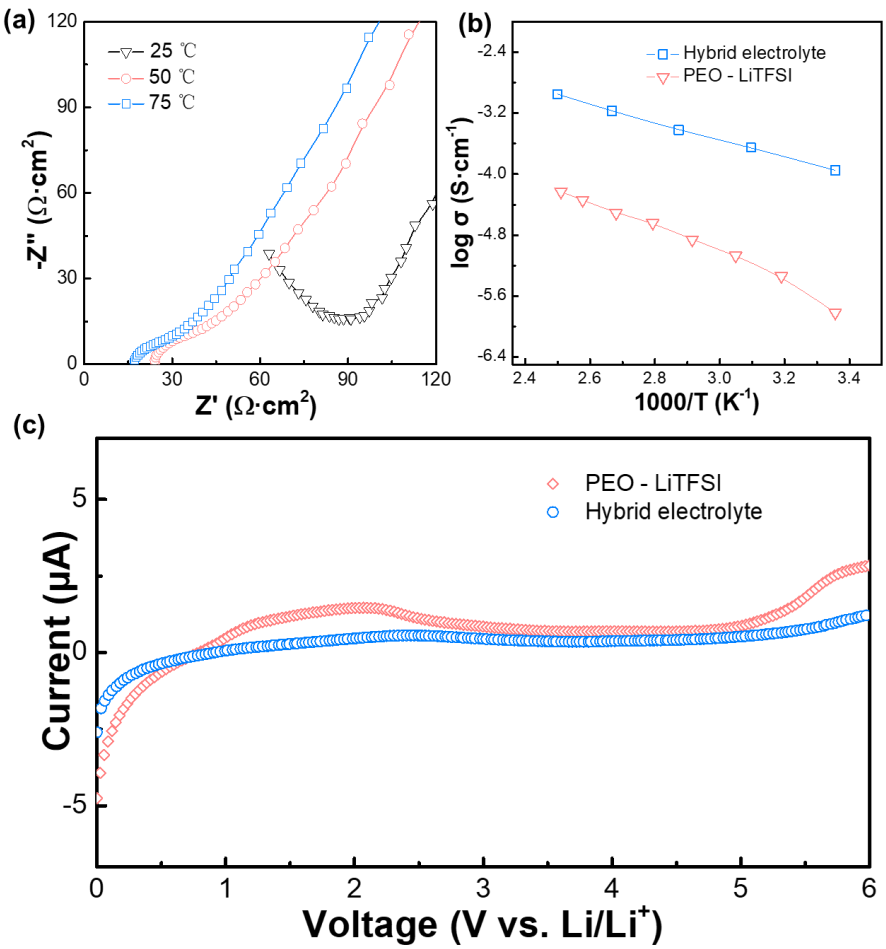

Figure 7-7. (a) EIS profiles of hybrid electrolyte at temperature 25℃, 50 ℃ and 75 ℃, in which the ionic conductivity at room temperature can reach$1.12 \times 10^{-4}\ \mathrm{S \cdot cm^{-1}}$. (b) Relation between ionic conductivity of electrolyte and temperature for both hybrid electrolyte and PEO-LiTFSI electrolyte. (c) LSV profile for hybrid electrolyte, in which the hybrid electrolyte exhibits a stable voltage window up to 6.0 V vs. Li/Li^+

As is shown before, the hybrid electrolyte has very good structural flexibility after the combination of polymer and c-LLZO fiber network, which does not display any obvious cracks during bending. To evaluate the influence of flexibility on the ionic

conductivity, the bend test was carried out with a hybrid electrolyte strip sealed in the Al/polymer soft packaging with carbon coated Al foil stretched out as current collector as displayed in Figure 7-8a. A controlled sample with the same mixture ratio of LLZO powders and PEO-LiTFSI was also examined in the bend test. EIS was exploited to analyze the ionic conductivity changes from the flat state to the fully bent state (Figure 7-8b). Normalized EIS curves show that hybrid electrolyte possesses a higher ionic conductivity than that of PEO-LiTFSI/LLZO powder electrolyte, which proves the ion transport efficiency of nanofiber network. It is also noted that the bent-state hybrid electrolyte has sufficiently high ionic conductivity for battery application, addressing the concerns about brittle inorganic electrolyte during manufacturing. In contrast, the PEO-LiTFSI/LLZO powder electrolyte presents a huge impedance increase in the bend test compared to its flat state. In fact, the control sample is barely flexible and easy to break into pieces, leading to poor conductivity performance after bending. The flexibility of the hybrid electrolyte can address the brittleness of inorganic solid electrolyte owing to the effective absorption of local strain energy by the nanofiber network and reduction in the stress concentration positions, which paves the way for large-scale manufacturing of Li-ion batteries with solid-state electrolytes.

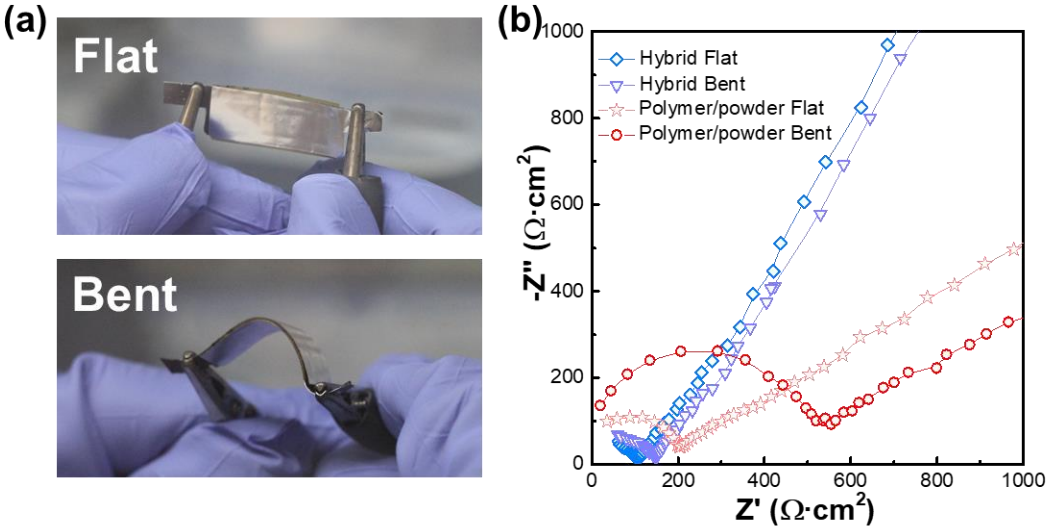

Figure 7-8. (a) images to show the flat and bent states of the hybrid electrolyte (b) EIS test for both the flat and bent state electrolyte, in which the ionic conductivity of hybrid electrolyte addresses the brittle issues for inorganic electrolytes.

7.4 Conclusion

In conclusion, we have successfully exploited bacterial cellulose nanofiber as a template to synthesize a polymer-ceramic hybrid electrolyte, in which a c-LLZO network acts as a scaffold coated with PEO-LiTFSI. This hybrid electrolyte possesses a 3D interconnected fiber network, presenting a structural flexibility comparable with conventional bulk inorganic ceramic electrolyte. The well-organized interconnected c-LLZO network not only provides fast Li-ion diffusion pathways, but also raises the concentration of free Li ions in the polymer electrolyte. As a result, the hybrid electrolyte exhibits an ionic conductivity of 1.12×10^{-4} S/cm at room temperature, much higher than that of controlled PEO-LiTFSI electrolyte (about $1 \times 10^{-6}\ S \cdot cm^{-1}$). LSV

curve reveals that hybrid electrolyte exhibits a stable voltage window up to 6.0 V vs. Li/Li^+, satisfying the requirement of most high-voltage Li-ion batteries. The ionic conductivity test for the flat and bent hybrid electrolyte addressed the concerns of brittleness for the inorganic electrolyte. This facile and applicable template-based approach provides new principles for the strategy of battery design that can be further extended to other electrolyte materials as well.

7.5 Experimental

Fabrication process of hybrid electrolyte

LLZO network preparation.

$LiNO_3$, $La(NO_3)_3{\cdot}6H_2O$, $ZrO(NO_3)_2{\cdot}6H_2O$ (from Alfa Aesar) were weighed stoichiometrically and dissolved in the 15% acetic acid solution. A stoichiometric amount of $Al(NO_3)_3{\cdot}9H_2O$ is also dissolved in the solution, as Al atoms act as the dopants in the LLZO to increase the concentration of Li vacancies and stabilize the cubic phase at room temperature. A BC nanofiber was cut in the dimension of 10 mm × 5 mm and placed in the freeze dehydration machine for 48 h to dry completely. The freeze-dried BC aerogel was soaked in the LLZO precursor solution for 2 h and then compressed to squeeze out the excess solution. The membrane template was then transferred to a constant temperature oven in vacuum for 24 h to volatilize the solvent and keep the membrane from encountering moisture. The membrane was calcined to 850 ℃ for 1h at a ramp rate 7 ℃/min. After calcination in a muffle furnace at 850 ℃ in the air, BC fibers were completely removed and the c-LLZO membrane was

fabricated. Then the calcined membranes were carefully transferred to the glovebox within Ar gas environment to protect the garnet structure by inhibiting the formation of Li_2CO_3.

Hybrid electrolyte preparation.

Poly (ethylene oxide) with average molecular weight about 600,000 g mol^{-1} was mixed with LiTFSI in acetonitrile (ACN) to form a homogeneous solution. The process should be performed in the glovebox to avoid contact with moisture. The PEO-LiTFSI solution was dropped on the LLZO network until the membrane was covered with enough polymer. Then, the sample was transferred to constant temperature oven at 65°C for 24 h to dry the hybrid membrane completely.

Characterization

Morphological characterization

Tescan XEIA3 SEM was used to characterize the morphology of the BC aerogel, LLZO nanofiber network, and the hybrid electrolyte. The XRD pattern was achieved using a D8 Bruker Advanced X-ray Diffraction system.

Electrochemical characterization

All the samples for EIS test were prepared in the glovebox. The ionic conductivity was examined by sandwiching hybrid electrolyte between two stainless steel plates. The range of frequency for EIS was 1MHz to 100 mHz. The

electrochemical stability of hybrid electrolyte was examined with LSV method at a sweep rate of 1 mV/s in the range of 0 to 6 V.

Chapter 8: Breaking Enabled Flexible Garnet Solid-State Electrolyte Membranes*

8.1 Abstract

Inorganic solid-state electrolytes for lithium metal batteries have attracted a lot of interest because of their non-flammability, high ionic conductivities, and wide electrochemical potential window. However, the poor flexibility of solid-state electrolytes due to their brittle nature severely hurdles their widespread applications. Our everyday experience that smaller objects are more difficult to break than larger ones is governed by fundamental fracture mechanics principal: The energy available in the smaller objects to drive the rupture scales down with the body size. Herein, based on fracture mechanics, we propose a mechanics-guided strategy to design a composite solid-state electrolyte with superb flexibility. Short flakes pre-cleaved from garnet-type electrolyte film are jointed with styrene-butadiene copolymer via additive manufacturing technique to form an assembled membrane. The dimensions of the electrolyte flakes are determined through parametric finite element studies to ensure the suppression of the brittle fracture for several target deformations bending curvature. In addition, the styrene-butadiene copolymer grid serves as a deformable buffer to further reduce the stress transferred to the garnet flakes. Therefore, excellent deformability can be imparted to the proposed composite solid-state electrolyte. The electrolyte membrane achieves an ultimate tensile strength of 5.12 MPa, three to five

* The results in this chapter have been submitted: Xie, H.; Bao, Y.; et al. Breaking Enabled Flexible Garnet Solid-State Electrolyte Membranes

times higher than the prevalent polyethylene oxide-based polymer electrolyte, as well as significant extensibility up to 220% before rupture. This facile and pragmatic strategy presents a new design principle for flexible solid-state electrolytes and paves the way towards the next-generation all solid-state batteries for microelectronic devices.

8.2 Introduction

The booming growth in electric vehicles, consumer electronics, and large-scale energy storage drives the surging needs for energy storage devices with high energy density, long-time cycling stability and high safety[3,219–222]. Lithium metal is revisited recently as a promising anode candidate to replace conventional ion intercalation anode materials and attracts much attentions owing to its low reduction potential (~-3.05 V versus standard hydrogen electrode) and high specific capacity (3860 mAh/g theoretically)[117,223–226]. Yet issues such as cycling stability and dendrite-growth induced safety concerns still haunt around, severely hurdling the widespread use of Li-metal batteries[224,227,228]. Developing enhanced inorganic solid-state electrolytes (SSEs) is one of the promising strategies to address these issues[123,130,229,230], among which cubic phase garnet-based electrolyte ($Li_7La_3Zr_2O_{12}$, usually doped with tantalum or niobium)[129,147,231] is heavily investigated because of its outstanding properties such as high ionic conductivity, excellent chemical and electrochemical stability window, as well as high modulus. However, the extreme brittleness of garnet SSEs leads to their poor flexibility, greatly limiting their scalability and potential usage for flexible electronic devices. Considerable efforts have been devoted to synthesize

inorganic/polymer electrolyte micro-architectures to mitigate the effects of the brittleness of garnet SSEs[197,232–236]. However, research showed that the existence of Li salts, such as lithium bis(trifluoromethanesulfonyl)imide (LiTFSI) in the hybrid electrolyte would induce the formation of Li dendrites[232]. Moreover, the employment of polymer electrolyte compromises the mechanical strength of the electrolyte, which in turn leads to a weaker suppression of the dendrite growth [237,238]. Although the unpredictable fracture of SSEs is extremely detrimental to the battery systems, it is interesting to note that the fractured electrolytes still maintain their apparent electrical properties, such as good ionic conductivity and high electrochemical stability window. Therefore, if fragments of SSE remain well-assembled in the layered sandwich structure of the battery so that each fragment can performs its electrochemical function, then the whole battery system can still operate normally.

We are all familiar with an everyday experience that it takes more effort to break a smaller and slender object than a smaller one. This regular observation is dictated by a fundamental fracture mechanics law: Rupture is an energetic competition between the deformation strain energy, which serves as the driving agency of crack growth, and the surface energy, which resists fracture progression. The strain energy stored in a deformed body scales with the volume, while the surface energy scales with the surface area. As the dimension of the body diminishes, at the same deformation level, strain energy rapidly scales down and falls below the surface energy. In this scenario, any further rupture ceases since the deformation cannot provide abundant energy to initiate new cracks or to drive the growth of the existing cracks. Therefore, there exists a threshold of flake dimension, under which the flakes become immune of

further cracking. Guided by such fracture mechanics principal, we resort to a strain energy-management approach and present a flexible copolymer/garnet composite SSE architecture. By directly modulating the dimension of garnet flakes, we successfully harness the strain energy below the fracture toughness of garnet SSE, thus eliminate further random electrolyte cracking in user condition. As a result, superb flexibility can be achieved with an ultimate tensile strength of 5.12 MPa, three to five times higher than the prevalent polyethylene oxide-based polymer electrolyte, as well as significant extensibility up to 220% before rupture. We perform a parametric study using finite element analysis (FEA) to get quantitative guiding principles based on the relation among SSE flake threshold, SSE thickness, and bending curvature. Experimental verifications were carried out to evaluate the analysis results from the parametric study, which presented good consistency between theory and practice. Under this direction, we fabricated the flexible LLZO flake array membrane, jointed with styrene butadiene (SB) copolymer. The as-synthesized LLZO electrolyte membrane presents high mechanical strength and flexibility, good electrochemical performance and nice compatibility with modern microelectronics manufacturing technologies. The facile and pragmatic design provides a promising methodology addressing the brittleness issue of SSEs and paves the approach for cost reduction and improvement of SSE scalability during battery manufacturing.

8.3 Results and discussion

Figure 8-1a illustrates the concept of this methodology, decreasing the aspect ratio of LLZO to inhibit the strain energy surpassing the limit defined by the fracture

surface, in which the SB copolymer bridges the flakes and buffers the strain concentration. SB copolymer possesses attractive properties such as high flexibility and extensibility, strong bonding strength with ceramic materials and high abrasion resistance. It is also widely employed as a binder additive for positive and negative electrodes in lithium batteries[239–242], and as the structural framework for polymer electrolytes[243]. Figure 8-1b schematically presents the major synthetic procedures of the flexible LLZO solid-state electrolyte membrane. A piece of cubic LLZO thin membrane was prefabricated as the starting material. The membrane was attached on a piece of thermal release tape, followed by being cleaved into square flakes with appropriate dimensions achieved through the parametric investigation and verified through experimental test. SB copolymer ink was extruded from the nozzle of an additive manufacturing printer[244,245] at tunable rate by controlling air flow to ensure the complete binding of neighboring LLZO flakes together to form a continuous electrolyte membrane. A free-standing LLZO film with satisfactory flexibility was fabricated after being transferred from the thermal release tape, in which each flake acts a vertical ion conductive unit for lithium ions. SB copolymer performs as a releasor with good flexibility which buffers the stress introduced during manufacturing, packaging, transportation, as well as applications. This pragmatic approach also enables the potential for a roll-to-roll process of flexible LLZO electrolyte membrane fabrication.

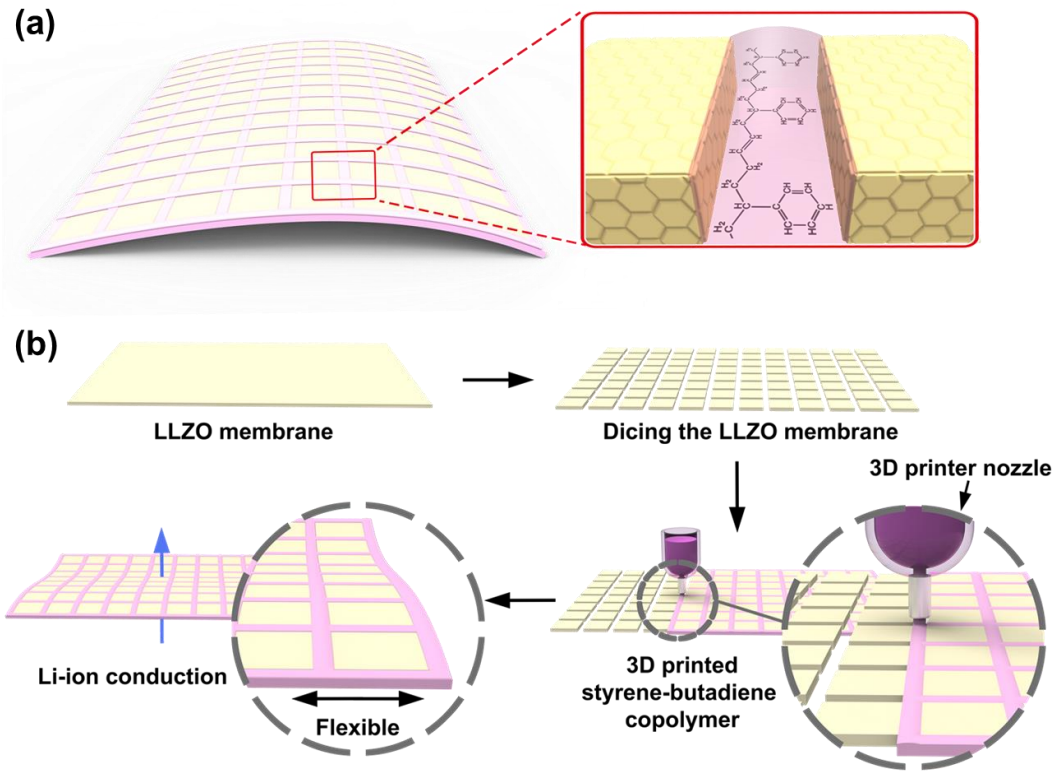

Figure 8-1. Schematic demonstrating the novel methodology for the fabrication of flexible LLZO solid-state electrolyte membrane. (a) Styrene butadiene copolymer was employed to join the short flakes. (b) General procedure for the composite electrolyte fabrication. A piece of LLZO membrane was diced into short flakes with diameters optimized from FEA parametric analysis, and SB copolymer ink was extruded from the 3D printer nozzle to bind firmly the neighboring LLZO flakes. The as-synthesized membrane maintains the existing advantage of SSEs while presents good flexibility.

The pivot of this methodology lies in the achievement of optimal flake dimensions, which can provide guidance for tailoring the aspect ratio of the flakes and maintaining sufficient mechanical strength to resist cracks. It is noted that in addition to the intrinsic mechanic strength of the SSEs, factors such as membrane thickness and

bending curvature exert influences on the appropriate dimension as well. Fracture mechanics demonstrate that the strain energy reserved in the SSEs increases with the volume of the flakes, whereas the fracture surface energy is proportional to the area, indicating the existence of a threshold where the two parameters present equal. To forestall the formation of cracks, dimension of the flakes should be curbed under the threshold, in which the impact of strain energy would not surpass that of fracture surface energy. Therefore, we envision that the LLZO membrane could be adjusted to be immune to fracture or even flexible if flake dimension parameters are reasonably tuned. To quantitatively analyze the threshold dimensions of the SSE flakes, a parametric FEA investigation was carried out to simulate the crack formation process with proper mechanic parameters from literature (Young's Modulus of LLZO is 150 GPa, Poisson ratio is 0.26, and the fracture toughness is 39.528 $MPa \cdot mm^{1/2}$)[246,247]. The general process for parametric analysis was depicted in Figure 8-2, in which a LLZO membrane stuck to the polyethylene tape was pressed onto a steel rod surface continually. High stress induced the formation of cracks, breaking the LLZO membrane into strain-released flakes. Owing to the existence of constraint between flakes and tape, each flake still behaves at a proper bending state as the membrane conformed firmly with steel rods. The strain energy in the LLZO flakes which already surpassed the fracture surface energy threshold would generate cracks and partially release along with the formation of smaller segmented parts, giving rise to the decrease of flake dimensions. The strain energy that decreased along with the volume reduction of flake was inadequate to overcome its fracture surface energy. As a result, the dimensions of the flakes were eventually stabilized into a certain range. The stable flake dimension

range was significantly influenced by the diameters of steel rods as high bending curvature would give rise to a decrease of the flake dimensions.

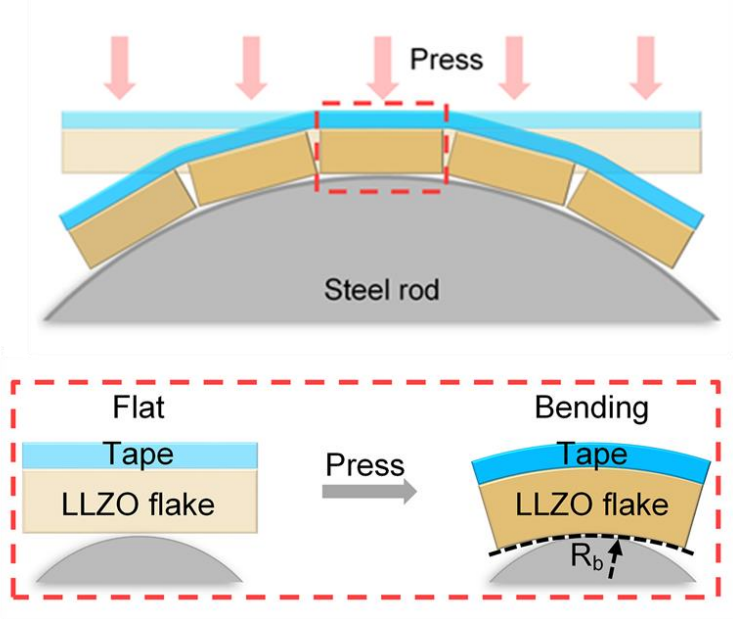

Figure 8-2. The schematic of LLZO breaking procedure during bending.

In the FEA analysis, LLZO flakes with thickness from 50 μm to 250 μm were evaluated under different bend state, in which both tape and LLZO flake were simplified as elastic materials owing to the small strain. Figure 8-3 presents a simulating example of a LLZO flake with 1.2mm long and 200 μm thick under different bending states. The top surface of the flake was under tensile stress, while the bottom surface was under compression. Generally, breaking initiation takes place on the top surface of the flake. A small notch was designed on the top surface functioning as a crevice generator for the stress concentration to trigger the fracture event. The stress evolution around the notch on the top surface indicates clearly that the stress concentration near the notch tip became more severe when the bending radius R_b

decreased gradually from flat to 6.25 mm. On the other hand, considering the LLZO flakes were under the same bending state (e.g R_b = 10 mm), the concentrated stresses near the notch tip were significantly relieved when the length of the LLZO flake decreased from 1.8 mm to 0.6 mm. As a result, the stress in the short LLZO flake cannot provide enough high fracture energy for crack initiation. Comparing the stress intensity factor evolution with LLZO Fracture toughness[246] K_{IC} (red dashed line), the critical bending state was determined for each LLZO flake with a certain length.

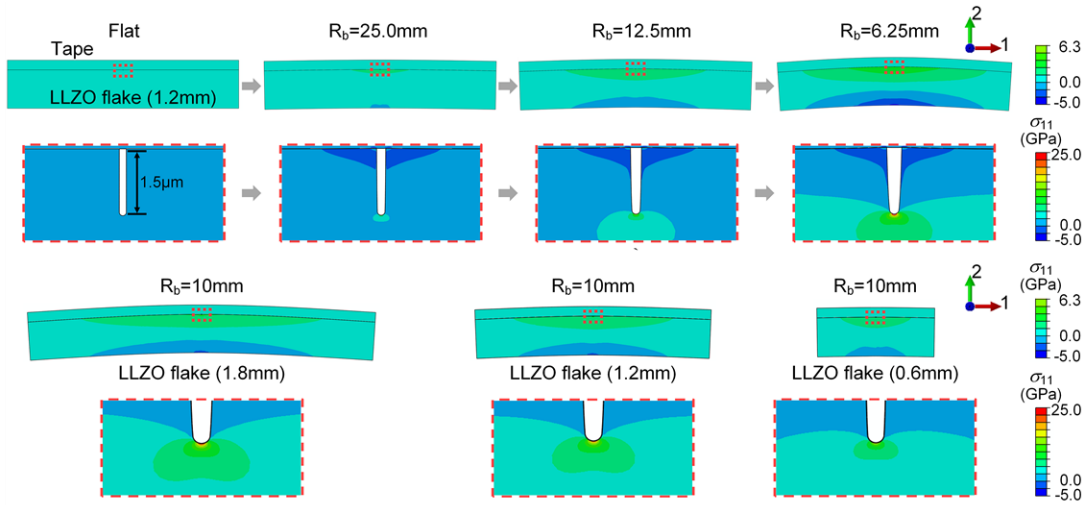

Figure 8-3. The FEA simulation of 200 μm thick LLZO flake (length 1.2mm) under bending state. The red dashed frames show the stress evolution around a tiny notch (1.5 μm depth).

The relation between bending curvature and stress intensities for various flake lengths was depicted in Figure 8-4a, in which LLZO flakes with shorter length can sustain a higher bending curvature. Figure 8-4b presents that the threshold dimension of LLZO flakes was also determined by the bending curvature, as LLZO flakes under higher bending state possess a shorter threshold dimension.

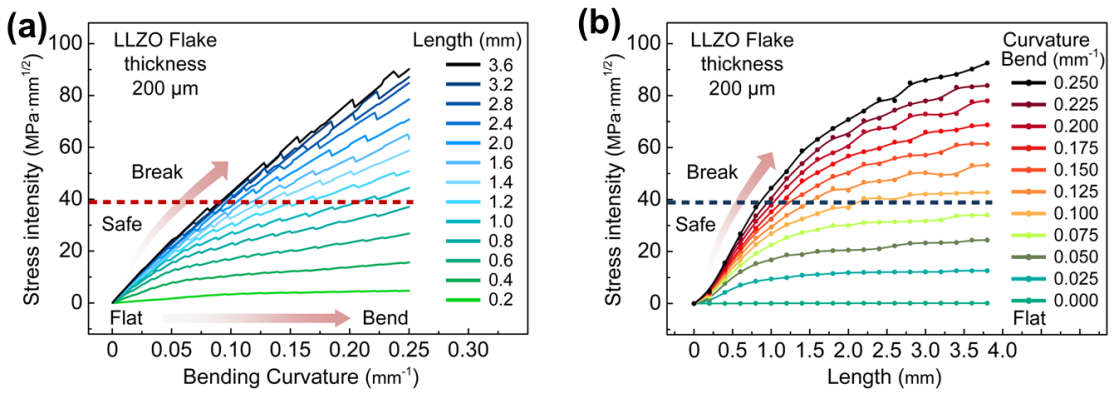

Figure 8-4 (a) The relation between stress intensity factor and bending curvature in 200 μm thick LLZO flakes with different length from 0.2 to 3.6 mm. (b) The relation between stress intensity factor and flake length under different bending curvature (from 0.0 to 0.20 mm^{-1}) in 200 μm LLZO flakes.

For different thickness of LLZO flakes from 50 μm to 250 μm, the FEA analyses were showed in Figure 8-5 and 8-6. Due to the higher bending stiffness, the thicker LLZO flake will have a higher threshold length for a certain bending extent.

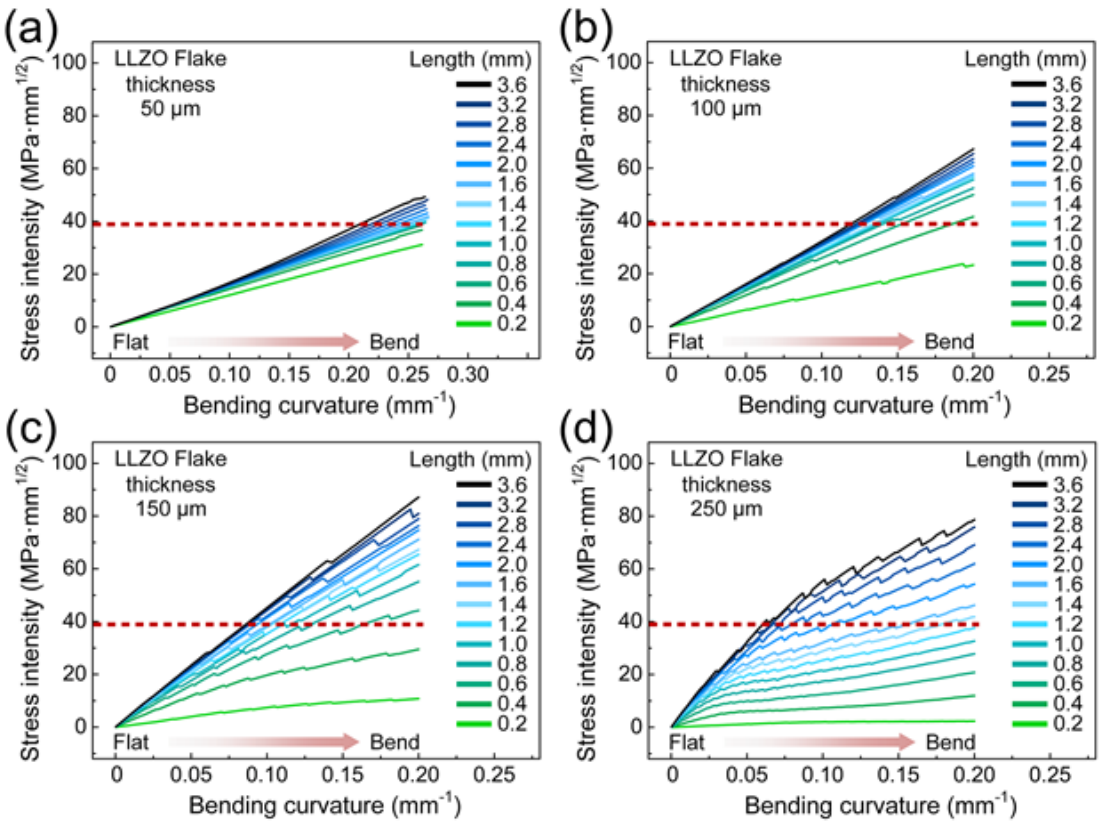

Figure 8-5. The relation between stress intensity and bending curvature in LLZO flakes with different length (from 0.2 to 3.6 mm) and different thickness (a) 50 μm, (b) 100 μm, (c) 150 μm, (d) 250 μm.

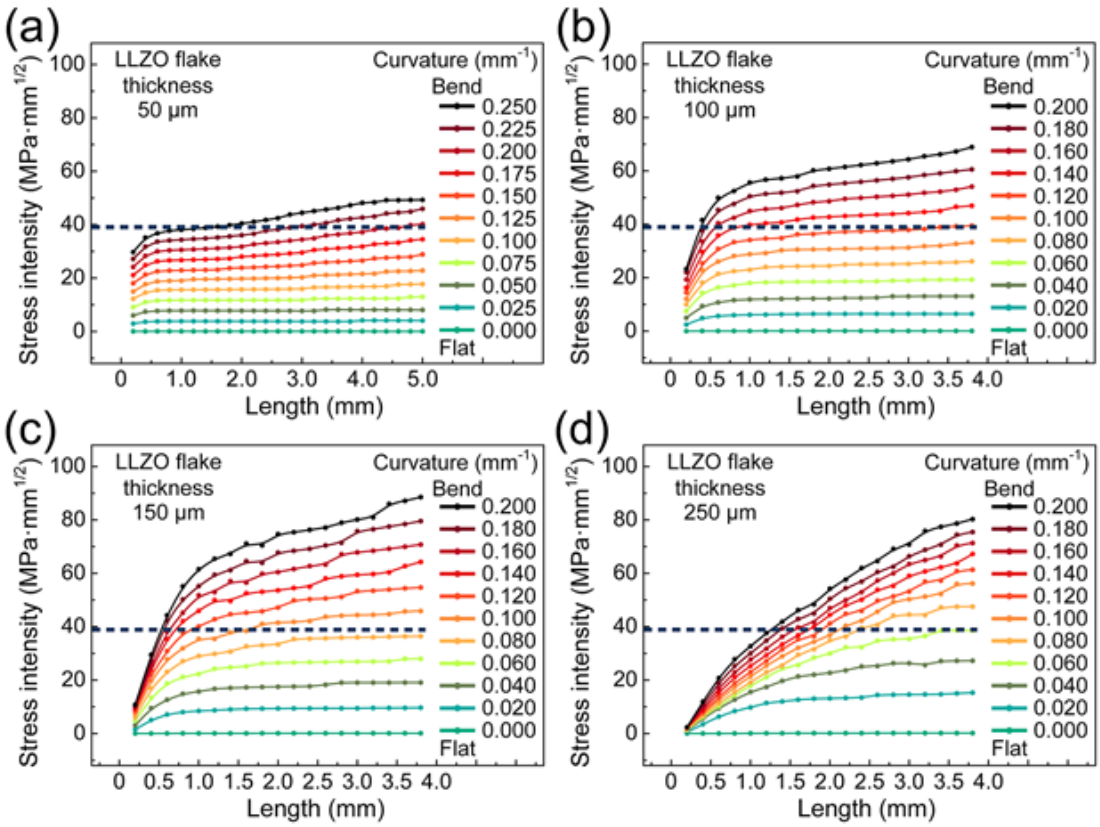

Figure 8-6. The relation between stress intensity and flake length under different bending curvature (from 0.0 to 0.25 mm^{-1}) in LLZO flakes with different thickness (a) 50 μm, (b) 100 μm, (c) 150 μm, (d) 250 μm.

Finally, a 3D suggested flake-stable size zone, which was influence by the bending curvature and thickness of LLZO flakes, was presented in Figure 8-7. These FEA results provide a significant guide for designing a stable pre-segregated LLZO electrolyte membrane with reasonable size LLZO flakes.

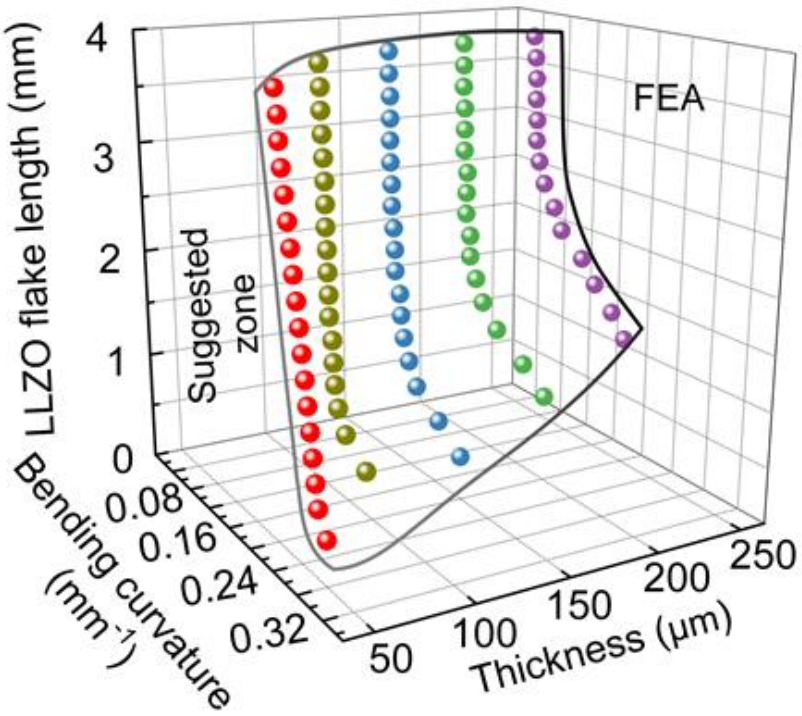

Figure 8-7. The threshold points derived from FEA simulation. Based on the bending curvature (bending radius) and the thickness of LLZO flakes, a suggested flake-stable zone is presented which is below the enveloping surface of these points.

To verify the parametric analysis results aforementioned, an experimental test was carried out to statistically evaluate the distribution of breaking flake dimensions. LLZO thin pellets with a fixed thickness of 200 μm were employed to be bended under different curvatures. One side of LLZO thin pellets with diameter 10 mm were attached on the tape and the side without tape was clung to the steel rods with diameters of 10 mm, 18 mm and 26 mm respectively. The thin pellets were bent to effectuate the conformation with the steel rods until no extra crack emerging. A consequent 90-degree rotation was performed, and the same operation was repeated until no more new flakes were generated during the whole process (the cracks were marked with dash red line in

Figure 8-8). Dimensions of as-formed flakes on these three different steel rods were collected statistically in Figure 8-8 and compared with the simulation results. Considering the randomness of crack emerging positions, the average dimensions of flakes for each pellet can be selected as the characteristic value to weigh the threshold lengths resisting the fracture at specific bending curvature. Statistic results show that all the dimensions for various rod diameters present typical Gaussian distributions with a distribution from several hundred micrometers to several millimeters. The characteristic values for flakes on 10 mm, 18 mm and 26 mm are 0.7 mm, 1.2 mm and 1.5 mm respectively. With the increase of the bend rod radius, the dimension of the flakes shows an increasing trend.

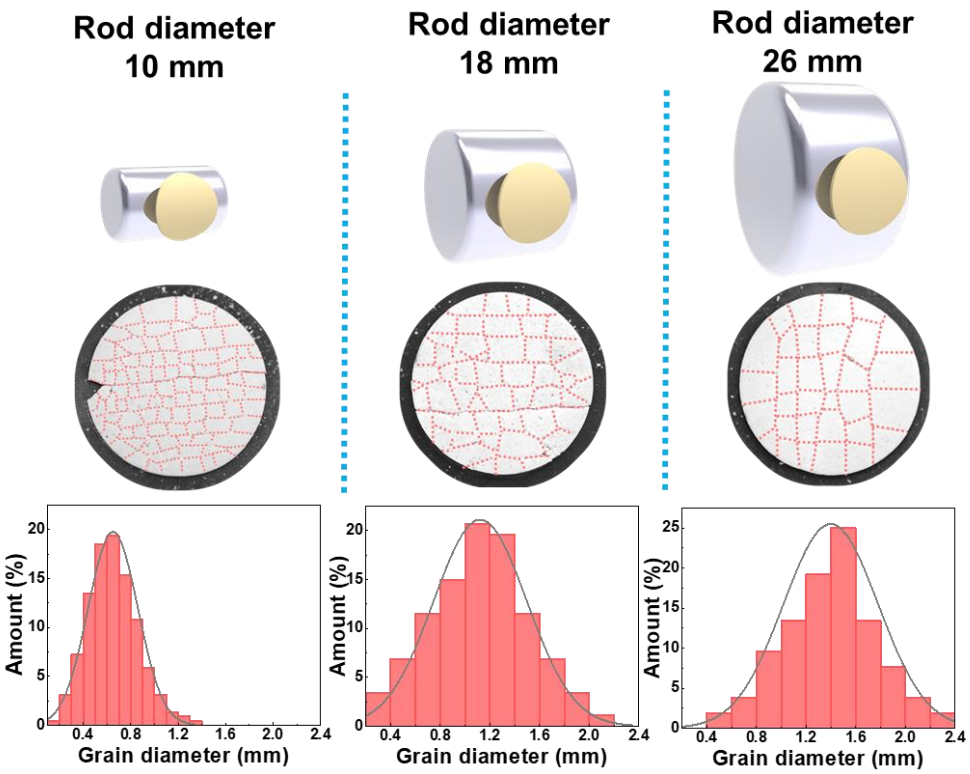

Figure 8-8. Experimental results of flake dimension distribution for LLZO thin pellets with thickness of 200 μm (the flake edges were marked with red dashed lines)

The experimental characteristic dimensions for different bending curvatures were drawn in Figure 8-9 to compare with the parametric analysis results. The parametric analysis presents a flake-stable zone below the threshold points calculated from the FEA study, where the flakes can maintain their shape and effectively resist the forming of cracks. The experimental characteristic values fall exactly in the flake-stable zone, very close to the calculated threshold curve, demonstrating a nice consistency between the experimental results and theoretical predictions.

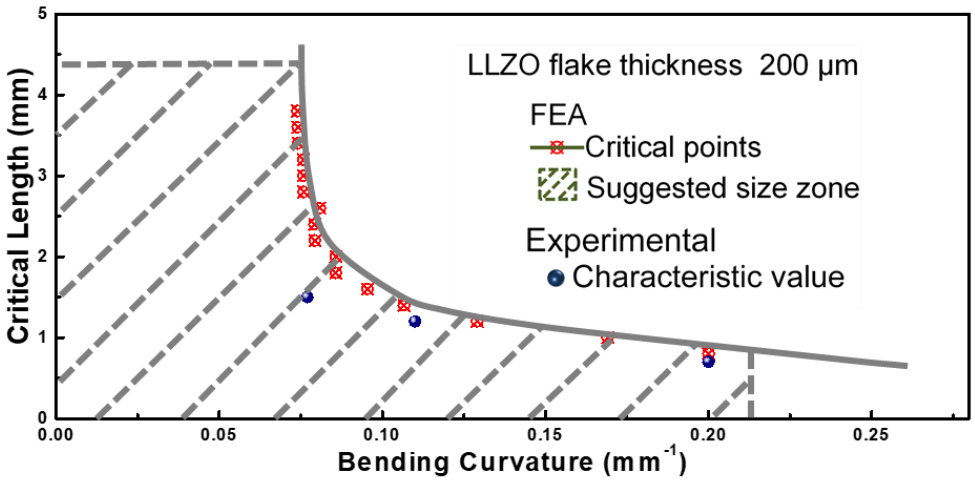

Figure 8-9. The characteristic LLZO flake lengths (blue points) in breaking experiment fall in the predicted flake-stable zone (shadow area), which is below the threshold points derived from FEA simulation.

Motivated by the parametric analysis results above, we introduce an electrolyte engineering methodology to pre-crack the solid-state electrolyte into flakes with sufficient stiffness to resist the fracture and bind them with flexible adhesive polymer to form a continuous membrane. This scalable approach for the fabrication of flexible

LLZO solid-state electrolyte membrane was successfully demonstrated by employing 3D printing technique. Figure 8-10a presents the SB copolymer printing process to fill the gap between flakes in the grid pattern with a preprogrammed design route. The SB copolymer ink stored in the syringe was vertically mounted to the 3D printer's stage and the prepared diced LLZO flakes attached on the tape was fixed on the silicon wafer with appreciate coordinates. During the printing process, SB copolymer ink is extruded from the nozzle at appropriate speed which could be tuned by air flow to ensure the complete binding of neighboring LLZO flakes. Figure 8-10b presents one specific example of the as-synthesized electrolyte membrane, in which the 3D printed SB copolymer bonded structure presents high robust feature, which allow for direct handling after the SB copolymer was completely cured. The flakes pre-cleaved from membrane with thicknesses varying from 50 μm to several hundred micrometers present a square shape with dimension of 1.2mm x 1.2 mm (scale bar 1 mm, Figure 8-10c). Figure 8-10d and e show the scanning electron microscope (SEM) image for the surface morphology of the membrane, in which a clear boundary between the LLZO flakes and SB copolymer can be observed. Figure 8-10f presents the cross-sectional image of the membrane with thickness that can be tailored from 50 μm to several hundred micrometers. Figure 8-10g depicts the energy-dispersive X-ray spectroscopy (EDS) mapping results for typical elements, in which the Zr and La elements belong to the LLZO electrolyte and carbon belongs to the SB copolymer, indicating a good and distinct bonding was formed between the SSE and SB copolymer.

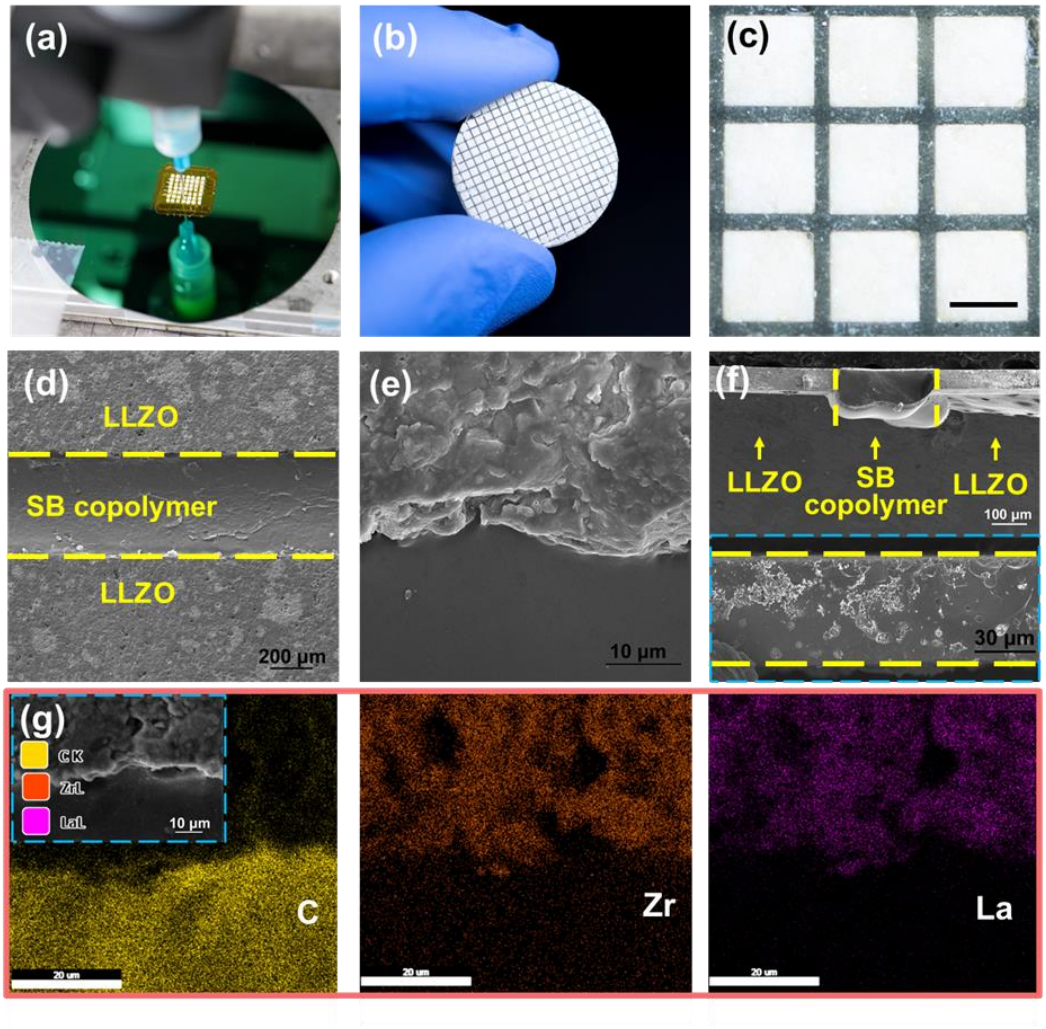

Figure 8-10. (a) Photo of the binding process with SB copolymer extruded from the 3D printer nozzle. (b) Photo of as-synthesized electrolyte membrane. (c) Magnified photo of the square flakes bound with SB copolymer (scale bar: 1mm). (d) and (e) SEM images present the surface morphology of the connection area of the LLZO and SB copolymer. (f) Cross-sectional SEM image of the as-synthesized membrane. (g) EDS mapping depicts the C, Zr and La element distribution

To evaluate the phase structure of the membrane, X-ray diffraction analysis (XRD) was employed to detect the composite solid-state electrolyte membrane. Figure

8-11 depicts the XRD patterns, in which diffraction peaks present great consistency with the cubic-phase garnet $Li_7La_3Zr_2O_{12}$ (Joint Committee on Powder Diffraction Standards card number: 80-4947). It is noted that the broad peak of SB copolymer at around 19.7° is suppressed by the strong crystalline peaks from LLZO. The XRD patterns prove that the LLZO flakes maintain cubic-garnet phase after bonding with SB copolymer.

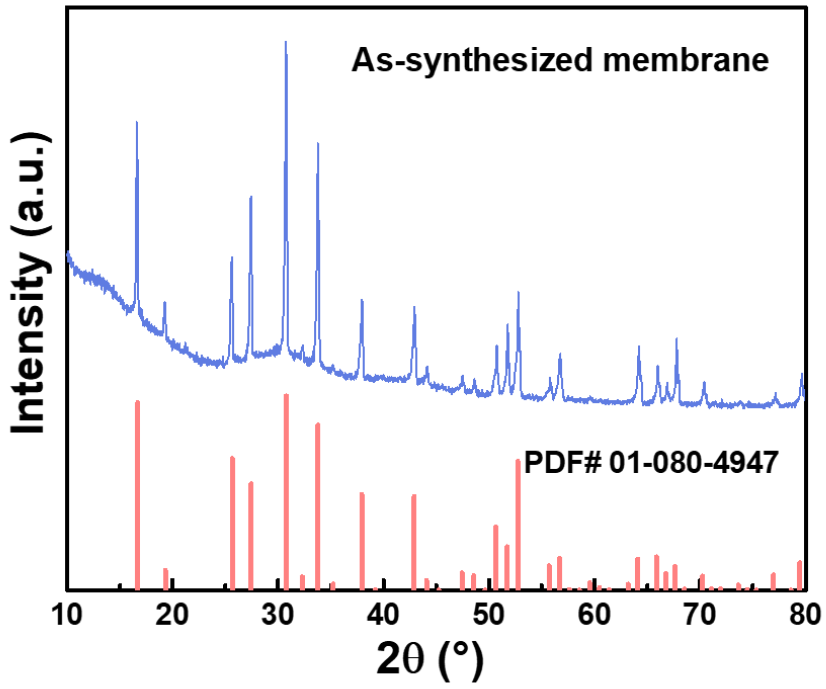

Figure 8-11. XRD patterns for the membrane. (b) FTIR of the SB copolymer and electrolyte membrane from 3250 cm-1 to 640 cm-1. Good stability of the SB copolymer in the membrane can be observed.

To further investigate the chemical stability of cubic garnet flakes with the SB copolymer, Fourier-transform infrared spectroscopy (FTIR) was exploited to evaluate

the pure SB copolymer and the composite electrolyte membrane, presented in Figure 8-12a from 3250 cm^{-1} to 640 cm^{-1}. The absorption peaks located at 3000 cm^{-1} and 3080 cm^{-1} are attributed to the aromatic hydrogen or unsaturated carbon. Signals at 2915 cm^{-1} and 2844 cm^{-1} are related to the vibration peaks of methylene groups[248,249]. Compared with pure SB copolymer, it is noted that the electrolyte membrane presents similar absorption results, which demonstrates good chemical stability and compatibility between SB copolymer and LLZO. Figure 8-12b shows the FTIR transmittance spectra of pure LLZO powders, SB copolymer, as well as the membrane in the fingerprint region from 1100 cm^{-1} to 640 cm^{-1}. The band at 864 cm^{-1} of the membrane comes from the strong characteristic vibration of Zr-O-Zr group in LLZO[247,250].

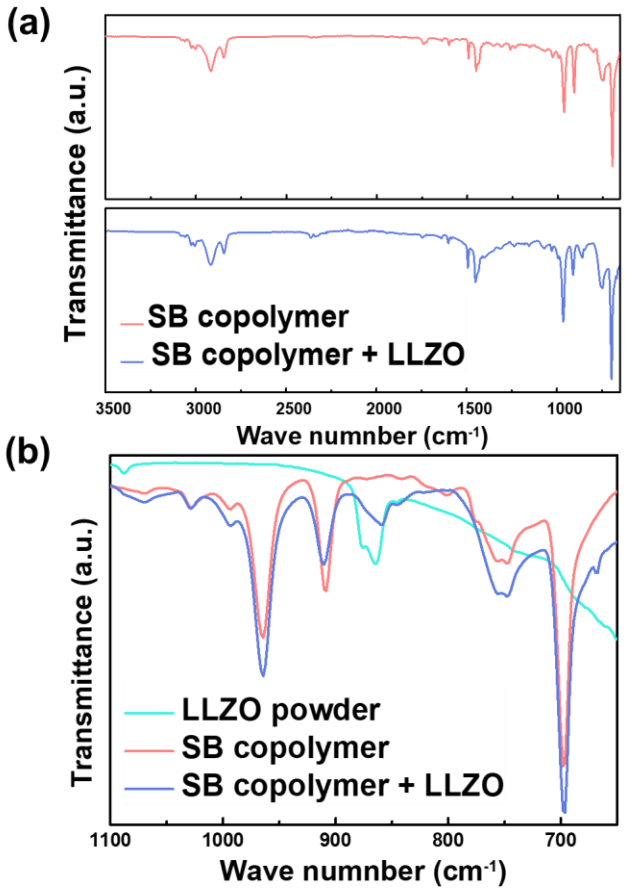

Figure 8-12. (a) FTIR of the SB copolymer and electrolyte membrane from 3250 cm-1 to 640 cm-1. Good stability of the SB copolymer in the membrane can be observed (b) FTIR of the fingerprint region from 1100 cm-1 to 640 cm-1. LLZO brought about absorption peaks around 864 cm-1 in the membrane due to Zr-O-Zr group vibration.

To evaluate the mechanical properties of the as-synthesized membrane, tensile test was carried out to investigate the bond strength between LLZO flakes and SB copolymer. Figure 8-13 shows the engineering stress-stain curves for the as-synthesized membrane and the comparison with related reports on flexible polymer electrolytes[251,252]. Our membrane demonstrates a significantly high ultimate tensile strength of 5.12 MPa, three to five times higher than the current prevalent polyethylene oxide (PEO) type solid-polymer electrolyte (PEO-LiTFSI) or its hybrid mixture with inorganic nasicon solid electrolyte. In addition, this membrane possesses high extensibility which can be stretched to 220% before rupture, ensuring excellent flexible capability.

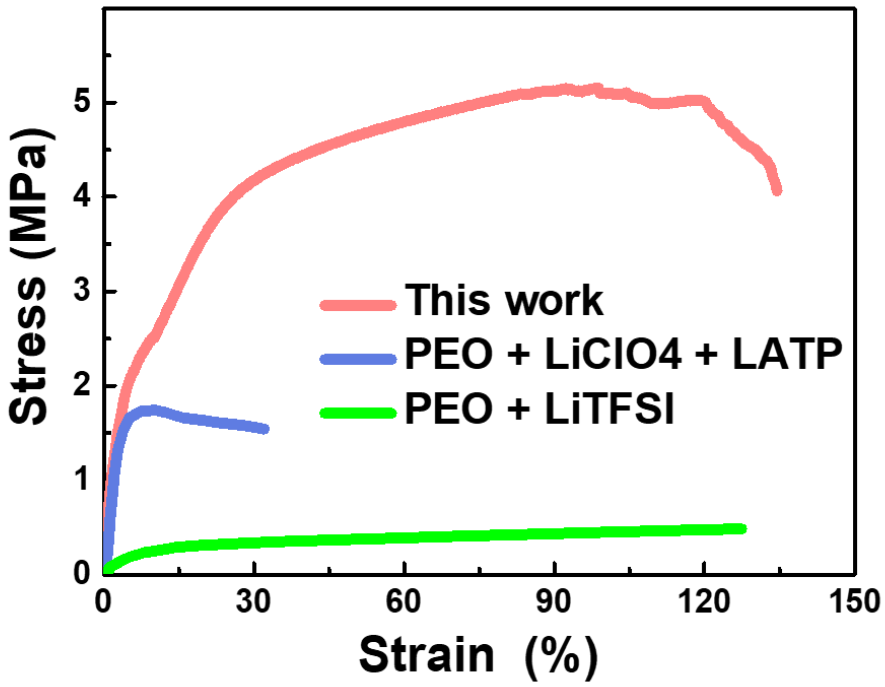

Figure 8-13 Engineering stress-strain curve for the as-synthesized membrane and its comparison with current prevalent PEO based polymer[251] or hybrid electrolytes[252].

With the elastomeric SB copolymer as buffering grid, the composite electrolyte membrane presents can easily withstand bending curvatures analyzed in the parametric study (Figure 8-14). To prepare the Li metal coated membrane for electrochemical performance characterization, a 400 μm thick pellet was pre-melted with Li metal on both sides and after the pellet was broken into small flake segments, SB copolymer was employed to seal the gap between different flakes.

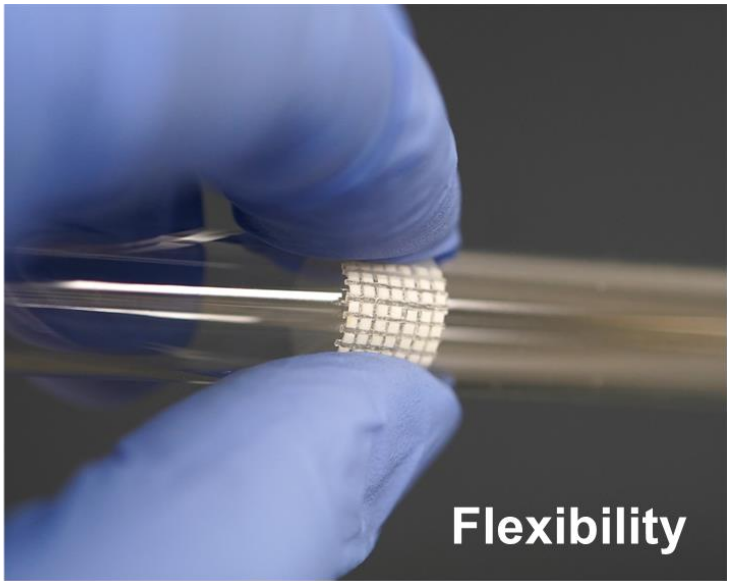

Figure 8-14. Photo demonstrating good flexibility of the membrane.

To evaluate cycling capability of the membrane against Li dendrites, a symmetric Li | electrolyte | Li cell was employed to carry out the charge and discharge processes. Figure 8-15a presents the typical Nyquist plot of the Li | electrolyte | Li cell achieved from the electrochemical impedance spectroscopy (EIS), two semi-circles of which are attributed to the impedance of garnet SSE (high frequency R1) and the interface resistance (low frequency R2) respectively, as showing in the equivalent circuit. During charge and discharge processes at a constant current, lithium ions were plating and stripping through the membrane to mimic the operation of charging and discharging lithium metal batteries. Figure 8-15b presents the voltage profiles of the symmetry cell with the electrolyte membrane around 50 cycles at a constant current density of 0.1 mA/cm^2 at room temperature. The voltage profiles show stable curves which indicates stable impedance and excellent stability of the Li metal and LLZO membrane interface during electrochemical cycling.

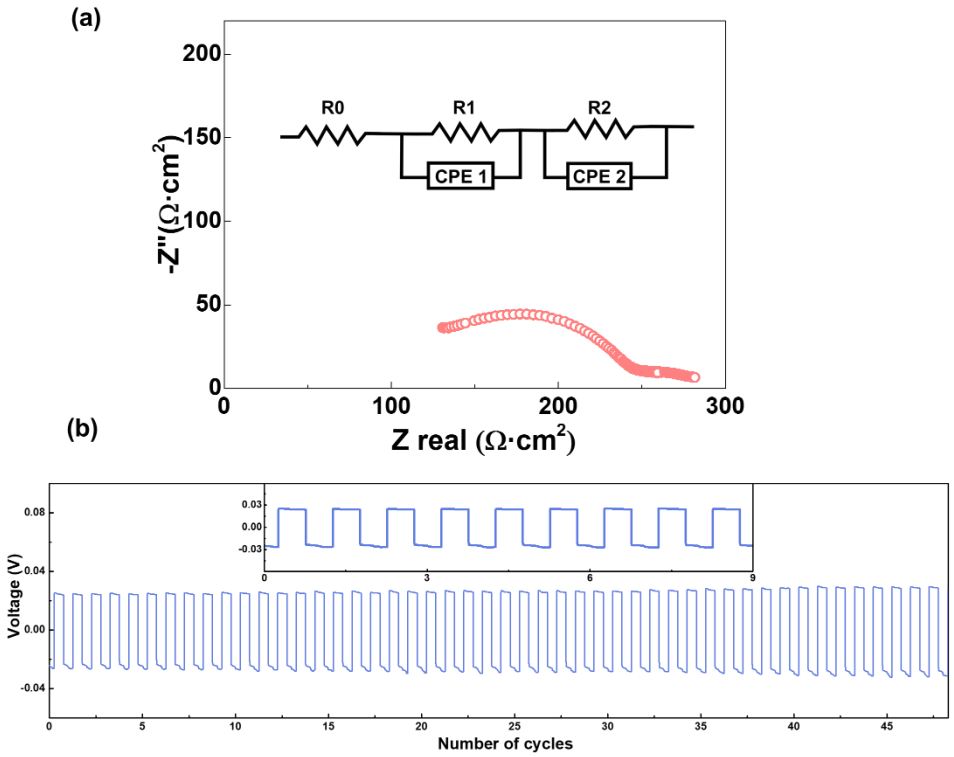

Figure 8-15. (a) EIS profile of the membrane at room temperature. (b) Voltage profile of the lithium plating/striping cycling with a current density of 0.1 mA/cm^2 at room temperature.

8.4 Conclusion

We have demonstrated an effective "break management" strategy to design a flexible LLZO electrolyte membrane, in which the electrolyte film was cleaved into short flakes and then were bound together with SB copolymer, resisting brittle fracture through buffering the excessive stresses from each short flake. Parametric FEA study was carried out to analyze the relations between the dimensions of the flakes and multiple parameters, delivering the optimal dimensions of flakes with various

electrolyte thickness under different curving state. The flexible membrane maintains all existing attractive properties of LLZO solid-state electrolyte and presents an ultimate tensile strength of 5.12 MPa enhanced by the copolymer/electrolyte periodic structure, three to five times higher than the prevalent PEO-LiTFSI solid electrolyte or its hybrid with inorganic nasicon solid electrolyte. In addition, the composite electrolyte possesses significant high extensibility which can be stretched to 220% before rupture, ensuring excellent flexible capability. This high flexibility and nice compatibility with modern manufacturing technologies prove high application potential for future microelectronics. This scalable strategy and the unique design methodology can also be applied to other inorganic brittle membrane to improve the flexibility.

8.5 Experimental

Finite element parametric analysis

A LLZO flake under bending which simplified from the LLZO breaking experiment was modeled through a standard analysis in ABAQUS 6.13 (See details in Supporting Information). In the simulation, the top surface of the LLZO flake was tied to the tape, while the bottom surface of the LLZO flake was in contact with the surface of the steel rod. A displacement load was applied on the two sides of LLZO flakes to model the bending process. A 1.5 μm depth notch was considered at the top surface of the LLZO flake for calculating the stress intensity. Then, a series of LLZO flakes with different thickness and different length were modeled to determine the critical breaking length of LLZO flakes.

Materials Synthesis

The Al-contained $Li_{6.75}La_3Zr_{1.75}Ta_{0.25}O_{12}$ garnet powders were synthesized via solid-state reaction method. $LiOH{\cdot}H_2O$ (99.9%, Sigma Aldrich), La_2O_3 (≥ 99.9%, Sigma Aldrich), ZrO_2 (99.9%, Sigma Aldrich) and Ta_2O_5 (99.9%, Sigma Aldrich) were used as precursors, with stoichiometric amounts mixed in isopropyl alcohol (IPA) for 12 h. 10% excess $LiOH{\cdot}H_2O$ were induced to compensate the loss of lithium. Al2O3 nanopowders (around 2%wt of the total materials) were added to improve the sintering process. The stoichiometrically mixed powders were calcined at 920 ℃ for 12 h. Then the powders were mixed with IPA and ball-milled for 9 h. The powders were pressed into thin membrane at 300 MPa and sintered at a temperature 1150 ℃ for 9 h.

Li metal was exploited to test its stability with the SB copolymer and the image of the contact between the two were shown in figure 8-S1. No obvious interface change could be observed after the SB copolymer got completely cured.

Membrane fabrication

The membrane was attached to a thermal release tape and was cut into small flakes with dimension 1.2 mm X 1.2 mm to form a garnet array. A 3D printer was employed to extrude the SB copolymer glue to seal the gap between flakes. After the copolymer is completely cured, the membrane was transferred to a hot plate to remove the thermal release tape from the garnet array. The two sides of the membrane were polished to get rid of impurities.

Materials characterization.

The morphologies of the electrolyte were evaluated on a Tescan XEIA Plasma FIB/SEM. X-ray diffractions (XRD) of the binary alloys were performed on a D8 Bruker Advanced X-ray Diffraction system using a Cu Kα radiation source operated at 40 kV and 40 mA. A single column tabletop model testing system (Instron, USA) was used to perform mechanical tests. A 1000 N load cell was used with a nominal strain rate of 2 mm/min.

Electrochemical measurement.

Li metal was melted on the surface of LLZO membranes, the membranes were cleaved into flakes and SB-copolymers was employer to bind the flakes together. Electrochemical tests of Li/garnet/Li symmetric cells were tested on a BioLogic VMP3 potentiostat at room temperature. The electrochemical impedance spectra (EIS) were performed with a 20 mV AC amplitude in the range of 100 mHz to 1 MHz. Galvanostatic stripping-plating of the Li/garnet/Li symmetric cells was recorded at room temperature with a current density of 100 $\mu A/cm^2$. The cells were placed in an argon filled glovebox to conduct all measurements. A Thermo Nicolet NEXUS 670 FT-IR was used to measure the FT-IR spectrum.

8.6 Supporting Information

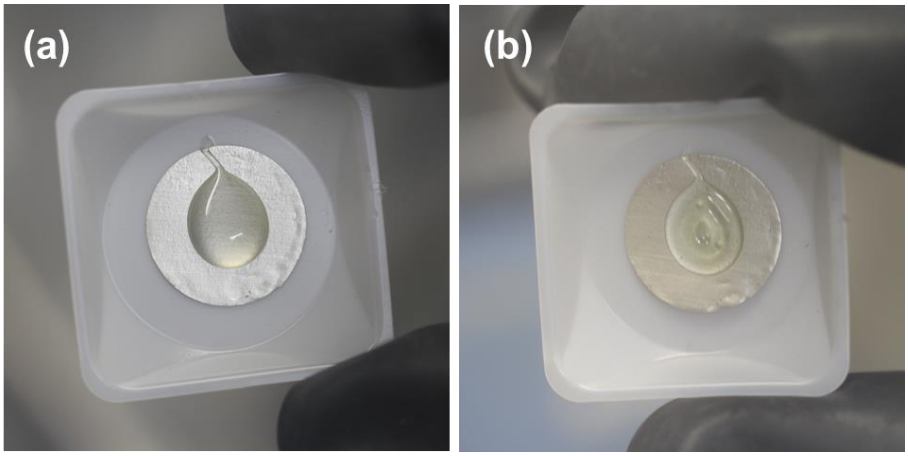

Figure 8-S1. The stability test of the SB copolymer with Li (a) when Li metal and the SB copolymer contact (b) good stability after the SB copolymer get completely cured (48 h)

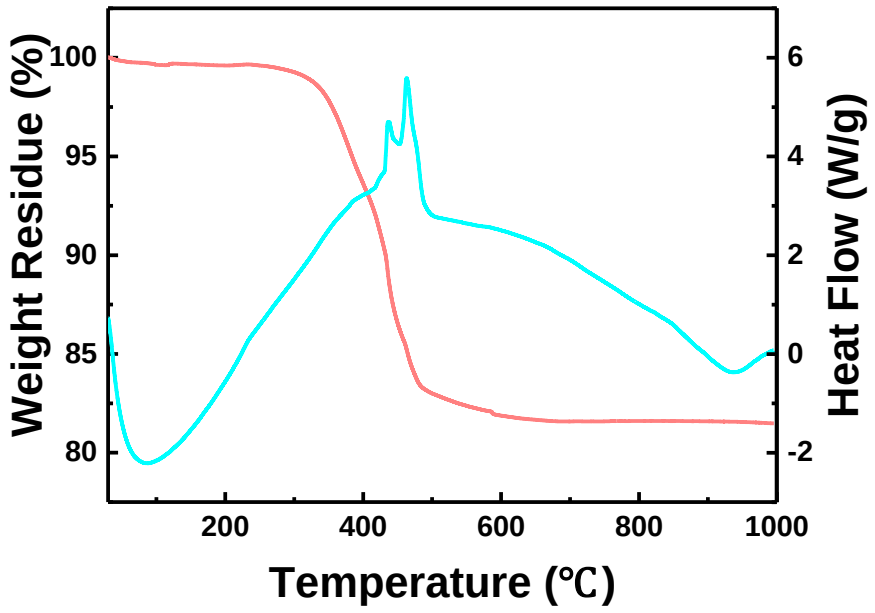

Figure 8-S2. Thermogravimetric analysis of the as-synthesized membrane.

Models		LLZO flake length (mm)												
		0.2	0.4	0.6	0.8	1.0	1.2	1.4	1.6	2.0	2.4	2.8	3.2	3.6
LLZO flake Thickness (μm)	100	1-1	1-2	1-3	1-4	1-5	1-6	1-7	1-8	1-9	1-10	1-11	1-12	1-13
	150	2-1	2-2	2-3	2-4	2-5	2-6	2-7	2-8	2-9	2-10	2-11	2-12	2-13
	200	3-1	3-2	3-3	3-4	3-5	3-6	3-7	3-8	3-9	3-10	3-11	3-12	3-13
	250	4-1	4-2	4-3	4-4	4-5	4-6	4-7	4-8	4-9	4-10	4-11	4-12	4-13

Table 8-S1. Geometric parameters of LLZO flake used in FEA modeling

Parameters	Values
E_{tape}, **Young's Modulus of tape[253], (BOPP)**	2.5 GPa
ν_{tape}, **Poisson ratio of tape**	0.43
E_{LLZO}, **Young's Modulus of LLZO[254]**	150 GPa
ν_{LLZO}, **Poisson ratio of LLZO[255]**	0.26
K_{IC} **LLZO Fracture toughness**	39. 528 MPa·mm$^{1/2}$

Table 8-S2. Parameters used in FEA modeling

Detailed finite element modeling (FEM) method

In the LLZO sheet breaking experiment, LLZO flakes were under bending due to the constraints on each other and the tape. We modeled a single LLZO flake bending process through a standard analysis in ABAQUS 6.13. To determine the critical breaking length of LLZO flakes. Four different thicknesses of LLZO flakes, 50 μm, 100 μm, 150 μm, 200 μm, 250 μm were considered. For each thickness, a series of LLZO flakes with different length from 0.2 mm to 3.6 mm were adopted in the modeling. The geometric parameters of LLZO flakes with different thickness and length were showed in Table S1. These 2D models were analyzed at the plain strain

condition. The thickness of tape film was 50 μm, and the length was equal to the LLZO flakes. Due to the small strain in the tape during the bending process, both of the tape and LLZO flake were simplified as elastic materials. The mechanical parameters were shown in Table S2. The top surface of the LLZO flake was tied to the tape, while the bottom surface of the LLZO flake was in contact with the surface of the steel rod, which was treated as an analytical rigid object in the simulation. A displacement load was applied on the two sides of LLZO flakes to model the bending process. A 1.5 μm depth notch was introduced in the middle position on the top surface of the LLZO flake for calculating the stress intensity. The bending curvature was calculated based on the displacement load. While the simulated stress intensity exceeds the LLZO Fracture toughness[246] K_{IC}, the surface notch started to crack. Based on this criterion, the relation among the critical lengths of LLZO flake, the bending curvature (bending radius) and thickness was decided.

Chapter 9: Conclusion and Future Outlooks

The research presented in this dissertation has focus on the high temperature process approaches for material nanostructure designing in two distinct emerging electrochemical systems, with a range of physical, chemical, electrochemical characterizations. Throughout this process, a number of techniques have been employed to overcome the limitations of promising candidate material systems, which can significantly improve their properties such as chemical stability, electrochemical durability, as well as flexibility and adaptability for harsher operation conditions. The reported result in this research can offer a thorough picture of the methods and directions which help explain the mechanism, guide the optimization process, as well as inspire novel strategies for advances in the material design. Here some of the most interesting and important findings are summarized, together with ideas for future work to resolve the remaining questions in the current systems.

9.1 Research summary

Necklace-like Silicon Carbide and Carbon Nanocomposites

We employ Joule heating on the C/Si nanocomposite fibers to do an in-situ synthesis of a SiC/carbon necklace-like nanostructure, in which the nanoparticles of SiC can be interconnected with each other while still maintaining their high specific surface area. The CSNF acts as a reservoir to provide C and Si atoms before Joule heating, as a micro furnace to heat the pristine reagent during Joule heating, and finally as the substrate to host the formed SiC nanoparticles. Pristine CSNF films were heated

to 2000 K, which significantly improved the graphitic structure of the carbon nanofibers, thereby increasing the conductivity of substrate. The high-temperature enabled by the Joule heating efficiently boosts the in-situ formation of SiC, while also enhancing the bonding strength between the SiC nanoparticles and carbon nanofibers. SiC nanoparticles can be homogeneously distributed and strongly anchored on the carbon nanofibers, which is advantageous for the potential application of this novel composite. Joule heating, as an effective and scalable method, has the potential to promote the in-situ synthesis of other homogenous carbide nanoparticles, which in turn could have enhanced bonding strengths with carbon-based substrates and similar homogeneous distribution similar to the results discussed herein.

Ultrathin-Graphene-Coated Metal Nanoparticles for Oxygen Reduction Reaction

We report a one-step synthetic technique to simultaneously fabricate supported Co@graphene core-shell nanoparticles. This strategy presents several advantages, such as generation of core-shell nanostructures in one facile processing step, tunability and control over graphene shell thickness down to monolayer graphene, as well as the abundance of substrate candidates. The ORR test shows that their stability and durability exceeded previously reported PGM-free catalysts. DFT calculations proved that local contact between Co core and graphene shell produces carbon atoms with lower electron density which promote ORR process. This facile synthetic approach provides a pathway towards the design and development of metal/graphene core-shell nanoparticles with controllable graphene coating thickness for a wide range of potential applications in the fields of catalysis and beyond.

Improving the Interface between Li/Na Alloys and Various Substrates for Batteries

We report that by adding alloying elements to molten Li and Na, the surface energy and viscosity of negative electrodes can be manipulated to directly solder onto various substrates. As a demonstration, a Li-Sn alloy was soldered onto the surface of garnet SSEs within 10 seconds and exhibits a conformal and tight contact. The alloy significantly decreases the interfacial resistance against garnet SSE to as low as ~7 $\Omega \cdot cm^2$. Subsequent electrochemical studies confirm the excellent stability of both the interface and the alloy electrodes during the long time and high capacity cycling. To demonstrate the versatility of this alloy-based soldering technique, several other Li binary alloys were studied and display similar wetting behavior on metal, ceramic, and polymer substrates. Moreover, this direct soldering technique was extended to molten Na alloy systems, and in particular, a Na-Sn alloy was successfully coated on an alumina substrate. This direct soldering technique will inspire new strategies to develop safe Li and Na metal batteries with high energy densities.

High Temperature Thermal Pulse for High Performance Solid State Electrolyte

We demonstrate a thermal pulse technique for rapid ceramic surface processing that can quickly clean surface contamination and restore the materials in less than 2 s. As a demonstration, we successfully cleaned Li_2CO_3 contamination from the surface and grain boundaries of garnet SSEs. The ultra-short processing time prevented Li loss and any phase change of the garnet SSE at high temperature. We systematically studied the formation of oxygen vacancies by this process, which results in an increase in ionic

conductivity of the garnet SSEs from about 1.6×10^{-4} S/cm to 3.2×10^{-4} S/cm. The rapid thermal pulse treatment also significantly improved the electrochemical stability of the material. Additionally, the critical cycling current density in symmetric cells increased from 100 μA/cm^2 to 500 μA/cm^2 after the thermal pulse treatment. This unique Joule heating method and ultra-fast process enable the potential for roll-to-roll processing for ceramic surface treatment in practical applications.

Garnet-Polymer Solid Electrolyte Templated by Bacterial Cellulose

We have successfully exploited bacterial cellulose nanofiber as a template to synthesize a polymer-ceramic hybrid electrolyte, in which a c-LLZO network acts as a scaffold coated with PEO-LiTFSI. This hybrid electrolyte possesses a 3D interconnected fiber network, presenting a structural flexibility comparable with conventional bulk inorganic ceramic electrolyte. The well-organized interconnected c-LLZO network not only provides fast Li-ion diffusion pathways, but also raises the concentration of free Li ions in the polymer electrolyte. As a result, the hybrid electrolyte exhibits an ionic conductivity of 1.12×10^{-4} S/cm at room temperature, much higher than that of controlled PEO-LiTFSI electrolyte (about $1 \times 10^{-6}\ \mathrm{S \cdot cm^{-1}}$). LSV curve reveals that hybrid electrolyte exhibits a stable voltage window up to 6.0 V vs. Li/Li$^+$, satisfying the requirement of most high-voltage Li-ion batteries. The ionic conductivity test for the flat and bent hybrid electrolyte addressed the concerns of brittleness for the inorganic electrolyte. This facile and applicable template-based approach provides new principles for the strategy of battery design that can be further extended to other electrolyte materials as well.

Breaking Enabled Flexible Garnet Solid-State Electrolyte Membranes

We have demonstrated an effective “break management” strategy to design a flexible LLZO electrolyte membrane, in which the electrolyte film was cleaved into short flakes and then were bound together with SB copolymer, resisting brittle fracture through buffering the excessive stresses from each short flake. Parametric FEA study was carried out to analyze the relations between the dimensions of the flakes and multiple parameters, delivering the optimal dimensions of flakes with various electrolyte thickness under different curving state. The flexible membrane maintains all existing attractive properties of LLZO solid-state electrolyte and presents an ultimate tensile strength of 5.12 MPa enhanced by the copolymer/electrolyte periodic structure, three to five times higher than the prevalent PEO-LiTFSI solid electrolyte or its hybrid with inorganic nasicon solid electrolyte. In addition, the composite electrolyte possesses significant high extensibility which can be stretched to 220% before rupture, ensuring excellent flexible capability. This high flexibility and nice compatibility with modern manufacturing technologies prove high application potential for future microelectronics. This scalable strategy and the unique design methodology can also be applied to other inorganic brittle membrane to improve the flexibility.

9.2 Future work strategy

Although the research in this dissertation has improved our understanding in materials properties through high temperature process techniques, there are still some interesting questions that could become the core of future research.

PGM-free catalysts for ORR

Although the PGM-free catalyst present good performance and durability in ORR for fuel cell, there is still a challenge that the incomplete reduction of O_2 would result in formation of H_2O_2. The formation of destructive H_2O_2 not only decreases the activity and stability of PGM-free catalysts (H_2O_2 has been shown to degrade PGM-free ORR), but also damages the membrane and ionomers in the catalyst layer.

We propose further study of the approaches that could suppress the formation of H_2O_2, such as introducing another catalyst functioning as the H_2O_2 scavenger. Thermal shock technique can also be applied in the synthesis of this scavengers. We propose to use thermal shock approach to develop well-dispersed Group IV and V metal oxide/oxynitride nanoparticles, with increased oxygen vacancies and decreased dimensions of less than 10 nm, as highly active and durable catalysts for H_2O_2/radical removal. These nanoparticles will be homogenously assembled onto high surface area carbon substrates or directly on PGM-free catalysts to remove H_2O_2/radicals during the oxygen reduction reaction (ORR).

The H_2O_2/radical removal activity of oxides, such as CeO_x, ZrO_x, and Ta_xTiO_y, is attributed to the existence of oxygen vacancies. The number of active sites will be enhanced by using nitrogen precursors with more free N-content and achieving a high pyridinic N-doping level. We will use heat treatment under an oxygen deficient

environment, as well as under NH_3 atmosphere for nitrogen doping, to elevate the number and stability of the oxygen vacancies.

Garnet solid-state electrolyte for Lithium batteries

Although in this dissertation, two different approaches are introduced to improve the flexibility of the solid-state electrolyte, there are still a number of remaining questions related to specific issues of the electrolyte. The morphology evaluation of electrolyte with lithium anode can be characterized with FIB/SEM. Furthermore, compositional or interfacial modifications could be adopted to improve the cycle capability at higher current density. Cathodes materials should be modified to decrease the interfacial impedance with the solid-state electrolyte. For example, ball milling can be employed to decrease the dimensions of the cathode materials which could be better deposited on the solid-state electrolyte. Moreover, porous structure design of the soli-state electrolyte could also be carried out to improve the effective contact surface area with electrode active materials. Additionally, high specific capacity electrode materials (for instance, Li/S) could be combined to the solid-state electrolyte to elevate the energy density of the full battery cell.

Bibliography

(1) Xu, R.; Xu, Y. *Modern Inorganic Synthetic Chemistry*; Elsevier, 2010.

(2) German, R. M. Sintering Theory and Practice. *Solar-Terrestrial Phys.* **1996**, 568.

(3) Larcher, D.; Tarascon, J. M. Towards Greener and More Sustainable Batteries for Electrical Energy Storage. *Nat. Chem.* **2015**, *7* (1), 19–29.

(4) Chu, S.; Majumdar, A. Opportunities and Challenges for a Sustainable Energy Future. *Nature* **2012**, *488* (7411), 294–303.

(5) Shao, M.; Chang, Q.; Dodelet, J.-P.; Chenitz, R. Recent Advances in Electrocatalysts for Oxygen Reduction Reaction. *Chem. Rev.* **2016**, *116* (6), 3594–3657.

(6) Kraytsberg, A.; Ein-Eli, Y. Review of Advanced Materials for Proton Exchange Membrane Fuel Cells. *Energy and Fuels* **2014**, *28* (12), 7303–7330.

(7) Chung, D. Y.; Jun, S. W.; Yoon, G.; Kwon, S. G.; Shin, D. Y.; Seo, P.; Yoo, J. M.; Shin, H.; Chung, Y. H.; Kim, H.; et al. Highly Durable and Active PtFe Nanocatalyst for Electrochemical Oxygen Reduction Reaction. *J. Am. Chem. Soc.* **2015**, *137* (49), 15478–15485.

(8) Hata, H.; Kubo, S.; Kobayashi, Y.; Mallouk, T. E. Intercalation of Well-Dispersed Gold Nanoparticles into Layered Oxide Nanosheets through Intercalation of a Polyamine. *J. Am. Chem. Soc.* **2007**, *129* (11), 3064–3065.

(9) Duchesne, P. N.; Li, Z. Y.; Deming, C. P.; Fung, V.; Zhao, X.; Yuan, J.; Regier, T.; Aldalbahi, A.; Almarhoon, Z.; Chen, S.; et al. Golden Single-Atomic-Site Platinum Electrocatalysts. *Nat. Mater.* **2018**, *17* (November).

(10) Strayer, M. E.; Binz, J. M.; Tanase, M.; Kamali Shahri, S. M.; Sharma, R.; Rioux, R. M.; Mallouk, T. E. Interfacial Bonding Stabilizes Rhodium and Rhodium Oxide Nanoparticles on Layered Nb Oxide and Ta Oxide Supports. *J. Am. Chem. Soc.* **2014**, *136* (15), 5687–5696.

(11) Sun, Y.; Zhang, X.; Luo, M.; Chen, X.; Wang, L.; Li, Y.; Li, M.; Qin, Y.; Li, C.; Xu, N.; et al. Ultrathin PtPd-Based Nanorings with Abundant Step Atoms Enhance Oxygen Catalysis. *Adv. Mater.* **2018**, *30* (38), 1–8.

(12) Guo, S.; Zhang, S.; Wu, L.; Sun, S. Co/CoO Nanoparticles Assembled on Graphene for Electrochemical Reduction of Oxygen. *Angew. chemie Int. Ed.* **2012**, *51* (47), 11770–11773.

(13) Kim, D.; Becknell, N.; Yu, Y.; Yang, P. Room-Temperature Dynamics of Vanishing Copper Nanoparticles Supported on Silica. *Nano Lett.* **2017**, *17* (4), 2732–2737.

(14) Du, L.; Luo, L.; Feng, Z.; Engelhard, M.; Xie, X.; Han, B.; Sun, J.; Zhang, J.; Yin, G.; Wang, C. Nitrogen–doped Graphitized Carbon Shell Encapsulated NiFe Nanoparticles: A Highly Durable Oxygen Evolution Catalyst. *Nano*

Energy **2017**, *39*, 245–252.

(15) Zhang, Z.; Sun, J.; Wang, F.; Dai, L. Efficient Oxygen Reduction Reaction (ORR) Catalysts Based on Single Iron Atoms Dispersed on a Hierarchically Structured Porous Carbon Framework. *Angew. Chemie Int. Ed.* **2018**, *57* (29), 9038–9043.

(16) Cheng, Q.; Han, S.; Mao, K.; Chen, C.; Yang, L.; Zou, Z.; Gu, M.; Hu, Z.; Yang, H. Co Nanoparticle Embedded in Atomically-Dispersed Co-NC Nanofibers for Oxygen Reduction with High Activity and Remarkable Durability. *Nano energy* **2018**, *52*, 485–493.

(17) Li, Z.; Zhuang, Z.; Lv, F.; Zhu, H.; Zhou, L.; Luo, M.; Zhu, J.; Lang, Z.; Feng, S.; Chen, W. The Marriage of the FeN4 Moiety and MXene Boosts Oxygen Reduction Catalysis: Fe 3d Electron Delocalization Matters. *Adv. Mater.* **2018**, *30* (43), 1803220.

(18) Prieto, G.; Zečević, J.; Friedrich, H.; De Jong, K. P.; De Jongh, P. E. Towards Stable Catalysts by Controlling Collective Properties of Supported Metal Nanoparticles. *Nat. Mater.* **2013**, *12* (1), 34.

(19) Hao, R.; Xing, R.; Xu, Z.; Hou, Y.; Gao, S.; Sun, S. Synthesis, Functionalization, and Biomedical Applications of Multifunctional Magnetic Nanoparticles. *Adv. Mater.* **2010**, *22* (25), 2729–2742.

(20) Peterson, S. B.; Apt, J.; Whitacre, J. F. Lithium-Ion Battery Cell Degradation Resulting from Realistic Vehicle and Vehicle-to-Grid Utilization. *J. Power Sources* **2010**, *195* (8), 2385–2392.

(21) Goodenough, J. B.; Kim, Y. Challenges for Rechargeable Li Batteries. *Chem. Mater.* **2009**, *22* (3), 587–603.

(22) Armand, M.; Tarascon, J.-M. Building Better Batteries. *Nature* **2008**, *451* (7179), 652.

(23) Gerssen-Gondelach, S. J.; Faaij, A. P. C. Performance of Batteries for Electric Vehicles on Short and Longer Term. *J. Power Sources* **2012**, *212*, 111–129.

(24) Han, X.; Ouyang, M.; Lu, L.; Li, J. A Comparative Study of Commercial Lithium Ion Battery Cycle Life in Electric Vehicle: Capacity Loss Estimation. *J. Power Sources* **2014**, *268*, 658–669.

(25) Tran, M.; Banister, D.; Bishop, J. D. K.; McCulloch, M. D. Realizing the Electric-Vehicle Revolution. *Nat. Clim. Chang.* **2012**, *2* (5), 328.

(26) Dunn, B.; Kamath, H.; Tarascon, J.-M. Electrical Energy Storage for the Grid: A Battery of Choices. *Science (80-.).* **2011**, *334* (6058), 928–935.

(27) Willgert, M.; Leijonmarck, S.; Lindbergh, G.; Malmström, E.; Johansson, Mjj. Cellulose Nanofibril Reinforced Composite Electrolytes for Lithium Ion Battery Applications. *J. Mater. Chem. A* **2014**, *2* (33), 13556–13564.

(28) Zhu, Y.; Xiao, S.; Shi, Y.; Yang, Y.; Hou, Y.; Wu, Y. A Composite Gel Polymer Electrolyte with High Performance Based on Poly (Vinylidene Fluoride) and Polyborate for Lithium Ion Batteries. *Adv. Energy Mater.* **2014**,

4 (1), 1300647.

(29) Zhu, Y.; Wang, F.; Liu, L.; Xiao, S.; Chang, Z.; Wu, Y. Composite of a Nonwoven Fabric with Poly (Vinylidene Fluoride) as a Gel Membrane of High Safety for Lithium Ion Battery. *Energy Environ. Sci.* **2013**, *6* (2), 618–624.

(30) Xiao, S.; Wang, F.; Yang, Y.; Chang, Z.; Wu, Y. An Environmentally Friendly and Economic Membrane Based on Cellulose as a Gel Polymer Electrolyte for Lithium Ion Batteries. *Rsc Adv.* **2014**, *4* (1), 76–81.

(31) Stephan, A. M.; Nahm, K. S. Review on Composite Polymer Electrolytes for Lithium Batteries. *Polymer (Guildf).* **2006**, *47* (16), 5952–5964.

(32) Quartarone, E.; Mustarelli, P. Electrolytes for Solid-State Lithium Rechargeable Batteries: Recent Advances and Perspectives. *Chem. Soc. Rev.* **2011**, *40* (5), 2525–2540.

(33) Takada, K. Progress and Prospective of Solid-State Lithium Batteries. *Acta Mater.* **2013**, *61* (3), 759–770.

(34) Seino, Y.; Ota, T.; Takada, K.; Hayashi, A.; Tatsumisago, M. A Sulphide Lithium Super Ion Conductor Is Superior to Liquid Ion Conductors for Use in Rechargeable Batteries. *Energy Environ. Sci.* **2014**, *7* (2), 627–631.

(35) Liu, Z.; Fu, W.; Payzant, E. A.; Yu, X.; Wu, Z.; Dudney, N. J.; Kiggans, J.; Hong, K.; Rondinone, A. J.; Liang, C. Anomalous High Ionic Conductivity of Nanoporous β-Li3PS4. *J. Am. Chem. Soc.* **2013**, *135* (3), 975–978.

(36) Wang, A.; Xu, H.; Zhou, Q.; Liu, X.; Li, Z.; Gao, R.; Wu, N.; Guo, Y.; Li, H.; Zhang, L. A New All-Solid-State Hyperbranched Star Polymer Electrolyte for Lithium Ion Batteries: Synthesis and Electrochemical Properties. *Electrochim. Acta* **2016**, *212*, 372–379.

(37) Zhang, J.; Zhao, J.; Yue, L.; Wang, Q.; Chai, J.; Liu, Z.; Zhou, X.; Li, H.; Guo, Y.; Cui, G. Safety-reinforced Poly (Propylene Carbonate)-based All-solid-state Polymer Electrolyte for Ambient-temperature Solid Polymer Lithium Batteries. *Adv. Energy Mater.* **2015**, *5* (24), 1501082.

(38) Xin, S.; You, Y.; Wang, S.; Gao, H.-C.; Yin, Y.-X.; Guo, Y.-G. Solid-State Lithium Metal Batteries Promoted by Nanotechnology: Progress and Prospects. *ACS Energy Lett.* **2017**, *2* (6), 1385–1394.

(39) Cheng, X.-B.; Zhang, R.; Zhao, C.-Z.; Zhang, Q. Toward Safe Lithium Metal Anode in Rechargeable Batteries: A Review. *Chem. Rev.* **2017**, *117* (15), 10403–10473.

(40) Xu, K. Electrolytes and Interphases in Li-Ion Batteries and Beyond. *Chem. Rev.* **2014**, *114* (23), 11503–11618.

(41) Xu, W.; Wang, J.; Ding, F.; Chen, X.; Nasybulin, E.; Zhang, Y.; Zhang, J.-G. Lithium Metal Anodes for Rechargeable Batteries. *Energy Environ. Sci.* **2014**, *7* (2), 513–537.

(42) Arico, A. S.; Bruce, P.; Scrosati, B.; Tarascon, J.-M.; Van Schalkwijk, W. Nanostructured Materials for Advanced Energy Conversion and Storage

Devices. In *Materials For Sustainable Energy: A Collection of Peer-Reviewed Research and Review Articles from Nature Publishing Group*; World Scientific, 2011; pp 148–159.

(43) Qian, X.; Gu, N.; Cheng, Z.; Yang, X.; Wang, E.; Dong, S. Impedance Study of (PEO) 10LiClO4–Al2O3 Composite Polymer Electrolyte with Blocking Electrodes. *Electrochim. Acta* **2001**, *46* (12), 1829–1836.

(44) Kim, J.-W.; Ji, K.-S.; Lee, J.-P.; Park, J.-W. Electrochemical Characteristics of Two Types of PEO-Based Composite Electrolyte with Functional SiO2. *J. Power Sources* **2003**, *119*, 415–421.

(45) Murugan, R.; Thangadurai, V.; Weppner, W. Fast Lithium Ion Conduction in Garnet-type Li7La3Zr2O12. *Angew. Chemie Int. Ed.* **2007**, *46* (41), 7778–7781.

(46) Kazyak, E.; Chen, K. H.; Wood, K. N.; Davis, A. L.; Thompson, T.; Bielinski, A. R.; Sanchez, A. J.; Wang, X.; Wang, C.; Sakamoto, J.; et al. Atomic Layer Deposition of the Solid Electrolyte Garnet Li7La3Zr2O12. *Chem. Mater.* **2017**, *29* (8), 3785–3792.

(47) van den Broek, J.; Afyon, S.; Rupp, J. L. M. Interface-Engineered All-Solid-State Li-Ion Batteries Based on Garnet-Type Fast Li+Conductors. *Adv. Energy Mater.* **2016**, *6* (19), 1–11.

(48) Wang, Y.; Richards, W. D.; Ong, S. P.; Miara, L. J.; Kim, J. C.; Mo, Y.; Ceder, G. Design Principles for Solid-State Lithium Superionic Conductors. *Nat. Mater.* **2015**, *14* (10), 1026.

(49) Ren, J.; Li, L.; Chen, C.; Chen, X.; Cai, Z.; Qiu, L.; Wang, Y.; Zhu, X.; Peng, H. Twisting Carbon Nanotube Fibers for Both Wire-shaped Micro-supercapacitor and Micro-battery. *Adv. Mater.* **2013**, *25* (8), 1155–1159.

(50) Li, Z.; Xu, Z.; Tan, X.; Wang, H.; Holt, C. M. B.; Stephenson, T.; Olsen, B. C.; Mitlin, D. Mesoporous Nitrogen-Rich Carbons Derived from Protein for Ultra-High Capacity Battery Anodes and Supercapacitors. *Energy Environ. Sci.* **2013**, *6* (3), 871–878.

(51) Ji, X.; Lee, K. T.; Nazar, L. F. A Highly Ordered Nanostructured Carbon–sulphur Cathode for Lithium–sulphur Batteries. *Nat. Mater.* **2009**, *8* (6), 500.

(52) Ren, L.; Pint, C. L.; Arikawa, T.; Takeya, K.; Kawayama, I.; Tonouchi, M.; Hauge, R. H.; Kono, J. Broadband Terahertz Polarizers with Ideal Performance Based on Aligned Carbon Nanotube Stacks. *Nano Lett.* **2012**, *12* (2), 787–790.

(53) Ji, L.; Lin, Z.; Alcoutlabi, M.; Zhang, X. Recent Developments in Nanostructured Anode Materials for Rechargeable Lithium-Ion Batteries. *Energy Environ. Sci.* **2011**, *4* (8), 2682–2699.

(54) Van de Vyver, S.; Peng, L.; Geboers, J.; Schepers, H.; de Clippel, F.; Gommes, C. J.; Goderis, B.; Jacobs, P. A.; Sels, B. F. Sulfonated Silica/Carbon Nanocomposites as Novel Catalysts for Hydrolysis of Cellulose to Glucose. *Green Chem.* **2010**, *12* (9), 1560–1563.

(55) Guan, B.; Wang, X.; Xiao, Y.; Liu, Y.; Huo, Q. A Versatile Cooperative Template-Directed Coating Method to Construct Uniform Microporous Carbon Shells for Multifunctional Core–shell Nanocomposites. *Nanoscale* **2013**, *5* (6), 2469–2475.

(56) Guo, J.; Liu, Q.; Wang, C.; Zachariah, M. R. Interdispersed Amorphous MnOx–carbon Nanocomposites with Superior Electrochemical Performance as Lithium-storage Material. *Adv. Funct. Mater.* **2012**, *22* (4), 803–811.

(57) Wang, Y.; Zhang, H. J.; Lu, L.; Stubbs, L. P.; Wong, C. C.; Lin, J. Designed Functional Systems from Peapod-like Co@ Carbon to Co3O4@ Carbon Nanocomposites. *ACS Nano* **2010**, *4* (8), 4753–4761.

(58) Zhu, M.; Diao, G. Review on the Progress in Synthesis and Application of Magnetic Carbon Nanocomposites. *Nanoscale* **2011**, *3* (7), 2748–2767.

(59) Ji, X.; Liu, D.-Y.; Prendiville, D. G.; Zhang, Y.; Liu, X.; Stucky, G. D. Spatially Heterogeneous Carbon-Fiber Papers as Surface Dendrite-Free Current Collectors for Lithium Deposition. *Nano Today* **2012**, *7* (1), 10–20.

(60) Yamada, O.; Miyamoto, Y.; Koizumi, M. Self-Propagating High-Temperature Synthesis of the SiC. *J. Mater. Res.* **1986**, *1* (2), 275–279.

(61) Lu, D.; Yang, Y.; Qin, Y.; Yang, G. Forming Microgears by Micro-Fast Technology. *J. Microelectromechanical Syst.* **2013**, *22* (3), 708–715.

(62) Kim, K. J.; Lee, S.; Lee, J. H.; Roh, M.; Lim, K.; Kim, Y. Structural and Optical Characteristics of Crystalline Silicon Carbide Nanoparticles Synthesized by Carbothermal Reduction. *J. Am. Ceram. Soc.* **2009**, *92* (2), 424–428.

(63) Shi, W.; Zheng, Y.; Peng, H.; Wang, N.; Lee, C. S.; Lee, S. Laser Ablation Synthesis and Optical Characterization of Silicon Carbide Nanowires. *J. Am. Ceram. Soc.* **2000**, *83* (12), 3228–3230.

(64) Rossi, A. M.; Murphy, T. E.; Reipa, V. Ultraviolet Photoluminescence from 6 H Silicon Carbide Nanoparticles. *Appl. Phys. Lett.* **2008**, *92* (25), 253112.

(65) Wasyluk, J.; Perova, T. S.; Kukushkin, S. A.; Osipov, A. V; Feoktistov, N. A.; Grudinkin, S. A. Raman Investigation of Different Polytypes in SiC Thin Films Grown by Solid-Gas Phase Epitaxy on Si (111) and 6H-SiC Substrates. In *Materials Science Forum*; Trans Tech Publ, 2010; Vol. 645, pp 359–362.

(66) Feng, X. L.; Matheny, M. H.; Zorman, C. A.; Mehregany, M.; Roukes, M. L. Low Voltage Nanoelectromechanical Switches Based on Silicon Carbide Nanowires. *Nano Lett.* **2010**, *10* (8), 2891–2896.

(67) Wu, L.; Pei, F.; Mao, R.; Wu, F.; Wu, Y.; Qian, J.; Cao, Y.; Ai, X.; Yang, H. SiC–Sb–C Nanocomposites as High-Capacity and Cycling-Stable Anode for Sodium-Ion Batteries. *Electrochim. Acta* **2013**, *87*, 41–45.

(68) Yan-Hui, C.; Qian-Gang, F.; Cui-Wei, C.; He-Jun, L.; Ke-Zhi, L.; Qin, L. SiC Nanowire-Toughened SiC–MoSi2–CrSi2 Oxidation Protective Coating for Carbon/Carbon Composites. *Surf. Coatings Technol.* **2010**, *205* (2), 413–418.

(69) Yu, H.; Zhou, X.; Zhang, W.; Peng, H.; Zhang, C.; Sun, K. Properties of Carbon Nano-Tubes–Cf/SiC Composite by Precursor Infiltration and Pyrolysis Process. *Mater. Des.* **2011**, *32* (6), 3516–3520.

(70) Shimoda, K.; Hinoki, T.; Kohyama, A. Effect of Carbon Nanofibers (CNFs) Content on Thermal and Mechanical Properties of CNFs/SiC Nanocomposites. *Compos. Sci. Technol.* **2010**, *70* (2), 387–392.

(71) Qiang, X.; Li, H.; Zhang, Y.; Wang, Z.; Ba, Z. Synthesis and Toughening Effect of SiC Nanowires Wrapped by Carbon Nanosheet on C/C Composites. *J. Alloys Compd.* **2016**, *676*, 245–250.

(72) Yuan, J.-K.; Li, W.-L.; Yao, S.-H.; Lin, Y.-Q.; Sylvestre, A.; Bai, J. High Dielectric Permittivity and Low Percolation Threshold in Polymer Composites Based on SiC-Carbon Nanotubes Micro/Nano Hybrid. *Appl. Phys. Lett.* **2011**, *98* (3), 32901.

(73) Zhou, T.; Wang, X.; Liu, X.; Xiong, D. Improved Thermal Conductivity of Epoxy Composites Using a Hybrid Multi-Walled Carbon Nanotube/Micro-SiC Filler. *Carbon N. Y.* **2010**, *48* (4), 1171–1176.

(74) Mzyk, A.; Major, R.; Lackner, J. M.; Bruckert, F.; Wilczek, P.; Major, B. Effect of the Silicon Carbide Nanoparticles Introduction on Biological Properties of Porous Polymer Coatings. *RSC Adv.* **2015**, *5* (18), 13906–13916.

(75) Chen, Y.; Fu, K.; Zhu, S.; Luo, W.; Wang, Y.; Li, Y.; Hitz, E.; Yao, Y.; Dai, J.; Wan, J. Reduced Graphene Oxide Films with Ultrahigh Conductivity as Li-Ion Battery Current Collectors. *Nano Lett.* **2016**, *16* (6), 3616–3623.

(76) Yao, Y.; Fu, K. K.; Yan, C.; Dai, J.; Chen, Y.; Wang, Y.; Zhang, B.; Hitz, E.; Hu, L. Three-Dimensional Printable High-Temperature and High-Rate Heaters. *ACS Nano* **2016**, *10* (5), 5272–5279.

(77) Yao, Y.; Fu, K. K.; Zhu, S.; Dai, J.; Wang, Y.; Pastel, G.; Chen, Y.; Li, T.; Wang, C.; Li, T. Carbon Welding by Ultrafast Joule Heating. *Nano Lett.* **2016**, *16* (11), 7282–7289.

(78) Deng, Z.; Tian, Y.; Lee, S.; Ribbe, A. E.; Mao, C. DNA-encoded Self-assembly of Gold Nanoparticles into One-dimensional Arrays. *Angew. Chemie Int. Ed.* **2005**, *44* (23), 3582–3585.

(79) Bruce, P. G.; Scrosati, B.; Tarascon, J. Nanomaterials for Rechargeable Lithium Batteries. *Angew. Chemie Int. Ed.* **2008**, *47* (16), 2930–2946.

(80) Lai, H.; Shang, L.; Wu, Q.; Yang, L.; Zhao, J.; Li, H.; Lyu, Z.; Wang, X.; Hu, Z. Spinel Nickel Cobaltite Mesostructures Assembled from Ultrathin Nanosheets for High-Performance Electrochemical Energy Storage. *ACS Appl. Energy Mater.* **2018**, *1* (2), 684–691.

(81) Huang, L.; Santiago, D.; Loyselle, P.; Dai, L. Graphene-Based Nanomaterials for Flexible and Wearable Supercapacitors. *Small* **2018**, *14* (43), 1800879.

(82) Weng, Z.; Wu, Y.; Wang, M.; Jiang, J.; Yang, K.; Huo, S.; Wang, X.-F.; Ma, Q.; Brudvig, G. W.; Batista, V. S. Active Sites of Copper-Complex Catalytic

Materials for Electrochemical Carbon Dioxide Reduction. *Nat. Commun.* **2018**, *9* (1), 415.

(83) Liu, P.; Zhao, Y.; Qin, R.; Mo, S.; Chen, G.; Gu, L.; Chevrier, D. M.; Zhang, P.; Guo, Q.; Zang, D. Photochemical Route for Synthesizing Atomically Dispersed Palladium Catalysts. *Science (80-.).* **2016**, *352* (6287), 797–800.

(84) Luo, L.; Engelhard, M. H.; Shao, Y.; Wang, C. Revealing the Dynamics of Platinum Nanoparticle Catalysts on Carbon in Oxygen and Water Using Environmental TEM. *ACS Catal.* **2017**, *7* (11), 7658–7664.

(85) Ge, X.; Du, Y.; Li, B.; Hor, T. S. A.; Sindoro, M.; Zong, Y.; Zhang, H.; Liu, Z. Intrinsically Conductive Perovskite Oxides with Enhanced Stability and Electrocatalytic Activity for Oxygen Reduction Reactions. *ACS Catal.* **2016**, *6* (11), 7865–7871.

(86) Strayer, M. E.; Binz, J. M.; Tanase, M.; Kamali Shahri, S. M.; Sharma, R.; Rioux, R. M.; Mallouk, T. E. Interfacial Bonding Stabilizes Rhodium and Rhodium Oxide Nanoparticles on Layered Nb Oxide and Ta Oxide Supports. *J. Am. Chem. Soc.* **2014**, *136* (15), 5687–5696.

(87) Duchesne, P. N.; Li, Z. Y.; Deming, C. P.; Fung, V.; Zhao, X.; Yuan, J.; Regier, T.; Aldalbahi, A.; Almarhoon, Z.; Chen, S. Golden Single-Atomic-Site Platinum Electrocatalysts. *Nat. Mater.* **2018**, *17* (11), 1033.

(88) Sun, Y.; Zhang, X.; Luo, M.; Chen, X.; Wang, L.; Li, Y.; Li, M.; Qin, Y.; Li, C.; Xu, N. Ultrathin PtPd-Based Nanorings with Abundant Step Atoms Enhance Oxygen Catalysis. *Adv. Mater.* **2018**, *30* (38), 1802136.

(89) Zhang, Z.; Liu, G.; Cui, X.; Chen, B.; Zhu, Y.; Gong, Y.; Saleem, F.; Xi, S.; Du, Y.; Borgna, A. Crystal Phase and Architecture Engineering of Lotus-Thalamus-Shaped Pt-Ni Anisotropic Superstructures for Highly Efficient Electrochemical Hydrogen Evolution. *Adv. Mater.* **2018**, *30* (30), 1801741.

(90) Chung, D. Y.; Jun, S. W.; Yoon, G.; Kwon, S. G.; Shin, D. Y.; Seo, P.; Yoo, J. M.; Shin, H.; Chung, Y.-H.; Kim, H. Highly Durable and Active PtFe Nanocatalyst for Electrochemical Oxygen Reduction Reaction. *J. Am. Chem. Soc.* **2015**, *137* (49), 15478–15485.

(91) Hata, H.; Kubo, S.; Kobayashi, Y.; Mallouk, T. E. Intercalation of Well-Dispersed Gold Nanoparticles into Layered Oxide Nanosheets through Intercalation of a Polyamine. *J. Am. Chem. Soc.* **2007**, *129* (11), 3064–3065.

(92) Cheng, Q.; Han, S.; Mao, K.; Chen, C.; Yang, L.; Zou, Z.; Gu, M.; Hu, Z.; Yang, H. Co Nanoparticle Embedded in Atomically-Dispersed Co-N-C Nanofibers for Oxygen Reduction with High Activity and Remarkable Durability. *Nano Energy* **2018**, *52* (July), 485–493.

(93) Du, L.; Luo, L.; Feng, Z.; Engelhard, M.; Xie, X.; Han, B.; Sun, J.; Zhang, J.; Yin, G.; Wang, C.; et al. Nitrogen–doped Graphitized Carbon Shell Encapsulated NiFe Nanoparticles: A Highly Durable Oxygen Evolution Catalyst. *Nano Energy* **2017**, *39* (July), 245–252.

(94) Guo, S.; Zhang, S.; Wu, L.; Sun, S. Co/CoO Nanoparticles Assembled on

Graphene for Electrochemical Reduction of Oxygen. *Angew. Chemie - Int. Ed.* **2012**, *51* (47), 11770–11773.

(95) Ago, H.; Ito, Y.; Mizuta, N.; Yoshida, K.; Hu, B.; Orofeo, C. M.; Tsuji, M.; Ikeda, K.; Mizuno, S. Epitaxial Chemical Vapor Deposition Growth of Single-Layer Graphene over Cobalt Film Crystallized on Sapphire. *ACS Nano* **2010**, *4* (12), 7407–7414.

(96) Bhaviripudi, S.; Jia, X.; Dresselhaus, M. S.; Kong, J. Role of Kinetic Factors in Chemical Vapor Deposition Synthesis of Uniform Large Area Graphene Using Copper Catalyst. *Nano Lett.* **2010**, *10* (10), 4128–4133.

(97) Kim, M.; Nam, D.-H.; Park, H.-Y.; Kwon, C.; Eom, K.; Yoo, S.; Jang, J.; Kim, H.-J.; Cho, E.; Kwon, H. Cobalt-Carbon Nanofibers as an Efficient Support-Free Catalyst for Oxygen Reduction Reaction with a Systematic Study of Active Site Formation. *J. Mater. Chem. A* **2015**, *3* (27), 14284–14290.

(98) Jiang, S.; Zhu, C.; Dong, S. Cobalt and Nitrogen-Cofunctionalized Graphene as a Durable Non-Precious Metal Catalyst with Enhanced ORR Activity. *J. Mater. Chem. A* **2013**, *1* (11), 3593–3599.

(99) Doan-Nguyen, V. V. T.; Zhang, S.; Trigg, E. B.; Agarwal, R.; Li, J.; Su, D.; Winey, K. I.; Murray, C. B. Synthesis and X-Ray Characterization of Cobalt Phosphide (Co2P) Nanorods for the Oxygen Reduction Reaction. *ACS Nano* **2015**, *9* (8), 8108–8115.

(100) Hu, Y.; Jensen, J. O.; Zhang, W.; Cleemann, L. N.; Xing, W.; Bjerrum, N. J.; Li, Q. Hollow Spheres of Iron Carbide Nanoparticles Encased in Graphitic Layers as Oxygen Reduction Catalysts. *Angew. Chemie Int. Ed.* **2014**, *53* (14), 3675–3679.

(101) Deng, J.; Ren, P.; Deng, D.; Bao, X. Enhanced Electron Penetration through an Ultrathin Graphene Layer for Highly Efficient Catalysis of the Hydrogen Evolution Reaction. *Angew. Chemie Int. Ed.* **2015**, *54* (7), 2100–2104.

(102) Deng, J.; Deng, D.; Bao, X. Robust Catalysis on 2D Materials Encapsulating Metals: Concept, Application, and Perspective. *Adv. Mater.* **2017**, *29* (43), 1–23.

(103) Olson, T. S.; Pylypenko, S.; Atanassov, P.; Asazawa, K.; Yamada, K.; Tanaka, H. Anion-Exchange Membrane Fuel Cells: Dual-Site Mechanism of Oxygen Reduction Reaction in Alkaline Media on Cobalt− Polypyrrole Electrocatalysts. *J. Phys. Chem. C* **2010**, *114* (11), 5049–5059.

(104) Wang, X. X.; Cullen, D. A.; Pan, Y.-T.; Hwang, S.; Wang, M.; Feng, Z.; Wang, J.; Engelhard, M. H.; Zhang, H.; He, Y.; et al. Nitrogen-Coordinated Single Cobalt Atom Catalysts for Oxygen Reduction in Proton Exchange Membrane Fuel Cells. *Adv. Mater.* **2018**, *1706758*, 1706758.

(105) Huang, X.; Zhao, Z.; Cao, L.; Chen, Y.; Zhu, E.; Lin, Z.; Li, M.; Yan, A.; Zettl, A.; Wang, Y. M.; et al. High-Performance Transition Metal – Doped Pt3Ni Octahedra for Oxygen Reduction Reaction. *Science (80-.).* **2015**, *348* (2009), 1230–1234.

(106) Kitchin, J. R.; Bligaard, T. Origin of the Overpotential for Oxygen Reduction at a Fuel-Cell Cathode. **2004**, No. August 2017.

(107) Bao, Y.; An, W.; Turner, C. H.; Krishnan, K. M. The Critical Role of Surfactants in the Growth of Cobalt Nanoparticles. *Langmuir* **2009**, *26* (1), 478–483.

(108) Hohenberg, P.; Kohn, W. Inhomogeneous Electron Gas Physical Review 136. *B864* **1964**.

(109) Kohn, W.; Sham, L. J. Self-Consistent Equations Including Exchange and Correlation Effects. *Phys. Rev.* **1965**, *140* (4A), A1133.

(110) Kresse, G.; Furthmüller, J. Efficiency of Ab-Initio Total Energy Calculations for Metals and Semiconductors Using a Plane-Wave Basis Set. *Comput. Mater. Sci.* **1996**, *6* (1), 15–50.

(111) Kresse, G.; Joubert, D. From Ultrasoft Pseudopotentials to the Projector Augmented-Wave Method. *Phys. Rev. B* **1999**, *59* (3), 1758.

(112) Blöchl, P. E. Projector Augmented-Wave Method. *Phys. Rev. B* **1994**, *50* (24), 17953.

(113) Perdew, J. P. K. Burke, m. Ernzerhof. *Phys. Rev. Lett* **1996**, *77*, 3865.

(114) Monkhorst, H. J.; Pack, J. D. Special Points for Brillouin-Zone Integrations. *Phys. Rev. B* **1976**, *13* (12), 5188.

(115) Lin, D.; Zhao, J.; Sun, J.; Yao, H.; Liu, Y.; Yan, K.; Cui, Y. Three-Dimensional Stable Lithium Metal Anode with Nanoscale Lithium Islands Embedded in Ionically Conductive Solid Matrix. *Proc. Natl. Acad. Sci.* **2017**, *114* (42), 4613–4618.

(116) Yang, C.-P.; Yin, Y.-X.; Zhang, S.-F.; Li, N.-W.; Guo, Y.-G. Accommodating Lithium into 3D Current Collectors with a Submicron Skeleton towards Long-Life Lithium Metal Anodes. *Nat. Commun.* **2015**, *6* (May), 8058.

(117) Lin, D.; Liu, Y.; Liang, Z.; Lee, H. W.; Sun, J.; Wang, H.; Yan, K.; Xie, J.; Cui, Y. Layered Reduced Graphene Oxide with Nanoscale Interlayer Gaps as a Stable Host for Lithium Metal Anodes. *Nat. Nanotechnol.* **2016**, *11* (7), 626–632.

(118) Liang, Z.; Lin, D.; Zhao, J.; Lu, Z.; Liu, Y.; Liu, C.; Lu, Y.; Wang, H.; Yan, K.; Tao, X.; et al. Composite Lithium Metal Anode by Melt Infusion of Lithium into a 3D Conducting Scaffold with Lithiophilic Coating. *Proc. Natl. Acad. Sci.* **2016**, 201518188.

(119) Ni, J. E.; Case, E. D.; Sakamoto, J. S.; Rangasamy, E.; Wolfenstine, J. B. Room Temperature Elastic Moduli and Vickers Hardness of Hot-Pressed LLZO Cubic Garnet. *J. Mater. Sci.* **2012**, *47* (23), 7978–7985.

(120) Monroe, C.; Newman, J. The Impact of Elastic Deformation on Deposition Kinetics at Lithium/Polymer Interfaces. *J. Electrochem. Soc.* **2005**, *152* (2), A396.

(121) Yu, X. A Stable Thin-Film Lithium Electrolyte: Lithium Phosphorus

Oxynitride. *J. Electrochem. Soc.* **1997**, *144* (2), 524.

(122) Senevirathne, K.; Day, C. S.; Gross, M. D.; Lachgar, A.; Holzwarth, N. A. W. A New Crystalline LiPON Electrolyte: Synthesis, Properties, and Electronic Structure. *Solid State Ionics* **2013**, *233*, 95–101.

(123) Kamaya, N.; Homma, K.; Yamakawa, Y.; Hirayama, M.; Kanno, R.; Yonemura, M.; Kamiyama, T.; Kato, Y.; Hama, S.; Kawamoto, K.; et al. A Lithium Superionic Conductor. *Nat. Mater.* **2011**, *10* (9), 682–686.

(124) Kato, Y.; Hori, S.; Saito, T.; Suzuki, K.; Hirayama, M.; Mitsui, A.; Yonemura, M.; Iba, H.; Kanno, R. High-Power All-Solid-State Batteries Using Sulfide Superionic Conductors. *Nat. Energy* **2016**, *1* (March), 16030.

(125) Kosova, N. V.; Devyatkina, E. T.; Stepanov, A. P.; Buzlukov, A. L. Lithium Conductivity and Lithium Diffusion in NASICON-Type Li 1+xTi2-XAlx(PO4)3 (X=0; 0.3) Prepared by Mechanical Activation. *Ionics (Kiel).* **2008**, *14* (4), 303–311.

(126) Hartmann, P.; Leichtweiss, T.; Busche, M. R.; Schneider, M.; Reich, M.; Sann, J.; Adelhelm, P.; Janek, J. Degradation of NASICON-Type Materials in Contact with Lithium Metal: Formation of Mixed Conducting Interphases (MCI) on Solid Electrolytes. *J. Phys. Chem. C* **2013**, No. 117, 21064–21074.

(127) Liu, W.; Liu, N.; Sun, J.; Hsu, P. C.; Li, Y.; Lee, H. W.; Cui, Y. Ionic Conductivity Enhancement of Polymer Electrolytes with Ceramic Nanowire Fillers. *Nano Lett.* **2015**, *15* (4), 2740–2745.

(128) Yang, T.; Li, Y.; Chan, C. K. Enhanced Lithium Ion Conductivity in Lithium Lanthanum Titanate Solid Electrolyte Nanowires Prepared by Electrospinning. *J. Power Sources* **2015**, *287*, 164–169.

(129) Murugan, R.; Thangadurai, V.; Weppner, W. Fast Lithium Ion Conduction in Garnet-Type Li7La 3Zr2O12. *Angew. Chemie - Int. Ed.* **2007**, *46* (41), 7778–7781.

(130) Thangadurai, V.; Narayanan, S.; Pinzaru, D. Garnet-Type Solid-State Fast Li Ion Conductors for Li Batteries: Critical Review. *Chem. Soc. Rev.* **2014**, *43* (13), 4714–4727.

(131) Kim, K. H.; Iriyama, Y.; Yamamoto, K.; Kumazaki, S.; Asaka, T.; Tanabe, K.; Fisher, C. A. J.; Hirayama, T.; Murugan, R.; Ogumi, Z. Characterization of the Interface between LiCoO2 and Li 7La3Zr2O12 in an All-Solid-State Rechargeable Lithium Battery. *J. Power Sources* **2011**, *196* (2), 764–767.

(132) Thangadurai, V.; Kaack, H.; Weppner, W. J. F. Novel Fast Lithium Ion Conduction in Garnet-Type Li 5 La 3 M 2 O 12 (M = Nb, Ta). *J. Am. Ceram. Soc.* **2003**, *86* (3), 437–440.

(133) Yang, T.; Gordon, Z. D.; Li, Y.; Chan, C. K. Nanostructured Garnet-Type Solid Electrolytes for Lithium Batteries: Electrospinning Synthesis of Li7La3Zr2O12 Nanowires and Particle Size-Dependent Phase Transformation. *J. Phys. Chem. C* **2015**, *119* (27), 14947–14953.

(134) Zheng, J.; Tang, M.; Hu, Y.-Y. Lithium Ion Pathway within Li7 La3 Zr2 O12 - Polyethylene Oxide Composite Electrolytes. *Angew. Chem. Int. Ed. Engl.* **2016**, *55* (40), 12538–12542.

(135) Ma, C.; Cheng, Y.; Yin, K.; Luo, J.; Sharafi, A.; Sakamoto, J.; Li, J.; More, K. L.; Dudney, N. J.; Chi, M. Interfacial Stability of Li Metal-Solid Electrolyte Elucidated via in Situ Electron Microscopy. *Nano Lett.* **2016**, *16* (11), 7030–7036.

(136) Wolfenstine, J.; Allen, J. L.; Read, J.; Sakamoto, J. Chemical Stability of Cubic Li7La3Zr 2O12 with Molten Lithium at Elevated Temperature. *J. Mater. Sci.* **2013**, *48* (17), 5846–5851.

(137) Wu, J.-F.; Chen, E.-Y.; Yu, Y.; Liu, L.; Wu, Y.; Pang, W.-K.; Peterson, V. K.; Guo, X. Gallium-Doped Li $_7$ La $_3$ Zr $_2$ O $_{12}$ Garnet-Type Electrolytes with High Lithium-Ion Conductivity. *ACS Appl. Mater. Interfaces* **2016**, acsami.6b13902.

(138) Richards, W. D.; Miara, L. J.; Wang, Y.; Kim, J. C.; Ceder, G. Interface Stability in Solid-State Batteries. *Chem. Mater.* **2016**, *28* (1), 266–273.

(139) Han, F.; Zhu, Y.; He, X.; Mo, Y.; Wang, C. Electrochemical Stability of Li10GeP2S12 and Li7La3Zr2O12 Solid Electrolytes. *Adv. Energy Mater.* **2016**, *6* (8), 1–9.

(140) Zhu, Y.; He, X.; Mo, Y. First Principles Study on Electrochemical and Chemical Stability of the Solid Electrolyte-Electrode Interfaces in All-Solid-State Li-Ion Batteries. *J. Mater. Chem. A* **2015**, *4* (9), 1–14.

(141) Chen, R. J.; Zhang, Y. B.; Liu, T.; Xu, B. Q.; Lin, Y. H.; Nan, C. W.; Shen, Y. Addressing the Interface Issues in All-Solid-State Bulk-Type Lithium Ion Battery via an All-Composite Approach. *ACS Appl. Mater. Interfaces* **2017**, *9* (11), 9654–9661.

(142) Raj, R.; Wolfenstine, J. Current Limit Diagrams for Dendrite Formation in Solid-State Electrolytes for Li-Ion Batteries. *J. Power Sources* **2017**, *343*, 119–126.

(143) Zhou, W.; Wang, S.; Li, Y.; Xin, S.; Manthiram, A.; Goodenough, J. B. Plating a Dendrite-Free Lithium Anode with a Polymer/Ceramic/Polymer Sandwich Electrolyte. *J. Am. Chem. Soc.* **2016**, *138* (30), 9385–9388.

(144) Tao, X.; Liu, Y.; Liu, W.; Zhou, G.; Zhao, J.; Lin, D.; Zu, C.; Sheng, O.; Zhang, W.; Lee, H.-W.; et al. Solid-State Lithium–Sulfur Batteries Operated at 37 °C with Composites of Nanostructured Li7La3Zr2O12/Carbon Foam and Polymer. *Nano Lett.* **2017**, *17* (5), 2967–2972.

(145) Cheng, L.; Chen, W.; Kunz, M.; Persson, K.; Tamura, N.; Chen, G.; Doeff, M. Effect of Surface Microstructure on Electrochemical Performance of Garnet Solid Electrolytes. *ACS Appl. Mater. Interfaces* **2015**, *7* (3), 2073–2081.

(146) Sudo, R.; Nakata, Y.; Ishiguro, K.; Matsui, M.; Hirano, A.; Takeda, Y.; Yamamoto, O.; Imanishi, N. Interface Behavior between Garnet-Type Lithium-Conducting Solid Electrolyte and Lithium Metal. *Solid State Ionics* **2014**, *262*, 151–154.

(147) Han, X.; Gong, Y.; Fu, K.; He, X.; Hitz, G. T.; Dai, J.; Pearse, A.; Liu, B.; Wang, H.; Rubloff, G.; et al. Negating Interfacial Impedance in Garnet-Based Solid-State Li Metal Batteries. *Nat. Mater.* **2017**, *16* (5), 572–579.

(148) Wang, C.; Gong, Y.; Liu, B.; Fu, K.; Yao, Y.; Hitz, E.; Li, Y.; Dai, J.; Xu, S.; Luo, W.; et al. Conformal, Nanoscale ZnO Surface Modification of Garnet-Based Solid-State Electrolyte for Lithium Metal Anodes. *Nano Lett.* **2017**, *17* (1), 565–571.

(149) Luo, W.; Gong, Y.; Zhu, Y.; Fu, K. K.; Dai, J.; Lacey, S. D.; Wang, C.; Liu, B.; Han, X.; Mo, Y.; et al. Transition from Superlithiophobicity to Superlithiophilicity of Garnet Solid-State Electrolyte. *J. Am. Chem. Soc.* **2016**, *138* (37), 12258–12262.

(150) Fu, K. (Kelvin); Gong, Y.; Liu, B.; Zhu, Y.; Xu, S.; Yao, Y.; Luo, W.; Wang, C.; Lacey, S. D.; Dai, J.; et al. Toward Garnet Electrolyte–based Li Metal Batteries: An Ultrathin, Highly Effective, Artificial Solid-State Electrolyte/Metallic Li Interface. *Sci. Adv.* **2017**, *3* (4).

(151) Xiao, P.; Derby, B. Wetting of Titanium Nitride and Titanium Carbide by Liquid Metals. *Acta Mater.* **1996**, *44* (1), 307–314.

(152) Drevet, B.; Eustathopoulos, N. Wetting of Ceramics by Molten Silicon and Silicon Alloys: A Review. *J. Mater. Sci.* **2012**, *47* (24), 8247–8260.

(153) Klein, R.; Desmaison-Brut, M.; Ginet, P.; Bellosi, A.; Desmaison, J. Wettability of Silicon Nitride Ceramic Composites by Silver, Copper and Silver Copper Titanium Alloys. *J. Eur. Ceram. Soc.* **2005**, *25* (10 SPEC. ISS.), 1757–1763.

(154) Contreras, A.; Bedolla, E.; Pérez, R. Interfacial Phenomena in Wettability of TiC by Al-Mg Alloys. *Acta Mater.* **2004**, *52* (4), 985–994.

(155) Trybula, M.; Gancarz, T.; Gasior, W.; Pasturel, A. Bulk and Surface Properties of Liquid Al-Li and Li-Zn Alloys. *Metall. Mater. Trans. A Phys. Metall. Mater. Sci.* **2014**, *45* (12), 5517–5530.

(156) Sharafi, A.; Meyer, H. M.; Nanda, J.; Wolfenstine, J.; Sakamoto, J. Characterizing the Li-Li7La3Zr2O12 Interface Stability and Kinetics as a Function of Temperature and Current Density. *J. Power Sources* **2016**, *302*, 135–139.

(157) Wakasugi, J.; Munakata, H.; Kanamura, K. Effect of Gold Layer on Interface Resistance between Lithium Metal Anode and $Li_{6.25}Al_{0.25}La_3Zr_2O_{12}$ Solid Electrolyte. *J. Electrochem. Soc.* **2017**, *164* (6), A1022–A1025.

(158) Liang, Y.; Du, Z.; Guo, C.; Li, C. Thermodynamic Modeling of the Li-Zn System. *J. Alloys Compd.* **2008**, *455* (1–2), 236–242.

(159) Sangster, J.; Bale, C. W. The Lithium-Tin System. *J. Phase Equilibria* **1998**, *19* (1), 70–75.

(160) Braga, M. H.; Malheiros, L. F.; Ansara, I. Thermodynamic Assessment of the Li-Si System. *J. Phase Equilibria* **1995**, *16* (4), 324–330.

(161) Tsvetkov, N.; Lu, Q.; Yildiz, B. Improved Electrochemical Stability at the Surface of $La_{0.8}Sr_{0.2}CoO_3$ Achieved by Surface Chemical Modification. *Faraday Discuss.* **2015**, *182*, 257–269.

(162) Tsvetkov, N.; Lu, Q.; Sun, L.; Crumlin, E. J.; Yildiz, B. Improved Chemical and Electrochemical Stability of Perovskite Oxides with Less Reducible Cations at the Surface. *Nat. Mater.* **2016**, *15* (9), 1010–1016.

(163) Knauth, P. Inorganic Solid Li Ion Conductors: An Overview. *Solid State Ionics* **2009**, *180* (14–16), 911–916.

(164) Hasegawa, S.; Imanishi, N.; Zhang, T.; Xie, J.; Hirano, A.; Takeda, Y.; Yamamoto, O. Study on Lithium/Air Secondary Batteries-Stability of NASICON-Type Lithium Ion Conducting Glass-Ceramics with Water. *J. Power Sources* **2009**, *189* (1), 371–377.

(165) Manthiram, A.; Yu, X.; Wang, S. Lithium Battery Chemistries Enabled by Solid-State Electrolytes. *Nat. Rev. Mater.* **2017**, *2* (4), 1–16.

(166) Garbayo, I.; Struzik, M.; Bowman, W. J.; Pfenninger, R.; Stilp, E.; Rupp, J. L. M. Glass-Type Polyamorphism in Li-Garnet Thin Film Solid State Battery Conductors. *Adv. Energy Mater.* **2018**, *1702265*, 1–14.

(167) Jin, Y.; Liu, K.; Lang, J.; Zhuo, D.; Huang, Z.; Wang, C.; Wu, H.; Cui, Y. An Intermediate Temperature Garnet-Type Solid Electrolyte-Based Molten Lithium Battery for Grid Energy Storage. *Nat. Energy*.

(168) Zhao, C.-Z.; Zhang, X.-Q.; Cheng, X.-B.; Zhang, R.; Xu, R.; Chen, P.-Y.; Peng, H.-J.; Huang, J.-Q.; Zhang, Q. An Anion-Immobilized Composite Electrolyte for Dendrite-Free Lithium Metal Anodes. *Proc. Natl. Acad. Sci.* **2017**, 201708489.

(169) Han, F.; Yue, J.; Chen, C.; Zhao, N.; Fan, X.; Ma, Z.; Gao, T.; Wang, F.; Guo, X.; Wang, C. Interphase Engineering Enabled All-Ceramic Lithium Battery. *Joule* **2018**, *2* (3), 497–508.

(170) Porz, L.; Swamy, T.; Sheldon, B. W.; Rettenwander, D.; Frömling, T.; Berendts, S.; Uecker, R.; Carter, W. C.; Chiang, Y. Mechanism of Lithium Metal Penetration through Inorganic Solid Electrolytes. *Adv. Energy Mater.* **2017**, *1701003*, 1–12.

(171) Aguesse, F.; Manalastas, W.; Buannic, L.; Del Amo, J. M. L.; Singh, G.; Llordés, A.; Kilner, J. Investigating the Dendritic Growth during Full Cell Cycling of Garnet Electrolyte in Direct Contact with Li Metal. *ACS Appl. Mater. Interfaces* **2017**, *9* (4), 3808–3816.

(172) Tsai, C.-L.; Roddatis, V.; Chandran, C. V.; Ma, Q.; Uhlenbruck, S.; Bram, M.; Heitjans, P.; Guillon, O. $Li_7La_3Zr_2O_{12}$ Interface Modification for Li Dendrite Prevention. *ACS Appl. Mater. Interfaces* **2016**, *8* (16), 10617–10626.

(173) Ren, Y.; Shen, Y.; Lin, Y.; Nan, C. W. Direct Observation of Lithium Dendrites inside Garnet-Type Lithium-Ion Solid Electrolyte. *Electrochem. commun.* **2015**, *57*, 27–30.

(174) Tsai, C. L.; Roddatis, V.; Chandran, C. V.; Ma, Q.; Uhlenbruck, S.; Bram, M.; Heitjans, P.; Guillon, O. Li7La3Zr2O12Interface Modification for Li Dendrite Prevention. *ACS Appl. Mater. Interfaces* **2016**, *8* (16), 10617–10626.

(175) Shen, Y.; Zhang, Y.; Han, S.; Wang, J.; Peng, Z.; Chen, L. Unlocking the Energy Capabilities of Lithium Metal Electrode with Solid-State Electrolytes. *Joule* **2018**.

(176) Cheng, L.; Crumlin, E. J.; Chen, W.; Qiao, R.; Hou, H.; Franz Lux, S.; Zorba, V.; Russo, R.; Kostecki, R.; Liu, Z.; et al. The Origin of High Electrolyte-Electrode Interfacial Resistances in Lithium Cells Containing Garnet Type Solid Electrolytes. *Phys. Chem. Chem. Phys.* **2014**, *16*, 18294–18300.

(177) Sharafi, A.; Yu, S.; Naguib, M.; Lee, M.; Ma, C.; Meyer, H. M.; Nanda, J.; Chi, M.; Siegel, D. J.; Sakamoto, J. Impact of Air Exposure and Surface Chemistry on Li–Li $_7$ La $_3$ Zr $_2$ O $_{12}$ Interfacial Resistance. *J. Mater. Chem. A* **2017**, *5* (26), 13475–13487.

(178) Nyman, M.; Alam, T. M.; McIntyre, S. K.; Bleier, G. C.; Ingersoll, D. Alternative Approach to Increasing Li Mobility in Li-La-Nb/Ta Garnet Electrolytes. *Chem. Mater.* **2010**, *22* (19), 5401–5410.

(179) Rao, R. P.; Gu, W.; Sharma, N.; Peterson, V. K.; Avdeev, M.; Adams, S. In Situ Neutron Diffraction Monitoring of Li7La3Zr2O12 Formation: Toward a Rational Synthesis of Garnet Solid Electrolytes. *Chem. Mater.* **2015**, *27* (8), 2903–2910.

(180) Zhan, X.; Lai, S.; Gobet, M. P.; Greenbaum, S. G.; Shirpour, M. Defect Chemistry and Electrical Properties of Garnet-Type Li $_7$ La $_3$ Zr $_2$ O $_{12}$. *Phys. Chem. Chem. Phys.* **2018**, *20* (3), 1447–1459.

(181) Kubicek, M.; Wachter-Welzl, A.; Rettenwander, D.; Wagner, R.; Berendts, S.; Uecker, R.; Amthauer, G.; Hutter, H.; Fleig, J. Oxygen Vacancies in Fast Lithium-Ion Conducting Garnets. *Chem. Mater.* **2017**, *29* (17), 7189–7196.

(182) Li, Y.; Chen, X.; Dolocan, A.; Cui, Z.; Xin, S.; Xu, H.; Park, K.; Goodenough, J. B.; Li, Y.; Chen, X.; et al. Garnet Electrolyte with an Ultra-Low Interfacial Resistance for Li-Metal Batteries Garnet Electrolyte with an Ultra-Low Interfacial Resistance for Li- Metal Batteries. *J. Am. Chem. Soc.* **2018**, *140*, 6448–6455.

(183) Wang, C.; Wang, Y.; Yao, Y.; Luo, W.; Wan, J.; Dai, J.; Hitz, E.; Fu, K. K.; Hu, L. A Solution-Processed High-Temperature, Flexible, Thin-Film Actuator. *Adv. Mater.* **2016**, *28* (39), 8618–8624.

(184) Sharafi, A.; Kazyak, E.; Davis, A. L.; Yu, S.; Thompson, T.; Siegel, D. J.; Dasgupta, N. P.; Sakamoto, J. Surface Chemistry Mechanism of Ultra-Low Interfacial Resistance in the Solid-State Electrolyte Li7La3Zr2O12. *Chem. Mater.* **2017**, *29* (18), 7961–7968.

(185) Larraz, G.; Orera, A.; Sanjuán, M. L. Cubic Phases of Garnet-Type Li7La3Zr2O12: The Role of Hydration. *J. Mater. Chem. A* **2013**, *1* (37), 11419.

(186) Wang, H.; Downing, R. G.; Dura, J. A.; Hussey, D. S. In Situ Neutron Techniques for Studying Lithium Ion Batteries. *Polym. Energy Storage Deliv. Polyelectrolytes Batter. Fuel Cells* **2012**, *1096*, 91–106.

(187) Lamaze, G. P.; Chen-Mayer, H. H.; Becker, D. A.; Vereda, F.; Goldner, R. B.; Haas, T.; Zerigian, P. Cold Neutron Depth Profiling of Lithium-Ion Battery Materials. *J. Power Sources* **2003**, *119–121*, 680–685.

(188) Huang, M.; Liu, T.; Deng, Y.; Geng, H.; Shen, Y.; Lin, Y.; Nan, C. W. Effect of Sintering Temperature on Structure and Ionic Conductivity of Li 7 - XLa 3Zr 2O 12 - 0.5x (x = 0.5 ~ 0.7) Ceramics. *Solid State Ionics* **2011**, *204–205* (1), 41–45.

(189) Suzuki, Y.; Kami, K.; Watanabe, K.; Watanabe, A.; Saito, N.; Ohnishi, T.; Takada, K.; Sudo, R.; Imanishi, N. Transparent Cubic Garnet-Type Solid Electrolyte of Al2O3-Doped Li7La3Zr2O12. *Solid State Ionics* **2015**, *278*, 172–176.

(190) Cheng, L.; Hou, H.; Lux, S.; Kostecki, R.; Davis, R.; Zorba, V.; Mehta, A.; Doeff, M. Enhanced Lithium Ion Transport in Garnet-Type Solid State Electrolytes. *J. Electroceramics* **2017**, *38* (2–4), 168–175.

(191) Wang, K.; Chang, Y.; Lv, L.; Long, Y. Effect of Annealing Temperature on Oxygen Vacancy Concentrations of Nanocrystalline CeO2film. *Appl. Surf. Sci.* **2015**, *351*, 164–168.

(192) Li, Y.; Wang, Z.; Li, C.; Cao, Y.; Guo, X. Densification and Ionic-Conduction Improvement of Lithium Garnet Solid Electrolytes by Flowing Oxygen Sintering. *J. Power Sources* **2014**, *248*, 642–646.

(193) Wang, C.; Xie, H.; Zhang, L.; Gong, Y.; Pastel, G.; Dai, J.; Liu, B.; Wachsman, E. D.; Hu, L. Universal Soldering of Lithium and Sodium Alloys on Various Substrates for Batteries. *Adv. Energy Mater.* **2017**, *1701963*, 1701963.

(194) Liu, W.; Lee, S. W.; Lin, D.; Shi, F.; Wang, S.; Sendek, A. D.; Cui, Y. Enhancing Ionic Conductivity in Composite Polymer Electrolytes with Well-Aligned Ceramic Nanowires. *Nat. energy* **2017**, *2* (5), 17035.

(195) Zheng, J.; Dang, H.; Feng, X.; Chien, P.-H.; Hu, Y.-Y. Li-Ion Transport in a Representative Ceramic–polymer–plasticizer Composite Electrolyte: Li 7 La 3 Zr 2 O 12–polyethylene Oxide–tetraethylene Glycol Dimethyl Ether. *J. Mater. Chem. A* **2017**, *5* (35), 18457–18463.

(196) Yang, T.; Zheng, J.; Cheng, Q.; Hu, Y.-Y.; Chan, C. K. Composite Polymer Electrolytes with Li7La3Zr2O12 Garnet-Type Nanowires as Ceramic Fillers: Mechanism of Conductivity Enhancement and Role of Doping and Morphology. *ACS Appl. Mater. Interfaces* **2017**, *9* (26), 21773–21780.

(197) Zhao, C.-Z.; Zhang, X.-Q.; Cheng, X.-B.; Zhang, R.; Xu, R.; Chen, P.-Y.; Peng, H.-J.; Huang, J.-Q.; Zhang, Q. An Anion-Immobilized Composite Electrolyte for Dendrite-Free Lithium Metal Anodes. *Proc. Natl. Acad. Sci.* **2017**, 201708489.

(198) Fu, K. K.; Gong, Y.; Dai, J.; Gong, A.; Han, X.; Yao, Y.; Wang, C.; Wang, Y.; Chen, Y.; Yan, C. Flexible, Solid-State, Ion-Conducting Membrane with 3D Garnet Nanofiber Networks for Lithium Batteries. *Proc. Natl. Acad. Sci.* **2016**, *113* (26), 7094–7099.

(199) Römling, U.; Galperin, M. Y. Bacterial Cellulose Biosynthesis: Diversity of Operons, Subunits, Products, and Functions. *Trends Microbiol.* **2015**, *23* (9), 545–557.

(200) Yamanaka, S.; Watanabe, K.; Kitamura, N.; Iguchi, M.; Mitsuhashi, S.; Nishi, Y.; Uryu, M. The Structure and Mechanical Properties of Sheets Prepared from Bacterial Cellulose. *J. Mater. Sci.* **1989**, *24* (9), 3141–3145.

(201) Bäckdahl, H.; Helenius, G.; Bodin, A.; Nannmark, U.; Johansson, B. R.; Risberg, B.; Gatenholm, P. Mechanical Properties of Bacterial Cellulose and Interactions with Smooth Muscle Cells. *Biomaterials* **2006**, *27* (9), 2141–2149.

(202) Svensson, A.; Nicklasson, E.; Harrah, T.; Panilaitis, B.; Kaplan, D. L.; Brittberg, M.; Gatenholm, P. Bacterial Cellulose as a Potential Scaffold for Tissue Engineering of Cartilage. *Biomaterials* **2005**, *26* (4), 419–431.

(203) Chen, L.; Huang, Z.; Liang, H.; Gao, H.; Yu, S. Three-dimensional Heteroatom-doped Carbon Nanofiber Networks Derived from Bacterial Cellulose for Supercapacitors. *Adv. Funct. Mater.* **2014**, *24* (32), 5104–5111.

(204) Chen, L.; Huang, Z.; Liang, H.; Guan, Q.; Yu, S. Bacterial-cellulose-derived Carbon Nanofiber@ MnO2 and Nitrogen-doped Carbon Nanofiber Electrode Materials: An Asymmetric Supercapacitor with High Energy and Power Density. *Adv. Mater.* **2013**, *25* (34), 4746–4752.

(205) Nakayama, A.; Kakugo, A.; Gong, J. P.; Osada, Y.; Takai, M.; Erata, T.; Kawano, S. High Mechanical Strength Double-network Hydrogel with Bacterial Cellulose. *Adv. Funct. Mater.* **2004**, *14* (11), 1124–1128.

(206) Long, C.; Qi, D.; Wei, T.; Yan, J.; Jiang, L.; Fan, Z. Nitrogen-doped Carbon Networks for High Energy Density Supercapacitors Derived from Polyaniline Coated Bacterial Cellulose. *Adv. Funct. Mater.* **2014**, *24* (25), 3953–3961.

(207) Juntaro, J.; Pommet, M.; Kalinka, G.; Mantalaris, A.; Shaffer, M. S. P.; Bismarck, A. Creating Hierarchical Structures in Renewable Composites by Attaching Bacterial Cellulose onto Sisal Fibers. *Adv. Mater.* **2008**, *20* (16), 3122–3126.

(208) Narayanan, S.; Baral, A. K.; Thangadurai, V. Dielectric Characteristics of Fast Li Ion Conducting Garnet-Type Li5+2: XLa3Nb2- XYxO12 (x = 0.25, 0.5 and 0.75). *Phys. Chem. Chem. Phys.* **2016**, *18* (22), 15418–15426.

(209) Afyon, S.; Krumeich, F.; Rupp, J. L. M. A Shortcut to Garnet-Type Fast Li-Ion Conductors for All-Solid State Batteries. *J. Mater. Chem. A* **2015**, *3* (36), 18636–18648.

(210) Miara, L. J.; Ong, S. P.; Mo, Y.; Richards, W. D.; Park, Y.; Lee, J.-M.; Lee, H. S.; Ceder, G. Effect of Rb and Ta Doping on the Ionic Conductivity and Stability of the Garnet Li $_{7+2x-y}$ (La $_{3-x}$ Rb $_{x}$)(Zr $_{2-y}$ Ta $_{y}$)O $_{12}$ ($0 \leq$ <i>.

Chem. Mater. **2013**, *25* (15), 3048–3055.

(211) Croce, F.; Persi, L. L.; Scrosati, B.; Serraino-Fiory, F.; Plichta, E.; Hendrickson, M. A. Role of the Ceramic Fillers in Enhancing the Transport Properties of Composite Polymer Electrolytes. *Electrochim. Acta* **2001**, *46* (16), 2457–2461.

(212) Wieczorek, W.; Florjanczyk, Z.; Stevens, J. R. Composite Based Solid. *Electrochim. Acta* **1995**, *40* (13–14), 2251–2258.

(213) Wieczorek, W.; Such, K.; Wyciślik, H.; Płocharski, J. Modifications of Crystalline Structure of Peo Polymer Electrolytes with Ceramic Additives. *Solid State Ionics* **1989**, *36* (3–4), 255–257.

(214) Croce, F.; Curini, R.; Martinelli, A.; Persi, L.; Ronci, F.; Scrosati, B.; Caminiti, R. Physical and Chemical Properties of Nanocomposite Polymer Electrolytes. *J. Phys. Chem. B* **2002**, *103* (48), 10632–10638.

(215) Scrosati, B.; Croce, F.; Persi, L. Impedance Spectroscopy Study of PEO-Based Nanocomposite Polymer Electrolytes. *J. Electrochem. Soc.* **2002**, *147* (5), 1718.

(216) Chu, P. P.; Reddy, M. J.; Kao, H. M. Novel Composite Polymer Electrolyte Comprising Mesoporous Structured SiO2 and PEO/Li. *Solid State Ionics* **2003**, *156* (1–2), 141–153.

(217) Thompson, T.; Wolfenstine, J.; Allen, J. L.; Johannes, M.; Huq, A.; David, I. N.; Sakamoto, J. Tetragonal vs. Cubic Phase Stability in Al – Free Ta Doped Li $_7$ La $_3$ Zr $_2$ O $_{12}$ (LLZO). *J. Mater. Chem. A* **2014**, *2* (33), 13431–13436.

(218) Jin, Y.; McGinn, P. J. Al-Doped Li7La3Zr2O12 Synthesized by a Polymerized Complex Method. *J. Power Sources* **2011**, *196* (20), 8683–8687.

(219) Dunn, J. B.; Gaines, L.; Kelly, J. C.; James, C.; Gallagher, K. G. The Significance of Li-Ion Batteries in Electric Vehicle Life-Cycle Energy and Emissions and Recycling's Role in Its Reduction. *Energy Environ. Sci.* **2015**, *8* (1), 158–168.

(220) Schmidt, O.; Hawkes, A.; Gambhir, A.; Staffell, I. The Future Cost of Electrical Energy Storage Based on Experience Rates. *Nat. Energy* **2017**, *6* (July), 17110.

(221) Schmuch, R.; Wagner, R.; Hörpel, G.; Placke, T.; Winter, M. Performance and Cost of Materials for Lithium-Based Rechargeable Automotive Batteries. *Nat. Energy* **2018**, *3* (4), 267–278.

(222) Tran, M.; Banister, D.; Bishop, J. D. K.; McCulloch, M. D. Realizing the Electric-Vehicle Revolution. *Nat. Clim. Chang.* **2012**, *2* (5), 328–333.

(223) Choi, J. W.; Aurbach, D. Promise and Reality of Post-Lithium-Ion Batteries with High Energy Densities. *Nat. Rev. Mater.* **2016**, *1*.

(224) Xu, W.; Wang, J.; Ding, F.; Chen, X.; Nasybulin, E.; Zhang, Y.; Zhang, J. G. Lithium Metal Anodes for Rechargeable Batteries. *Energy Environ. Sci.* **2014**, *7* (2), 513–537.

(225) Goodenough, J. B.; Park, K. S. The Li-Ion Rechargeable Battery: A Perspective. *J. Am. Chem. Soc.* **2013**, *135* (4), 1167–1176.

(226) Lin, D.; Liu, Y.; Cui, Y. Reviving the Lithium Metal Anode for High-Energy Batteries. *Nat. Nanotechnol.* **2017**, *12* (3), 194–206.

(227) Cheng, X. B.; Zhang, R.; Zhao, C. Z.; Zhang, Q. Toward Safe Lithium Metal Anode in Rechargeable Batteries: A Review. *Chem. Rev.* **2017**, *117* (15), 10403–10473.

(228) Wood, K. N.; Noked, M.; Dasgupta, N. P. Lithium Metal Anodes: Toward an Improved Understanding of Coupled Morphological, Electrochemical, and Mechanical Behavior. *ACS Energy Lett.* **2017**, *2* (3), 664–672.

(229) Deng, Z.; Wang, Z.; Chu, I.-H.; Luo, J.; Ong, S. P. Elastic Properties of Alkali Superionic Conductor Electrolytes from First Principles Calculations. *J. Electrochem. Soc.* **2016**, *163* (2), A67–A74.

(230) Milling, M. Preparation of Li 2 S–P 2 S 5 Amorphous Solid Electrolytes by Mechanical Milling. **2001**, *79*, 477–479.

(231) Li, Y.; Xu, B.; Xu, H.; Duan, H.; Lü, X.; Xin, S.; Zhou, W.; Xue, L.; Fu, G.; Manthiram, A.; et al. Hybrid Polymer/Garnet Electrolyte with a Small Interfacial Resistance for Lithium-Ion Batteries. *Angew. Chemie - Int. Ed.* **2017**, *56* (3), 753–756.

(232) Zhang, J.; Zhao, N.; Zhang, M.; Li, Y.; Chu, P. K.; Guo, X.; Di, Z.; Wang, X.; Li, H. Flexible and Ion-Conducting Membrane Electrolytes for Solid-State Lithium Batteries: Dispersion of Garnet Nanoparticles in Insulating Polyethylene Oxide. *Nano Energy* **2016**, *28*, 447–454.

(233) Fu, K. (Kelvin); Gong, Y.; Dai, J.; Gong, A.; Han, X.; Yao, Y.; Wang, C.; Wang, Y.; Chen, Y.; Yan, C.; et al. Flexible, Solid-State, Ion-Conducting Membrane with 3D Garnet Nanofiber Networks for Lithium Batteries. *Proc. Natl. Acad. Sci.* **2016**, *113* (26), 7094–7099.

(234) Zhai, H.; Xu, P.; Ning, M.; Cheng, Q.; Mandal, J.; Yang, Y. A Flexible Solid Composite Electrolyte with Vertically Aligned and Connected Ion-Conducting Nanoparticles for Lithium Batteries. *Nano Lett.* **2017**, *17* (5), 3182–3187.

(235) Xie, H.; Yang, C.; Fu, K. K.; Yao, Y.; Jiang, F.; Hitz, E. Flexible , Scalable , and Highly Conductive Garnet-Polymer Solid Electrolyte Templated by Bacterial Cellulose. *Adv. Energy Mater.* **2018**, *1703474*, 1–7.

(236) Zheng, J.; Dang, H.; Feng, X.; Chien, P. H.; Hu, Y. Y. Li-Ion Transport in a Representative Ceramic-Polymer-Plasticizer Composite Electrolyte: Li7La3Zr2O12-Polyethylene Oxide-Tetraethylene Glycol Dimethyl Ether. *J. Mater. Chem. A* **2017**, *5* (35), 18457–18463.

(237) Choudhury, S.; Mangal, R.; Agrawal, A.; Archer, L. A. A Highly Reversible Room-Temperature Lithium Metal Battery Based on Crosslinked Hairy Nanoparticles. *Nat. Commun.* **2015**, *6*, 1–9.

(238) Alarco, P. J.; Abu-Lebdeh, Y.; Abouimrane, A.; Armand, M. The Plastic-

Crystalline Phase of Succinonitrile as a Universal Matrix for Solid-State Ionic Conductors. *Nat. Mater.* **2004**, *3* (7), 476–481.

(239) Lee, J. H.; Lee, S.; Paik, U.; Choi, Y. M. Aqueous Processing of Natural Graphite Particulates for Lithium-Ion Battery Anodes and Their Electrochemical Performance. *J. Power Sources* **2005**, *147* (1–2), 249–255.

(240) Shi, C.; Zhang, P.; Chen, L.; Yang, P.; Zhao, J. Effect of a Thin Ceramic-Coating Layer on Thermal and Electrochemical Properties of Polyethylene Separator for Lithium-Ion Batteries. *J. Power Sources* **2014**, *270*, 547–553.

(241) Zhang, R.; Yang, X.; Zhang, D.; Qiu, H.; Fu, Q.; Na, H.; Guo, Z.; Du, F.; Chen, G.; Wei, Y. Water Soluble Styrene Butadiene Rubber and Sodium Carboxyl Methyl Cellulose Binder for ZnFe2O4anode Electrodes in Lithium Ion Batteries. *J. Power Sources* **2015**, *285*, 227–234.

(242) Yen, J.-P.; Chang, C.-C.; Lin, Y.-R.; Shen, S.-T.; Hong, J.-L. Effects of Styrene-Butadiene Rubber/Carboxymethylcellulose (SBR/CMC) and Polyvinylidene Difluoride (PVDF) Binders on Low Temperature Lithium Ion Batteries. *J. Electrochem. Soc.* **2013**, *160* (10), A1811–A1818.

(243) Scrosati, B.; Vincent, C. A. Polymer Electrolytes: The Key to Lithium Polymer Batteries. *MRS Bull.* **2000**, *25* (3), 28–30.

(244) Fu, K.; Wang, Y.; Yan, C.; Yao, Y.; Chen, Y.; Dai, J.; Lacey, S.; Wang, Y.; Wan, J.; Li, T.; et al. Graphene Oxide-Based Electrode Inks for 3D-Printed Lithium-Ion Batteries. *Adv. Mater.* **2016**, *28* (13), 2587–2594.

(245) Fu, K.; Yao, Y.; Dai, J.; Hu, L. Progress in 3D Printing of Carbon Materials for Energy-Related Applications. *Adv. Mater.* **2017**, *29* (9).

(246) Wolfenstine, J.; Jo, H.; Cho, Y. H.; David, I. N.; Askeland, P.; Case, E. D.; Kim, H.; Choe, H.; Sakamoto, J. A Preliminary Investigation of Fracture Toughness of Li7La 3Zr2O12 and Its Comparison to Other Solid Li-Ionconductors. *Mater. Lett.* **2013**, *96*, 117–120.

(247) Yu, S.; Schmidt, R. D.; Garcia-Mendez, R.; Herbert, E.; Dudney, N. J.; Wolfenstine, J. B.; Sakamoto, J.; Siegel, D. J. Elastic Properties of the Solid Electrolyte Li7La3Zr2O12(LLZO). *Chem. Mater.* **2016**, *28* (1), 197–206.

(248) Xiang, K.; Wang, X.; Huang, G.; Zheng, J.; Huang, J.; Li, G. Thermal Ageing Behavior of Styrene-Butadiene Random Copolymer: A Study on the Ageing Mechanism and Relaxation Properties. *Polym. Degrad. Stab.* **2012**, *97* (9), 1704–1715.

(249) Masson, J. F.; Pelletier, L.; Collins, P. Rapid FTIR Method for Quantification of Styrene-Butadiene Type Copolymers in Bitumen. *J. Appl. Polym. Sci.* **2001**, *79* (6), 1034–1041.

(250) Song, S.; Sheptyakov, D.; Korsunsky, A. M.; Duong, H. M.; Lu, L. High Li Ion Conductivity in a Garnet-Type Solid Electrolyte via Unusual Site Occupation of the Doping Ca Ions. *Mater. Des.* **2016**, *93*, 232–237.

(251) Zhu, K.; Liu, Y.; Liu, J. A Fast Charging/Discharging All-Solid-State Lithium

Ion Battery Based on PEO-MIL-53(Al)-LiTFSI Thin Film Electrolyte. *RSC Adv.* **2014**, *4* (80), 42278–42284.

(252) Ban, X.; Zhang, W.; Chen, N.; Sun, C. A High-Performance and Durable Poly(Ethylene Oxide)-Based Composite Solid Electrolyte for All Solid-State Lithium Battery. *J. Phys. Chem. C* **2018**, *122* (18), 9852–9858.

(253) Nevo, Y.; Peer, N.; Yochelis, S.; Igbaria, M.; Meirovitch, S.; Shoseyov, O.; Paltiel, Y. Nano Bio Optically Tunable Composite Nanocrystalline Cellulose Films. *RSC Adv.* **2015**, *5* (10), 7713–7719.

(254) Yu, S.; Schmidt, R. D.; Garcia-Mendez, R.; Herbert, E.; Dudney, N. J.; Wolfenstine, J. B.; Sakamoto, J.; Siegel, D. J. Elastic Properties of the Solid Electrolyte $Li_7La_3Zr_2O_{12}$ (LLZO). *Chem. Mater.* **2016**, *28* (1), 197–206.

(255) Deng, Z.; Wang, Z.; Chu, I.-H.; Luo, J.; Ong, S. P. Elastic Properties of Alkali Superionic Conductor Electrolytes from First Principles Calculations. *J. Electrochem. Soc.* **2015**, *163* (2), A67–A74.